UNIVERSITY OF SOUTHAMPTON

FACULTY OF PHYSICAL SCIENCES AND ENGINEERING

Optoelectronics Research Centre

Development of Highly Efficient Thulium-doped High Power Fibre Lasers

By

Norberto Javier Ramírez Martínez

ORCID ID 0000-0001-8711-792X

Thesis for the degree of Doctor of Philosophy

January 2021

UNIVERSITY OF SOUTHAMPTON

ABSTRACT

FACULTY OF PHYSICAL SCIENCES AND ENGINEERING

Optoelectronics

Thesis for the degree of Doctor of Philosophy

Development of Highly Efficient Thulium-doped High Power Fibre Lasers

Norberto Javier Ramírez Martínez

Thulium-doped fibers pumped with ~790nm high power diodes have the potential to enable a cross-relaxation process to achieve two excited ions into the $^3F_4$ manifold for one pump photon (two-for-one cross-relaxation) when the fibre core composition including the thulium concentration is optimized. This has the advantage of reaching thulium-doped fibre laser quantum efficiency up to 200% in the two-micron band. Therefore, the development of thulium-doped fibres is a key parameter to exploit laser efficiencies that can exceed the Stokes limit (>40%).

The thulium-doped fibres used in this thesis were fabricated in an aluminosilicate host using the well-known modified chemical vapour deposition process in combination with a hybrid gas phase solution doping technique. This novel fabrication method takes advantage of a conventional solution doping technique in which high purity rare-earth precursors that have low vapour pressures at room temperatures up to several hundred degrees Celsius can be used and at the same time by using a gas phase deposition process and high aluminium concentrations can be reached in the fibre core, which is otherwise not possible using the solution doping technique. Furthermore, fibres fabricated using this hybrid approach show more homogeneous and flat-top dopant profiles compared to fibres fabricated using the conventional approach where both aluminium and thulium are incorporated in the core through solution doping in the fibre core which helps to achieve a good laser efficiency in thulium-doped fibre lasers with ~790nm pumping.

Contrary to the generally held view of high thulium concentration for efficient fibres, this work demonstrates that a thulium concentration of about 3.5wt% with a more uniform dopant profile is sufficient to maintain superior laser performance with slope efficiencies >70% over a wide wavelength band of 1980nm to 2080nm and >50W output power.

In addition, for operation at longer wavelengths >2080nm, thulium-holmium co-doped silica fibres were fabricated to investigate the energy transfer mechanism from thulium to holmium, which thereby opens the opportunity for high power operation at longer wavelengths when pumped by ~790nm diodes. The hybrid gas phase-solution doping technique together with the modified chemical vapour deposition process used to fabricate the co-doped fibres allows a more uniform distribution of the interacting rare earth ions across the core region. As a consequence, an efficient two-for-one cross-relaxation process in thulium followed by an efficient energy transfer between thulium and holmium ions was obtained.

By optimizing the core composition and the concentration ratio of the dopants in thulium-holmium co-doped silica fibers, laser efficiencies >55% have been reached at an emission wavelengths of ~2100 nm and >37W output power, which has convincingly demonstrated the advantage of this approach and its considerable potential for power scaling.

List of Contents

List of Figures

List of Equations

List of Graphs

List of Images

List of Tables

Academic Thesis: Declaration of Authorship

I, Norberto Javier Ramírez Martínez, declare that this thesis and the work presented in it are my own and has been generated by me as the result of my own original research.

Development of Highly Efficient Thulium-doped High Power Fibre Lasers

I confirm that:

1. This work was done wholly or mainly while in candidature for a research degree at this University;
2. Where any part of this thesis has previously been submitted for a degree or any other qualification at this University or any other institution, this has been clearly stated;
3. Where I have consulted the published work of others, this is always clearly attributed;
4. Where I have quoted from the work of others, the source is always given. With the exception of such quotations, this thesis is entirely my own work;
5. I have acknowledged all main sources of help;
6. Where the thesis is based on work done by myself jointly with others, I have made clear exactly what was done by others and what I have contributed myself;
7. Parts of this work have been published as:

[1] N. J. Ramírez-Martínez, M. Núñez-Velázquez and J. K. Sahu, "Study on the dopant concentration ratio in thulium-holmium doped silica fibers for lasing at 2.1μm," Opt. Express28, 24961-24967 (2020).

[2] M. Núñez-Velázquez, N. J. Ramírez-Martínez and J. K. Sahu, " Development of Tm:Ho Co-doped Silica Fiber for High-power Operation at 2.1μm," in Conference on Lasers and Electro-Optics, OSA Technical Digest (Optical Society of America, 2020), paper STh4P.7.

[3] Norberto J. Ramírez Martínez, Martín M. A. Núñez Velázquez, Jayanta K. Sahu, "Efficient cladding pump Tm:Ho co-doped fiber laser for operation in the 2.1 microns region," Proc. SPIE 11260, Fiber Lasers XVII: Technology and Systems, 112600H (21 February 2020.

[4] N. J. Ramírez-Martínez, M. Núñez-Velázquez, and J. K. Sahu, "790nm Diode Pumped Thulium Sensitized Holmium-doped Fibre Laser Operating Beyond 2100nm," in 2019 Conference on Lasers and Electro-Optics Europe and

European Quantum Electronics Conference, OSA Technical Digest (Optical Society of America, 2019), paper cj_8_5.

[5] N. J. Ramírez-Martínez, M. Núñez-Velázquez, A. A. Umnikov, and J. K. Sahu, "Highly efficient thulium-doped high-power laser fibers fabricated by MCVD," Opt. Express 27, 196-201 (2019)

[6] N. J. Ramírez-Martínez, M. Núñez-Velázquez, A. A. Umnikov, and J. K. Sahu, "Efficient Thulium-doped Fiber Laser Operating in the 1890 – 2080nm Wavelength Band," in Advanced Photonics Congress, OSA Technical Digest (Optical Society of America, 2018), paper SoTu4H.3

[7] N. J. Ramírez-Martínez, M. Núñez-Velázquez, A. A. Umnikov, and J. K. Sahu, "Novel Fabrication Technique for Highly Efficient Tm-doped Fibers," in Conference on Lasers and Electro-Optics, OSA Technical Digest (Optical Society of America, 2018), paper SF3I.2

Signed:

Date: 21/01/2021

Acknowledgements

The following institutions are gratefully acknowledged for the support received during this research project.

- National Council of Science and Technology – CONACyT México (Consejo Nacional de Ciencia y Tecnología) award: CVU743592.
- UK Engineering and Physical Sciences Research Council award: EP/N00762X/1.
- Optoelectronics Research Centre, University of Southampton.
- Faculty of Engineering and Physical Sciences, University of Southampton.

To my mom, for being the best example I have ever had of hard working and continuous improvement. For always encouraging me to go beyond and exceed my expectations.

To my sister, for being an example of perseverance and making me see that there are different ways to get to the same place. For always been there for me despite the distance, pushing me to reach my goals and go further.

To all my friends, for your help, support and patience. Regardless of how close or far we are, you have been there in the good and bad moments. For encouraging me to continue on this path even when the light at the end of the tunnel was too far away either with a call, a message or with a couple of beers at the pub.

To my supervisor Prof. Jayanta Sahu, for giving me the opportunity to do my PhD and for your support, guidance, teaching and useful criticism during the last four years.

Definitions and Abbreviations

All the units in this document are given under the International System of Units, its derived units, multiple and sub-multiples, unless otherwise specified in the text.

The preforms and fibres refractive index are given at a wavelength of 633nm unless a different wavelength is specified in the graph.

Al: aluminium

CDS: Chelate Deposition System

clad: cladding

COC: cyclic olefin copolymer

CR: cross relaxation

Δn: refractive index difference

EDX: Energy Dispersive X-ray spectroscopy

ET: energy transfer

F300: high-quality quartz substrate from Heraeus Group

FBG: Fibre Bragg grating

FRIP: Fibre Refractive Index Profile

FUT: Fibre under test

HDFL: holmium-doped fibre laser

HGSD: hybrid gas phase-solution doping

High Power: >50W

IFA: multiwavelength fibre refractive index profiler from Interfiber analysis, LLC

MCVD: modified chemical vapour deposition

MeOH: Methanol (CH_3OH)

NA: Numerical Aperture

NIR: near infra-red

2-micron region: 2μm band + 2.1μm band

OH: hydroxyl functional group.

ORC: Optoelectronics Research Centre

OSA: Optical Spectrum Analyser

P: phosphorous

PC: polycarbonate

PK2600: preform refractive index profiler from Photon Kinetics, Inc.

PMMA: polymethylmethacrylate

ppm: part per million

PRIP: preform refractive index profile

RE: Rare earth (Tm: thulium; Ho: holmium; Yb: ytterbium; Er: erbium)

RIP: Refractive Index Profile

SD: Solution Doping

TDFL: thulium-doped fibre laser

THDFL: thulium:holmium co-doped fibre laser

thd: 2,2,6,6-tetramethyl-3,5- heptanedionate

TIR: total internal reflection

UV: ultra-violet

WLS: white light source

wt: weight

η: efficiency

η_A: efficiency with respect to absorbed pump power

η_L: efficiency with respect to launched pump power

λ: wavelength

Chapter 1 Introduction

This chapter introduces the rare earth-doped fibre lasers used within this region, their advantages or possible limitations, the fabrication route to follow for rare earth-doped fibre production as well as some of the main problems faced during the fabrication process. Additionally, the outline of the thesis is presented.

1.1 Overview

A rare earth-doped fibre laser is an optically pumped laser that uses an optical fibre as a gain medium and an external source of radiation that emits photons to excite the rare earth ions contained within the core the fibre[1]. As a consequence, they are able to convert the pump photon wavelength to longer or shorter wavelengths. For operation in the two microns region, thulium-doped fibres and holmium-doped fibres are usually the preferred choice[2].

The two main pump bands for thulium-doped fibres are ~790nm and ~1550nm[3]. Pumping with 1550nm sources has the benefit of lowering the quantum defect with high laser efficiency and low threshold. However, laser diodes at this wavelength and with an output power >10W are not commercially available, so the preferred pumping scheme uses erbium-ytterbium co-doped fibre lasers, which reduces the overall optical efficiency of the system[4].

Compared to the 1550nm pumping, the absorption band located at ~790nm overlaps with commercially available high power pump diodes[5], which under specific circumstances, such as having an optimized glass host material and dopant concentration within the core, can enable a two-for-one cross-relaxation process[6,7]. This phenomena allows to achieve two excited ions into the ground energy level for one pump photon, reaching a quantum efficiency up to 200% in the 2μm band[8].

Similarly to thulium-doped fibres, holmium-doped fibres laser systems can be pumped either by ~1150nm or ~1950nm sources[9-11], resulting in high efficient operation at wavelengths around the 2.1μm band[12]. However, direct pumping cannot be performed due to the fact that the absorption bands of interest lie where high power diodes are not available. Therefore, holmium-doped fibres are usually pumped by ~1950nm pump sources (TDFLs) by using the in-band pumping scheme[13]. Moreover, the laser efficiency of ~790nm diode pumped TDFLs operating at ~1950nm is somewhat less than when operating beyond 2μm, and as a result of

this, the overall electrical-to-optical conversion efficiency of lasers operating at 2.1μm could suffer[14].

Moreover, the implementation of this pumping scheme brings additional complexity to fibre fabrication due to the need for an all-glass fibre structure with a fluorine doped cladding for low-loss pump guidance, as low-index polymer used in standard double clad fibers will incur a strong absorption in the 2μm band[15].

An alternative approach is to use thulium as an absorber of the laser diode radiation and co-dope the holmium-doped fibres, allowing a direct diode pumping at 790nm and promoting the two-for-one cross-relaxation process in thulium, followed by a dominant donor-acceptor energy transfer mechanism from thulium ions to holmium ions to extend the emission wavelength >2.1μm[16,17].

One of the most common fabrication techniques to fabricate rare earth-doped fibres is the well-known modified chemical vapour deposition process in combination with the solution doping technique. This method is widely used in industry as well as in research to manufacture a range of high performance optical fibres[18].

The MCVD process is based on the oxidation of chemical compounds such as $SiCl_4$, $GeCl_4$ and $POCl_3$ with high vapour pressure at room temperature (~20˚C) carried by a controlled oxygen flow and injected into a rotating substrate. These chemicals interact with an external energy source, usually an oxygen/hydrogen burner to produce soot particles which are deposited on the inside wall of the tube. Due to its flexibility, the core composition can be modified depending on the chemical flow and temperature of reaction whereas the core thickness can be controlled by the number of deposited layers[19].

However, when the time comes to incorporate rare earth compounds, the low vapour pressure that can be produced at room temperature limits the use of a vapour deposition method[20]. To overcome this limitation, the solution doping technique is considered, allowing the incorporation of high purity rare earth precursors by soaking the substrate tube in a solution containing rare earth chlorides[21].

1.2 Motivation

The wavelength range around two microns is part of the well-know "eye safe" region starting from 1700nm to 2200nm[12,22]. In the last decade, the development of high power fibre lasers emitting in the 2μm and 2.1μm band has been under investigation, with output power now reaching the kW level[2,23,24]. Lasers operating in this spectral region have shown exceptional advantages in applications such as medicine material processing and remote sensing[25-27], among others.

Recently, the use of thulium-doped fibre lasers for lithotripsy has generated significant interest due to the high absorption of liquid water and biological protein components available in the intercrystalline spaces of the kidney stones[28]. Therefore, kidney stones undergo thermal expansion and vaporization during laser lithotripsy, thus contributing to the fragmentation of stones that can be cracked into pieces small enough to pass out the urinary track. The absorption coefficient of liquid water at room temperature (22˚C) in the near infrared range points out the different two-micron laser sources used in this medical procedure and is shown in Graph 1[29].

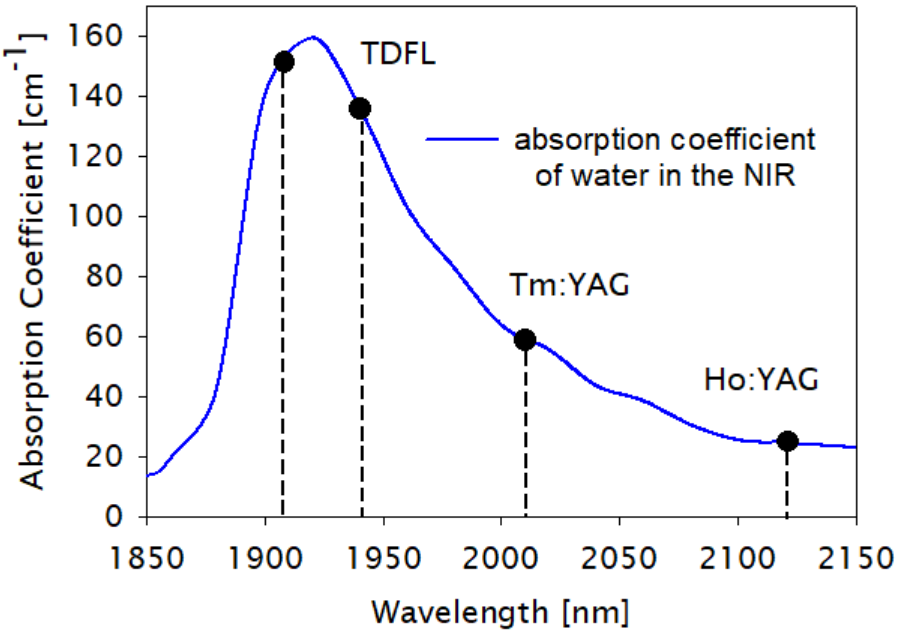

Graph 1. Absorption coefficient of liquid water at room temperature (22˚C)[29]

Holmium:YAG lasers have been applied to lithotripsy for more than two decades, however, they do not have suitable absorption bands in the traditional diode laser window of 780nm to 980nm, making this systems more complex compared to the fibre laser technology[30].

In contrast, thulium-doped fibre lasers sources can be directly pumped by ~790nm high power laser diodes and can be co-doped with holmium in order to operate in the 2μm and 2.1μm band. Moreover, it has been studied that thulium-doped fibre lasers produced higher stone ablation rates and smaller stone fragments than Holmium:YAG lasers[31].

1.3 Outline of the thesis

Chapter 2 provides the technical background for the development of highly efficient high power fibre lasers for the 2μm region applications. Here, basic laser concepts are presented to help the reader understand the principal mechanisms behind the ion-ion interactions that produce specific lasing characteristics and the general considerations for the design of a rare earth-doped fibre laser. Furthermore, the fabrication process and fabrication conditions, particularly for thulium-doped fibres is explored. Finally, the characterisation techniques used to evaluate the performance of the rare earth doped fibres are described.

Chapter 3 presents an all vapour phase doping technique for the incorporation of high aluminium oxide content into the preforms fabricated in combination with the MCVD technique. The experimental work reports the fabrication and characterisation of aluminosilicate-doped fibres with high aluminium oxide concentration, which is difficult to achieve using the conventional solution doping technique.

In chapter 4, the development of a hybrid process by combining both a vapour phase and solution doping techniques for thulium-doped preform fabrication in conjunction with the MCVD technique is presented. This novel fabrication route takes advantage of co-doping silica with high aluminium concentration and high purity thulium precursors, making this fabrication method compatible with most of the existing manufacturing processes. The demonstration of preforms fabricated using the hybrid process are reported as well as the characterisation from the resultant fibres.

Chapter 5 discusses the fabrication and laser performance of thulium and thulium-holmium co-doped silica fibres when cladding pumped at ~790nm is used to extend the emission spectrum to the 2.1μm region. By using the hybrid gas phase-solution doping technique, the doping concentration and the Tm:Ho ratio were varied to study the energy transfer efficiency from Tm^{3+} to Ho^{3+}.

Chapter 6 is a brief description of ytterbium-doped fibres fabricated by an all vapour phase deposition technique. The fabrications, analysis and results were the basis for subsequent collaborations and industrial projects.

Chapter 7 shows the overall conclusion in the development of a novel fabrication technique for highly efficiency thulium-doped fibres and highlights the best results achieved during the completion of this thesis.

Chapter 8 presents the future directions of this work. Recommendations on the fabrication and laser performance in the development of high power thulium-doped fibre lasers are mentioned.

Finally, the appendices summarize all the preform fabrications done during the PhD programme and how the initial challenges during the building up of the laser set-up were overcome.

Chapter 2 Background

Rare earth-doped silica fibre fabrication has played an important role in optical communications and high power fibre laser applications. The new fibre compositions and fibre design have overtaken the standard fabrication techniques, leading to the creation of new fabrication methods with enhance fibre performance.

In this chapter, a brief introduction of the mechanisms occurring when light interact with matter is presented, followed by a description of the ion-ion interactions happening between rare earth elements for two microns applications. In addition, basic laser concepts will be discussed to help the reader have a better understanding of the thesis. Finally, insight into the modified chemical vapour deposition technique is provided as well as information about the different approaches to incorporating rare earth into the silica matrix.

2.1 Interaction of light and matter

From a quantum perspective, light consists of particles called photons which carry electromagnetic energy and momentum. A photon may interact with an atom if its energy matches the difference between two atomic energy levels, leading to three principal mechanisms when talking about light interactions: absorption, spontaneous emission and stimulated emission[32].

If an atom is in its lower energy level, a photon may transmit its energy to the atom and raise it to a higher energy level. This process is induced by the photon and is called absorption. Similarly, if the atom is in a higher energy level, the photon may stimulate the atom to experience a transition to the lower level, resulting in the creation of a second photon whose energy is equal to the difference between the atomic energy levels. This process is called spontaneous emission because the transition is independent of the number of excited photons[33].

As presented in Figure 1, if we consider a two level energy system, the absorption of a photon with a specific energy leads to an upward transition of the atom from the ground level to the excited level. Inversely, if the atom is in the excited level and it contains a photon, the atom may be induced to emit another photon with

precisely the same characteristics as the original as it undergoes a downward transition. This process is known as stimulated emission.

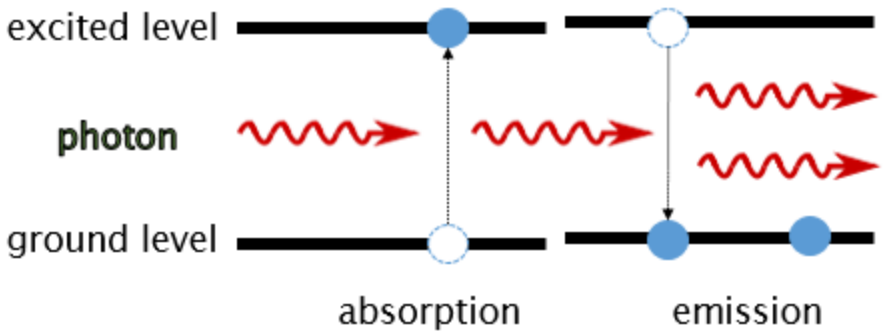

Figure 1. Stimulated emission process

This photon amplification process and the specific conditions of a gain medium that favours the stimulated emission over absorption and spontaneous emission underlies the operation of laser systems, which will be discussed in subsequent sections.

2.2 Basic laser concepts

2.2.1 Principle of lasing

The principle behind lasers is light amplification by stimulated emission of radiation. The stimulated emission allows a photon to induce an atom whose ion is in an upper energy level to undergo a transition to a lower energy level emitting a photon with the same characteristics as the initial photon. These two photons serve to stimulate the emission of two additional photons and so on[34]. At thermal equilibrium, the probability of stimulated emission is much lower than that of spontaneous emission; therefore, most of the conventional light sources are incoherent. In order to increase the process of stimulated emission for getting coherent light, it is necessary to go beyond the thermal equilibrium by creating a condition called population inversion. This condition cannot be attained in a two energy level system as it is in thermal equilibrium[32].

2.2.2 Population inversion

In a three energy level system, a pump photon will excite an atom from the ground level and take its energy to a higher level, where usually it will also have a short lifetime. Subsequently, it will spontaneously decay in a non-radiative process to a lower level with longer lifetime[35]. This energy level is commonly known as

metastable level. As the lifetime from the higher energy level is shorter than the metastable level, the ions will be accumulated in the metastable level holding the excitation energy and building up a population inversion as the population in the ground level will be exceeded[36]. Figure 2 shows a simplified three energy level diagram.

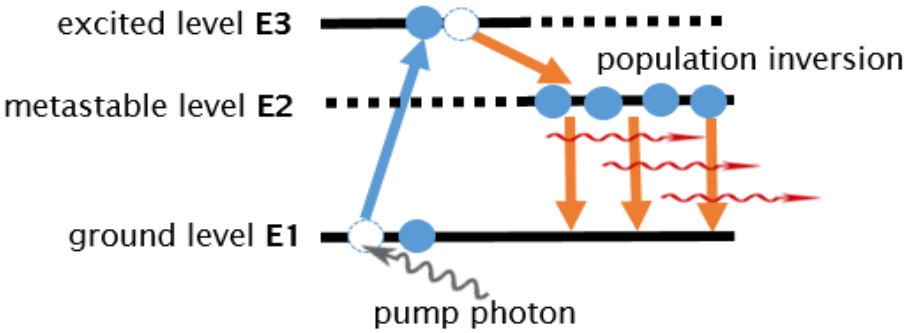

Figure 2. Simplified population inversion process

2.2.3 Lifetime

After excitation, the ions will remain in an excited state before returning to the ground state. This time during which the ions stay in the excited state is known as lifetime, where deactivation of the ions involves radiative and non-radiative processes[37]. It is supposed that the lifetime should be measured independently of the other processes that deactivate the ion. However, since the processes occur at the same time as the radiative, it is almost impossible to measure them in a separate way[38].

The fluorescence lifetime is the characteristic time that an ion remains in an excited state prior to returning to the ground state and is an indicator of the time available for information to be gathered from the emission profile. It is defined as the time in which the initial fluorescence intensity of an ion decays 1/e of the initial intensity[33,39] as shown in Figure 3.

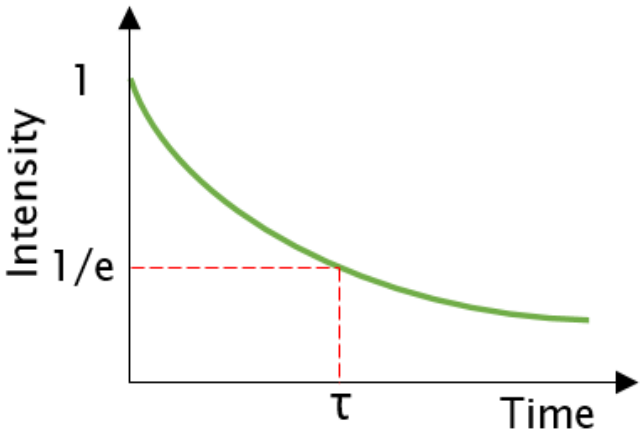

Figure 3. Characteristic fluorescence decay

In order to measure the lifetime in an optical fibre, an excitation source with high repetition rate pulsed output as well as filters (if needed) and detectors to capture the photon emission of the fibre that is repeated several times per second is required. It is important to mention that in order to avoid unwanted energy transfer processes between energy levels, it is preferred that only a small fraction of the ions from the ground state are excited by using short excitation pulses from the source with low pulse energy[40]. Therefore, the fluorescence lifetime measurement will have minimal signal degradation and as the excitation pulses change from an ON and OFF state by the source, the background noise is largely neglected.

Equation 1 describes the decay of fluorescence intensity as a function of the time excited by a short pulse of light, where I(t) is the fluorescence intensity measured at time t, I(o) is the initial intensity observed immediately after excitation, and τ is the fluorescence lifetime.

$$I(t) = Io * e^{(-\frac{t}{\tau})}$$

Equation 1. Exponential decay mathematical model

2.2.4 Optical resonator

The laser is an optical oscillator. It comprises a gain medium, an optical resonator commonly known as laser cavity and an external supply of energy or pump source. The laser cavity includes two parallel mirrors in which the gain medium is surrounded to provide feedback of the light. One mirror is fully reflective whereas the other is partially reflective so that it allows some of the light to leave the optical cavity[32-34]. A basic schematic of a laser cavity is shown in Figure 4.

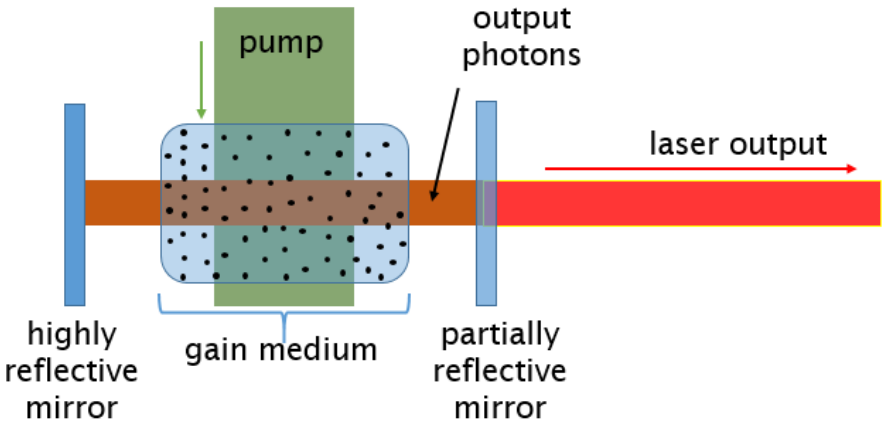

Figure 4. Schematic of a laser cavity

It is important to highlight that a laser can only operate if the gain is larger than the loss. Then, the power of the light in the laser resonator rises rapidly and starts to saturate the gain, taking the system into a steady state in which an output signal is produced.

2.2.5 Laser threshold and efficiency

When the power of the light in the laser resonator does not cause any gain saturation, the gain medium is below the laser threshold and only emits some luminescent light. This state is commonly known as small signal gain. The threshold of a laser is only reached when the small signal gain is equal to the total resonator losses[41]. These losses can be due to the mirrors that form the cavity, the absorption of the active medium or the losses per round trip of the laser resonator itself, among other causes.

Therefore, the optimization of the laser output power for a given pump power usually involves a compromise between a low laser threshold and a high slope efficiency[42].

The slope efficiency is defined as the slope of the curve obtained by plotting the laser output versus the pump power. This is calculated using Equation 2 and it represents the ratio of the converted energy into a laser output by the pump input energy.

$$\eta = \frac{\Delta\ Output\ power}{\Delta\ Pump\ power}$$

Equation 2. Laser efficiency

The pump power of the slope efficiency can be defined with respect to the launched or absorbed pump power depending on the application. For comparisons of the power efficiency, the launched pump power may be more relevant. However, for comparisons of the conversion efficiency and the intrinsic effects of the gain medium, the laser efficiency with respect to the absorbed pump power is more useful. Figure 5 shows an example of a slope efficiency curve.

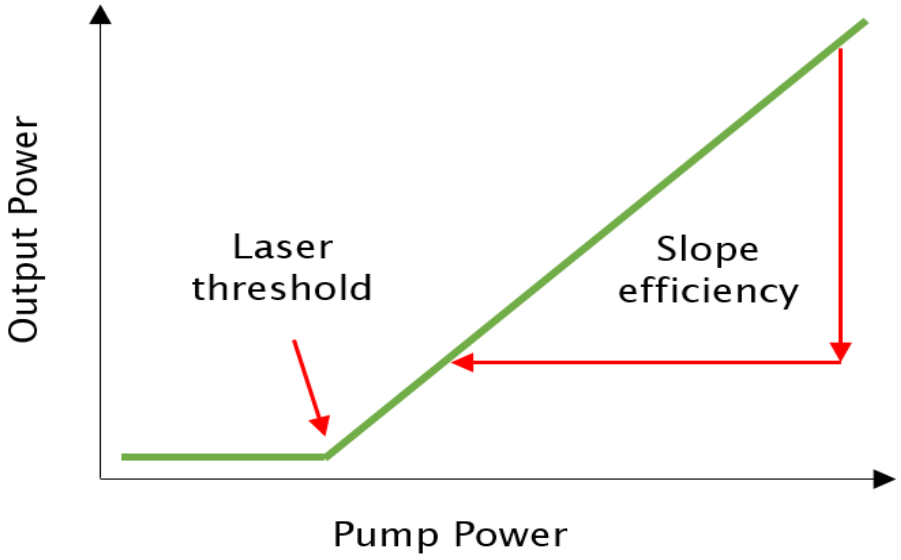

Figure 5. Characteristic slope efficiency curve from a laser source

For the purposes of this thesis, all the efficiency calculations were done with respect to the absorbed pump power.

2.3 Rare earths and the two-micron region

The lanthanides that comprise the series from Cerium (Ce) to Lutetium (Lu) of the periodic table are usually called rare earths elements as they were long ago thought to be rare[43]. However, these metals are very difficult to mine because it is unusual to find them in concentrations high enough for economical extraction[44].

The lanthanides usually exist as trivalent cations as the (3+) level of ionisation is the most stable for lanthanide ions[45]. For the purpose of this section of the thesis, Tm^{3+} and Ho^{3+} will be described as they are particularly important for laser applications in the two-micron region.

2.3.1 Thulium

Thulium is the second least abundant of the lanthanides and is widely studied for generating lasers in the two-micron region. The energy level diagram of the Tm^{3+}

ion and the different pump wavelengths that generate an emission in the two-micron region is shown in Figure 6.

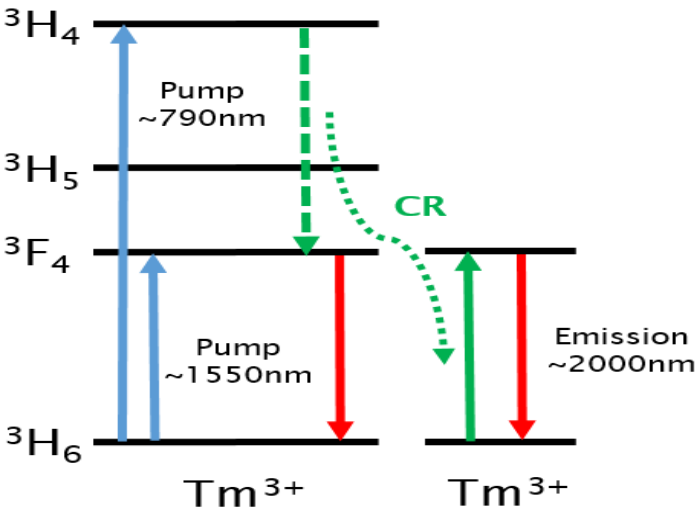

Figure 6. Simplified Tm energy level diagram

The Tm^{3+}: $^3F_4 \rightarrow {}^3H_6$ energy level transition can produce a wide laser emission in the longer side of the near infrared region from 1600nm to 2200nm[46,47], which can be addressed by either high power diodes at ~790nm or fibre laser pump sources at ~1550nm[48]. It is well known that the best method to pump an active medium is by choosing a pump wavelength which is close to the aimed wavelength due to the reduced quantum defect. However, in order to achieve the ~1550nm pump, an erbium-doped fibre or ytterbium-erbium co-doped fibres and additional high power diodes (980nm and 1450nm respectively) must be added to the system[3]. Alternatively, it is possible to pump thulium ions in silica matrix with ~790nm high power diodes. Under certain circumstance discussed in the following section, a two-for-one cross relaxation process can be produced[49].

It is worth mentioning that when the thulium concentration in a certain system is significantly low, the large interionic distance prevents any ion-ion interactions from taking place. However, when the thulium concentration is increased and the distance between ions is reduced, these ion interactions are more likely to happen[50,51]. For the purpose of this section of the thesis, the two-for-one cross relaxation process will be the only ions interaction mechanism described.

2.3.1.1 Two-for-one cross-relaxation

The well-known cross relaxation process might be consider as one of the most favourable mechanisms in thulium as it is possible to generate two excited ions

into the $^3F_4$ manifold for one pump photon when pumped by ~790nm diodes. When thulium concentration in a gain material exceeds ~2wt%, it is possible to reach quantum efficiencies greater than 100% of the $^3F_4 \rightarrow {}^3H_6$ two-micron lasing transition[5,6,49].

As shown in Figure 7, the process begins when an ion in the $^3H_6$ manifold (ground level) is pumped by a ~790nm high power diode to the $^3H_4$ manifold. Consequently, the excited ion in the $^3H_4$ manifold drops to a lower energy level ($^3F_4$), releasing energy in a non-radiative process. This energy is strong enough to excite an additional ion in the $^3H_6$ manifold and take it into a higher energy level with the same energy gap. Finally, the two excited ions in the $^3F_4$ manifold decay to the ground level, emitting in the two-micron region simultaneously[52-54].

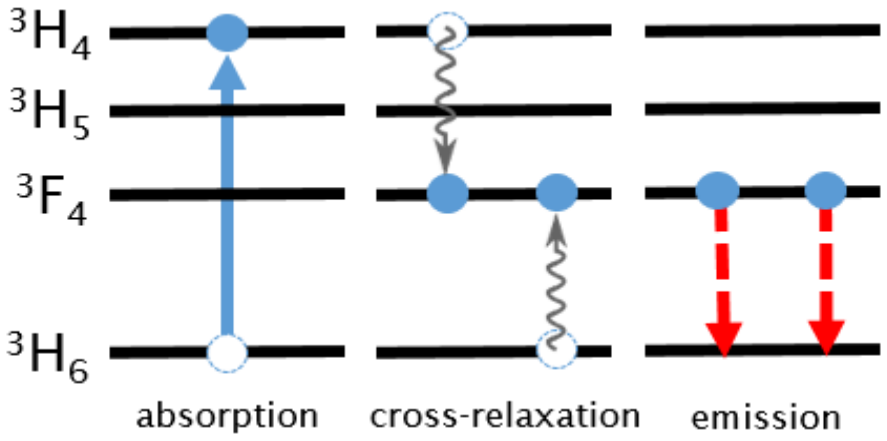

Figure 7. Simplified two-for-one cross-relaxation process

2.3.2 Holmium

Holmium is another lanthanide used for the generation of laser radiation in the two-micron wavelength region. Similar to other rare earths, holmium exists in only 1.3ppm of the earth's crust. Traditionally, in order to generate laser emission in the 2.1μm band, holmium can be pumped by thulium-doped fibre lasers at ~1950nm or by ytterbium-doped fibre lasers at ~1150nm[13,55]. The energy level diagram of holmium in silica host is shown in Figure 8.

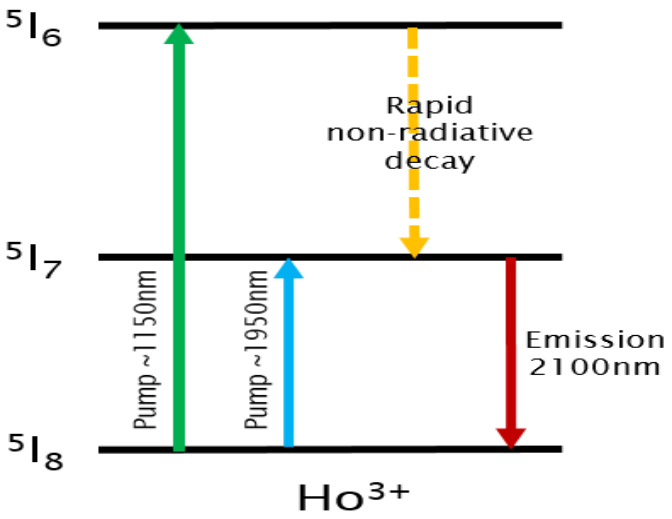

Figure 8. Simplified Ho energy level diagram

For the purpose of this section of the thesis, only the two lowest energy levels of holmium will be mentioned as they are an important element in the energy transfer from thulium to holmium described in the following section.

In singly Ho^{3+} silicate glasses, especially those containing moderate holmium concentrations, it has been reported that ion-ion interactions involving the $^5I_7$ manifold could be the cause of a reduction in the laser efficiency. Even though holmium glasses are usually doped with additional materials, the distribution of the dopants may not be uniform, leading to the formation of ion clusters. Nevertheless, holmium-doped silicate glasses have been fabricated without adverse effect and with promising results[56,57].

Holmium laser materials commonly incorporate additional rare earth elements such as thulium to work as a sensitizer, where under certain circumstances the sensitizer ion absorbs the pump energy and transfers it to an activator ion which lases.

2.3.2.1 Thulium-holmium co-doping

In order to reach the 2.1μm band and extend the available absorption wavelength in holmium, a co-doped system using thulium and holmium can be considered[58]. This approach will allow a direct diode pumping at ~790nm that can be utilized to excite thulium ions and promote the two-for-one cross relaxation process in

thulium, followed by a donor-acceptor energy transfer mechanism from thulium $^3F_4$ manifold to holmium $^5I_7$ manifold[59] as shown in Figure 9.

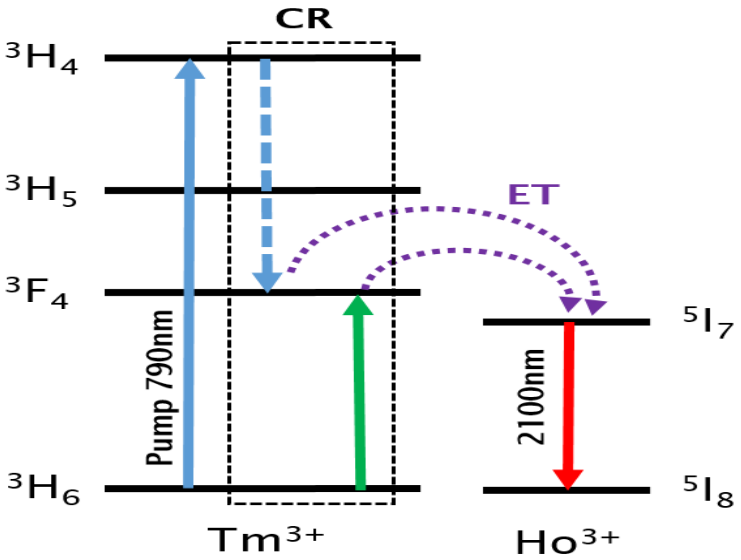

Figure 9. Tm to Ho energy transfer process

2.4 Rare earth doped fibre lasers

2.4.1 Principle of optical fibres

An optical fibre is a cylindrical dielectric waveguide made of a low loss material. It consists of a central core in which light rays are guided surrounded by a cladding with a lower refractive index. The optical rays are propagated in an optical fibre by total internal reflections within the fibre core if its angle of incidence at the core-cladding boundary is greater than the critical angle and remains the same as the ray bounces. Incident optical rays at angles greater that the acceptance angle are refracted into the fibre but are guided only for a short distance since they do not undergo to total internal reflection[60,61].

As the core-cladding boundary refractive index determines the range of angles within the light can be guided, the numerical aperture describes the light gathering capacity of the fibre and can be calculated with the refractive index profile of a preform or optical fibre[62] with the Equation 3.

$$NA = \sqrt{{n_{core}}^2 - {n_{clad}}^2}$$

Equation 3. Numerical aperture calculation

Numerous methods to measure the refractive index of a preform or fibre have been developed in recent years[63,64]. For the case of preforms, non-destructive techniques

has been under investigation, as sometimes the availability for speciality optical fibre preforms is limited. One of the most common techniques used in industry is to immerse the preform in a liquid with a known refractive index. Then, assuming that the preform is always circular, a laser beam is focussed across the diameter of the preform and its deflective angle at various points is measured. Consequently, it is possible to build up the refractive index of the preform by a direct comparison with the liquid refractive index[65]. For non-circular preforms, it has been reported that by using numerical processing of a set of deflection functions at different angular projections, it is possible to reconstruct a tomography of the refractive index profile and the outer geometry of the preform[66].

A schematic of a refractive index profile is presented in Figure 10.

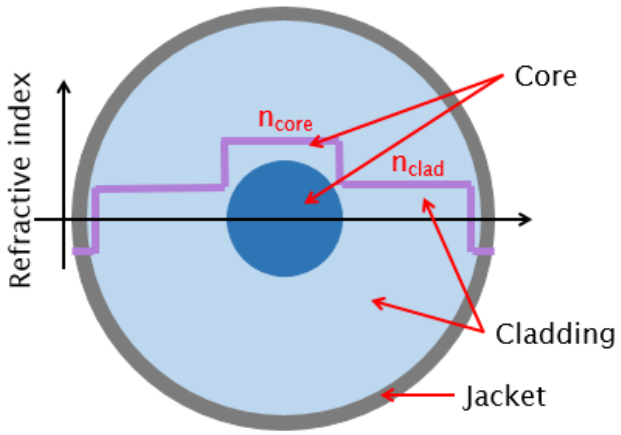

Figure 10. Schematic of an optical fibre refractive index profile

The optical rays are usually confined to the plane that pass through the fibre axis and reflect in the same plane without changing their angle of incidence (meridional rays). However, it is also possible that the optical rays propagate through the optical fibre without passing through its axis, intersecting the core-cladding boundary and following a helical path (skew rays)[32,61]. Figure 11 shows a schematic of an optical fibre and a cross sectional view of the skew rays' trajectories.

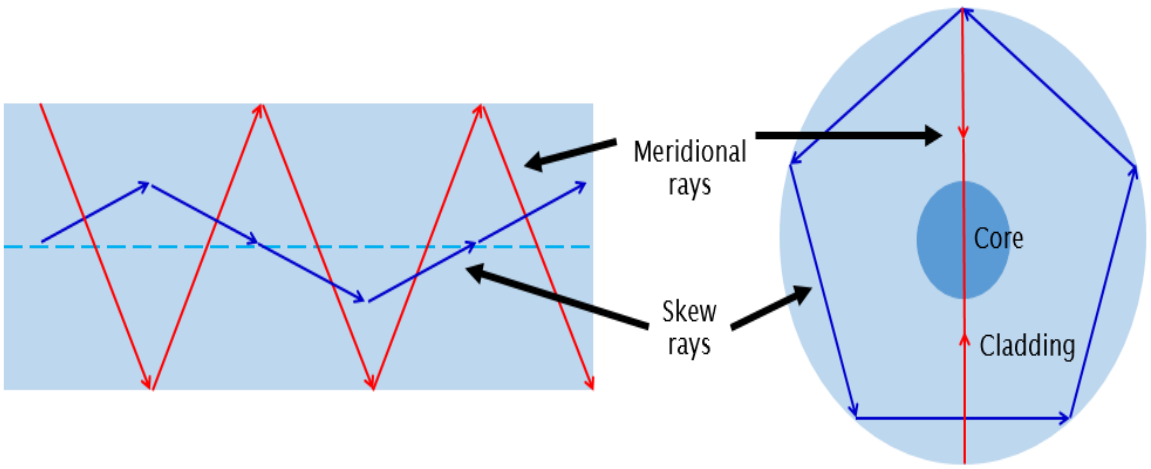

Figure 11. Meridional and skew rays trajectories in an optical fibre

2.4.2 Double clad fibres

A double clad fibre is an optical fibre that can propagate laser radiation in the cladding and the core simultaneously. In this kind of fibre, an inner cladding surrounds the core of the fibre, which is at the same time surrounded by an outer cladding with a lower refractive index[34]. This enables the inner cladding to guide light by total internal reflection in the same way the core does[67]. In the case of rare earth doped fibre lasers, the core is doped and acts as the gain medium. Figure 12 shows a schematic of a cladding pump double clad fibre.

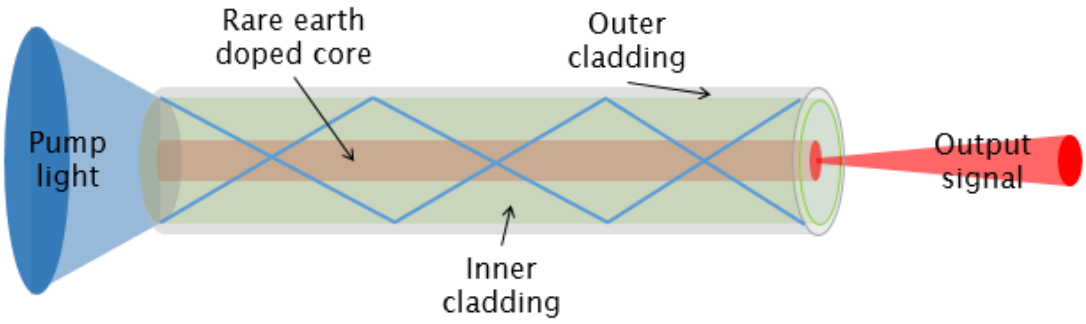

Figure 12. Schematic of a cladding pump fibre laser

As the pump light is launched into the cladding, the doped core gradually absorbs the cladding light as it propagates, driving the amplification process. However, some of the pump rays launched to the cladding do not overlap with the core of the fibre due to the circular symmetry in the fibre structure[68]; therefore, the pump is not efficiently absorbed.

These pumped skew rays can be mitigated by the use of coiling methods to modify the bend radius of the fibre and directly affect the mode mixing inside the inner

cladding, achieving a high spatial overlap with the core as shown in Figure 13. The advantages of using the coiling method have already been studied, experimentally tested and published in the literature[69].

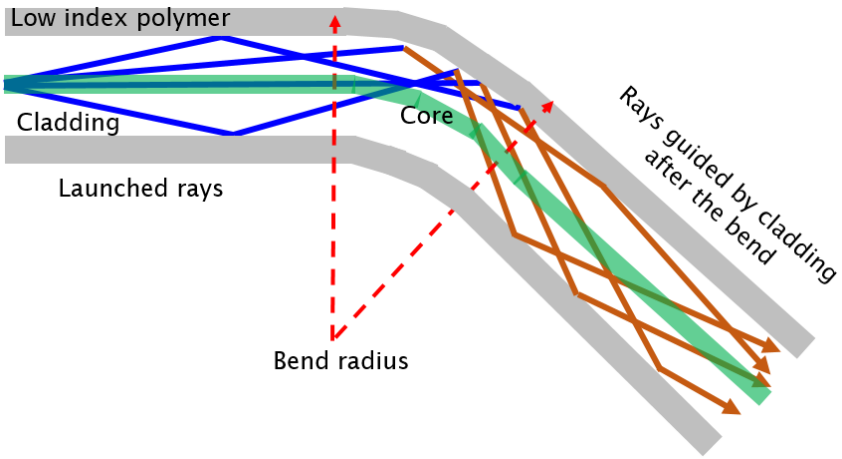

Figure 13. Skew rays after the coiling effect (fibre bending)

However, for optimized pump absorption for double clad fibres applications, it is necessary to modify the geometry of the fibre and break the circular symmetry of the fibre structure[70].

There are numerous geometric designs that break the symmetry of the fibre, such as rectangular, hexagonal, octagonal and D shapes, which are presented in Figure 14. These fibre geometries provide a noticeable improvement in terms of pump absorption efficiency compared to the conventional circular symmetry shape. However, it is important to consider also the shape of the fibre as it is usually spliced to conventional circular fibres. If the shape is not similar, it may cause adverse issues such as high splice loss and a reduction in the fibre performance[71].

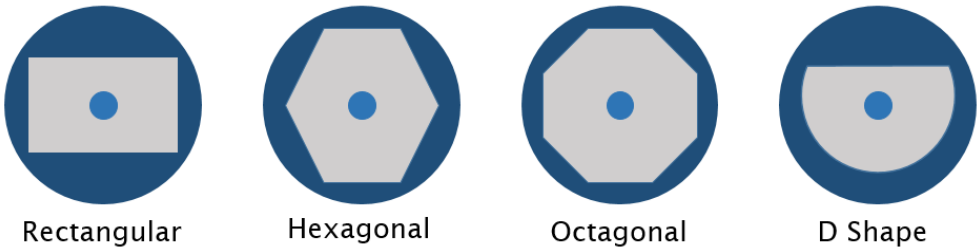

Figure 14. Cross sectional view of double clad fibres geometries

The most common approach to modifying the geometry and removing glass from the preform is to machine the circular surface of the preforms with a diamond milling, removing around 100µm to 200µm of glass in each pass. This milling process can be repeated multiple times until the reduction of the preform diameter is between 7% to 10%, depending on the fibre design. After the machining is

complete, the preform undergoes a fire polishing stage to smooth the surface and remove undesirable defects on the preform. Alternatively, it is possible to reshape the inner cladding by using a CO_2 laser to machine the preform. This approach enables the possibility for novel cladding structures as well as a reduction in the processing time.

The optimisation of the pump absorption efficiency, either by the use of a coiling method or the modification of the circular shape of the fibre, promotes the use of shorter lengths on double clad fibres for fibre laser and amplifiers.

2.5 Preform and fibre fabrication

2.5.1 Rare earth silica based fibres

Silica based optical fibres are composed primarily of silicon dioxide (SiO_2) which is an inorganic material commonly known as silica. Due to its high chemical purity and resistance, low thermal expansion and high transparency from the ultraviolet to the infrared spectral region, silica has been considered as an indispensable material by different industrial sectors[72,73].

However, fundamental limitations such as Rayleigh scattering[33] that exhibit the random density fluctuations due to irregular microscopic structure of silica and the OH incorporation have pushed the optical fibre industry to base their applications in the near infrared region[74,75]. The main vibration of the hydroxyl group in silica fibres is around 2.75μm with overtones at 0.72μm, 0.88μm, 0.95μm, 1.13μm, 1.24μm and 1.38μm[76,77]. Graph 2 shows the different fibre laser bands affected by the OH absorption in silica based fibres.

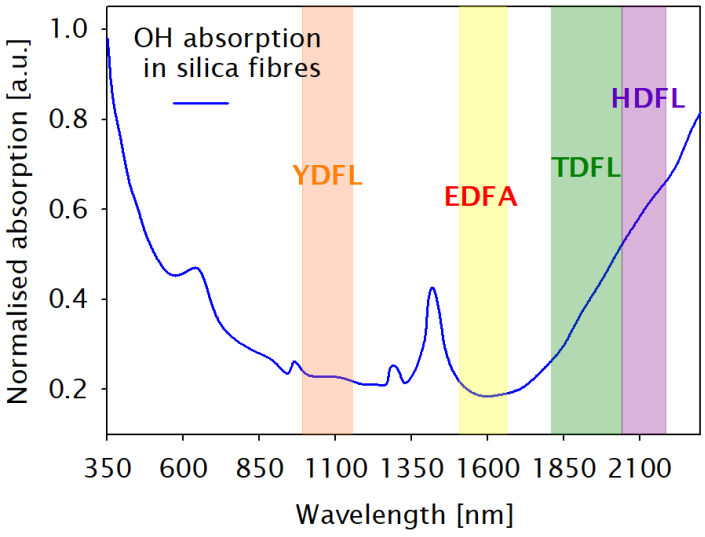

Graph 2. Hydroxyl group absorption in silica fibres[78]

To estimate the hydroxyl concentration in the fibres fabricated during this thesis we used the value of 50dB/km/ppm at 1380nm.

2.5.1.1 Glass host

The main target for the incorporation of rare earth ions into silica glass is to tailor the absorption and emission spectra, influence excited state properties and improve the glass forming characteristics[79,80]. Therefore, the addition of rare earth dopants to the silica matrix is essential for the development of fibre laser applications[18].

However, the highly polymerized structure of pure silica glass does not allow easy accommodation of rare earth ions even at low concentrations[72,73,81], thus network modifiers in the glass matrix are required to enhance the laser performance and reduce the undesirable clustering of the rare earth ions. Aluminium oxide and phosphorous pentoxide are the most common glass hosts used in the fibre laser applications to increase the rare earth solubility in silica and prevent clustering[82-84]. For the purpose of this thesis, aluminium oxide is the only network modifier used in the preform fabrication.

Aluminium oxide can be added to the silica matrix either in tetrahedral coordination as a network former or in octahedral coordination as a network modifier, making alumina a good candidate to be dissolved in silica[6,82,85]. While rare earth oxides dissolve well in alumina, alumina forms a solvation shell around the rare earth ions, allowing them to become soluble in the silica matrix[86]. Therefore, higher rare earth incorporation is possible whilst reducing the negative effects of clustering.

2.5.2 Modified chemical vapour deposition

The modified chemical vapour deposition is a process based on the vapour of chemical halides that react with oxygen on the inside of a rotating high-purity silica substrate tube. The mix of oxygen and vapour pressure of chemical halides such as silicon tetrachloride ($SiCl_4$), germanium tetrachloride ($GeCl_4$) or phosphorous oxychloride ($POCl_3$) are passed through a rotating tube and exposed to an external energy source, which is mounted in a MCVD lathe[19,87,88].

In order to transport these chemical halides to the deposition zone, the chemicals are kept in a liquid state inside a container called a bubbler. Then, a carrier gas is passed through the liquid precursor to generate bubbles. As the bubbles start to

break at the surface of the liquid, some vapour from these chemicals is generated and carried by a carrier gas flow which is normally oxygen. A schematic of a conventional bubbler is shown in Figure 15.

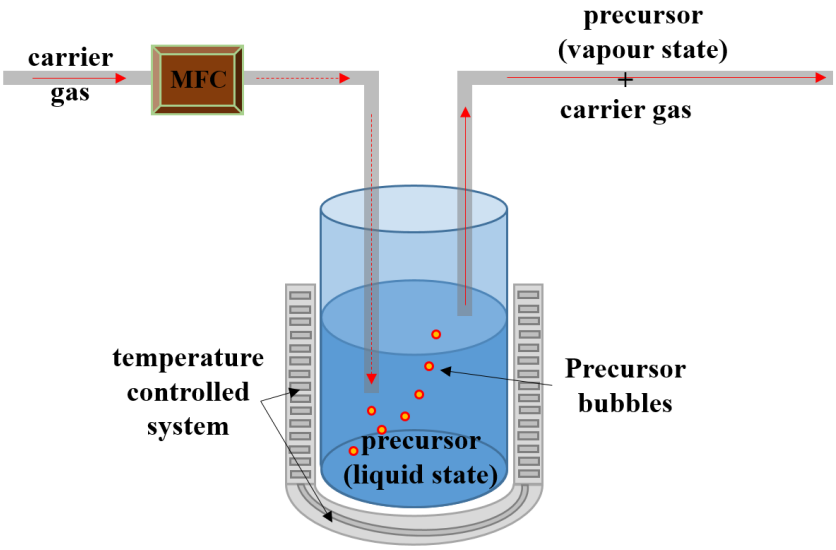

Figure 15. Precursor vapour delivery system (bubbler)

Table 1 shows the most common precursors utilized during the MCVD fabrication method as well as the generated product after oxidation.

Table 1. Precursors used in MCVD fabrication

Precursor	State	Delivery system	Product
$SiCl_4$	Liquid	Bubbler with O_2	SiO2
$GeCl_4$	Liquid	Bubbler with O_2	GeO2
$POCl_3$	Liquid	Bubbler with O_2	P205
BBr_3	Liquid	Bubbler with O_2	B2O3
SiF_4	Gas	Pressurised tank	High fluoride
SF_6	Gas	Pressurised tank	Medium fluoride

To control the amount of carrier gas flow, a mass flow controller (MFC) is utilized. It is important to mention that the mass transfer rate of the chemical halides will be influenced by the bubbler temperature, the bubbler pressure and the carrier gas flow rate. Figure 16 shows a schematic diagram of an MCVD system, including the glassware, the bubblers where the chemical halides are stocked in liquid state and the precursor delivery system.

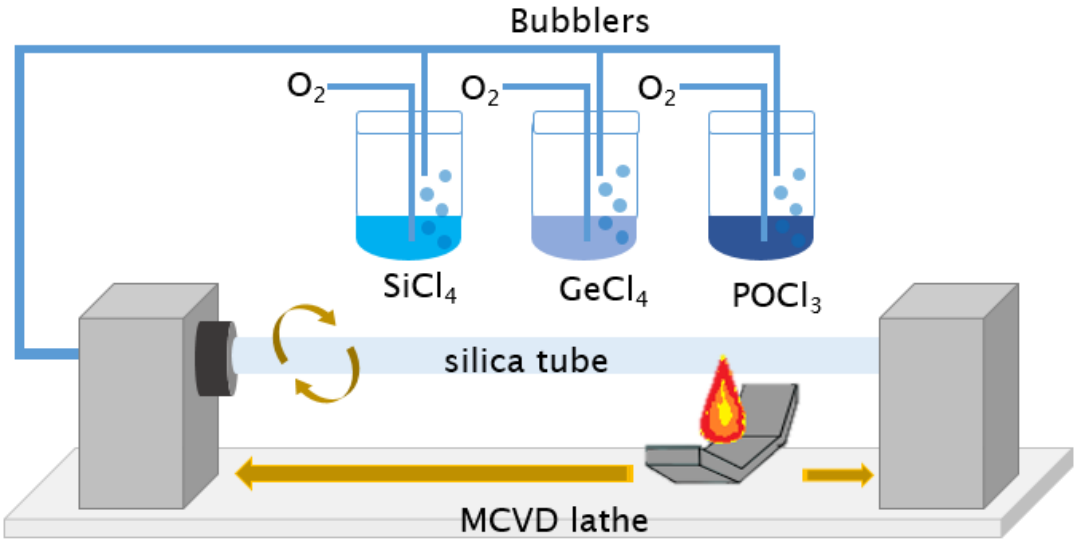

Figure 16. Schematic of MCVD system

Then, a homogeneous vapour phase reaction at high temperature takes place to form silica soot. These particles are driven to the cooler glass wall of the tube from the hot zone by the temperature gradient, where they are deposited on the inner surface of the tube. Depending on the speed, direction and temperature of the energy source, the soot particles can be deposited through different trajectories. As the energy source moves transversally, the reaction zone also changes position and sinters the silica soot to form a clear glass layer. This soot deposition mechanism is known as thermophoresis[89]. Figure 17 shows the vapour phase halides, the reaction at the hot zone, the creation and deposition of particles, and the sintering of the silica soot into solid glass inside a rotating glass tube.

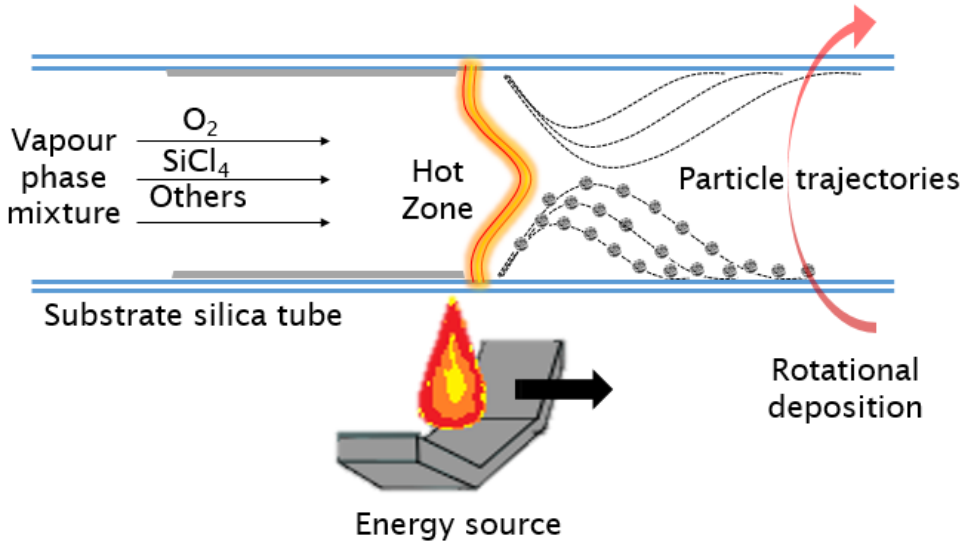

Figure 17. Thermophoresis mechanism

Finally, the silica tube is collapsed into a solid rod called a preform by surface tension and differential pressures between the inner and outer tube surfaces, while the tube rotates and preserves the cylindrical geometry.

2.5.3 Geometry modification

Normally, for high performance applications, the geometrical dimensions of the preforms are modified just after the MCVD fabrication process has finished and a combination of two techniques is applied: stretching of the preform and sleeving or jacketing of the preform.

The stretching technique is commonly used to adjust the size and length of the preform. As it is a technique which applies the conservation of the mass, similar to the fibre drawing, it is possible to modify the final dimensions of the preform by heating the glass near to the softening point and pulling the preform in a controlled manner as is expressed in Equation 4. Where r_1 and r_2 are the radius from the original preform and target preform respectively, V_b is the speed of the burner and V_p is the speed at which the rotating headstock needs to be pulled and, as the preforms are made of silica, ρ is the density of the silica.

$$\rho\pi {r_1}^2 2\, V_b = \rho\pi {r_2}^2 V_p$$

Equation 4. Controlled stretching

Following the stretching technique, the new preform is over jacketed with a high purity silica tube to modify the core/cladding ratio, where a combination of high temperature produced by the burner and an induced negative controlled pressure inside the bigger tube makes possible the fusion of the two glasses. This process is known as jacketing or sleeving.

Due to the limited dimensions available for high purity silica tubes, it is common to adjust the inner diameter of the tube so that it is sufficiently big enough to fit the solid preform and make the gap between the tube and the preform relatively small. The cross sectional area (CSA) of the initial tube can be calculated by Equation 5. Subsequently, it is possible to estimate the new inner diameter of the tube after the adjustment by Equation 6.

$$CSA = \pi \times {r_{OD}}^2 - \pi \times {r_{ID}}^2$$

Equation 5. Cross sectional are of a tube

$$\pi \times {r_{IDnew}}^2 = \pi \times {r_{ODnew}}^2 + CSA$$

Equation 6. Inner tube diameter calculation

Where r_{OD} and r_{ID} are the outer diameter and inner diameter of the initial tube and r_{ODnew} and r_{IDnew} are the new dimensions after the collapsing of the tube.

2.5.4 Vapour phase doping

Since the first preform fabrication by MCVD, numerous methods have been followed to incorporate rare earth ions into the silica glass structure without modifications on the MCVD system. However, the unavailability of liquid rare earth precursors at room temperature has limited this development[90]. Therefore, additional steps to the standard MCVD process and modifications to the system have been made to melt or evaporate the rare earth materials[91].

2.5.4.1 Rare earth chloride evaporation

Following the MCVD approach of transporting the chemical compounds to the hot zone, it is possible to melt high purity rare earth chlorides by adding an external heated chamber. By heating up the chamber to a controlled temperature above 1000˚C, it is possible to increase the vapour pressure of the fused rare earth chlorides. Then, with a mix of silicon tetrachloride and oxygen passing through the heated chamber, a controlled amount of rare earth can be integrated to the gas flow and delivered directly to the hot zone, building up a silica matrix doped with rare earth compounds[92]. However, rare earth dopant concentration levels are limited due to the high temperature required (>800˚C) to produce high vapour pressure[90].

A similar approach to this process is to place the rare earth chlorides within the substrate tube and close to the reaction zone, extending the temperature range up to several hundred degree Celsius[93]. Even though this alternative can generate higher vapour pressure from high purity rare earth dopants, there is no direct control of the flow or rate of evaporation.

2.5.4.2 Chelate deposition

An alternative to the rare earth chlorides is the use of certain compounds containing a ligand (typically organic) bonded to a central metal atom at two or more points called chelates. These precursor materials can be fluorinated to increase the volatility or unfluorinated[94,95]. However, the presence of fluorine compounds reduces the deposition efficiency by reactions that convert SiO_2 to SiF_4, which is volatile. It has been observed that unfluorinated chelates 2,2,6,6-tetramethyl-3,5- heptanedionate $(thd)_3$, normally called TRIS compound are thermally more stable, producing sufficient amounts of rare earth vapour pressure. From the literature, the vapour pressure from some rare earth chelate compounds when heated in the range of 150˚C to 220˚C[96] is presented in Graph 3.

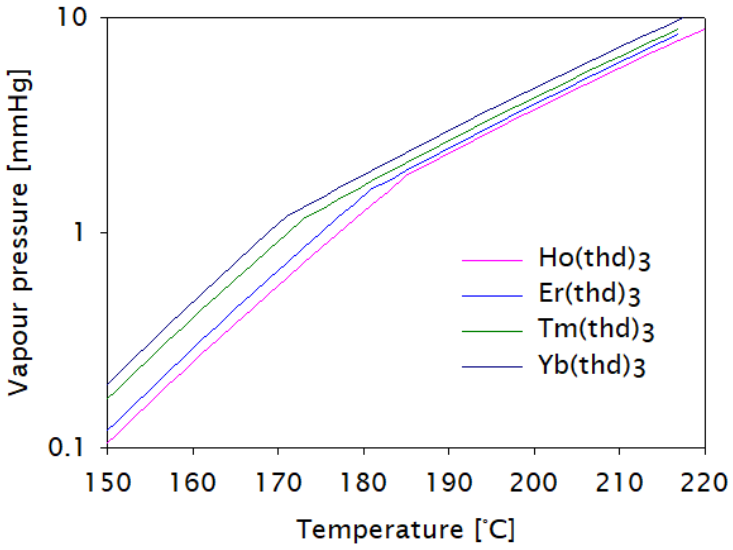

Graph 3. RE $(thd)_3$ vapour pressure as a function of temperature[96,97]

The vapour phase chelate delivery technique was first reported in 1990[98], where three sources of rare earth chelates were individually heated up to ~200˚C. Subsequently, the precursors were transported to the deposition zone by using helium as carrier gas and dedicated delivery lines, which were heated to prevent any early reaction until injection into the MCVD silica tube. Finally, a ribbon burner was provided under the entire length prior to the hot zone. Figure 18 shows a schematic of the rare-earth chelate delivery system.

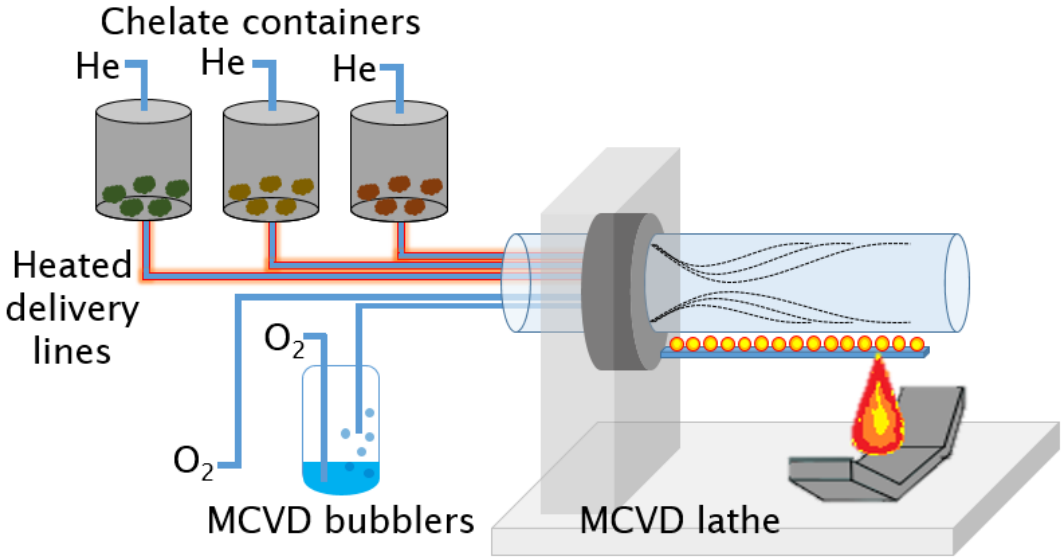

Figure 18. Schematic of a chelate delivery system[98]

Over the last two decades, similar configurations have been implemented in order to increase the rare earth concentration, to increase the number of doped layers during core deposition for Large Mode Area preform structures and to optimize the process technology itself[99-103]. However, despite of the possibility of generating vapour pressure at an accessible temperature of ~200˚C, it is still not enough when a rare earth concentration of >2wt% is needed.

2.5.5 Solution doping

Conventional dopants such as $SiCl_4$, $GeCl_4$ or $POCl_3$ can be incorporated into the silica matrix from the gas phase while other elements such as $AlCl_3$ and low vapour pressure precursors such as rare earth chlorides must be dissolved in a solution. Therefore, it is possible to immerse the silica substrate tube in a solution containing rare earth chlorides just after the silica soot is deposited in the MCVD process[21,84].

However, as the energy source moves transversally and sinters the silica soot, the solution containing rare earth chlorides cannot penetrate the clear glass layer. Thus, the temperature during the silica soot deposition must be reduced so that the sintering of the soot is incomplete and the glass layer left behind remains porous[104] as shown in Figure 19.

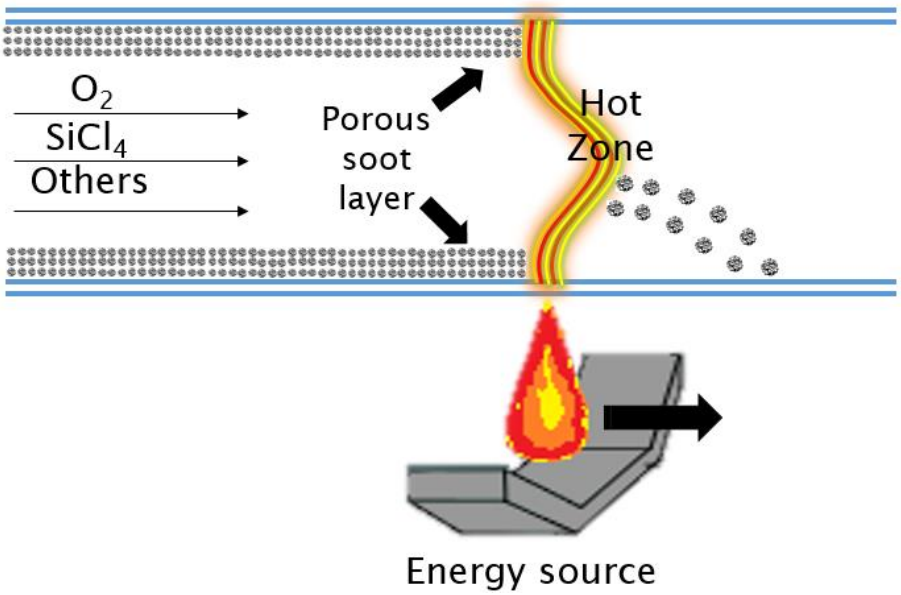

Figure 19. Thermophoresis mechanism with an enhanced porous soot layer

Then, the substrate tube with the porous soot layer is removed from the MCVD lathe and soaked vertically in a solution containing the rare earth chlorides. It is worth mentioning that the rare earth incorporation from a solution containing rare earth chlorides is controlled by the porosity and adhesion of the soot layer to the inner glass surface of the tube. If the temperature from the energy source is too high, the soot layer will be partially or totally sintered, decreasing the rare earth incorporation to the silica matrix. If the temperature is too low, the porous soot layer will not stick to the inner wall of the tube[105].

Subsequently, the solution is drained from the silica tube and reassembled in the MCVD lathe, where the soot is oxidised and sintered to form a clear glass layer with dopants. Finally, the tube is collapsed in the usual manner.

2.5.6 Fibre drawing

After the preform fabrication process is completed, the solid glass rod needs to be converted into a fibre by using a drawing tower. The essential components of this process are the preform feeding mechanism, a heat source to soften a portion of the preform and a fibre pulling. Furthermore, these three fundamental components must be aligned at all times[106]. Figure 20 shows a schematic of an optical fibre drawing tower, pointing out the key elements for optical fibre production.

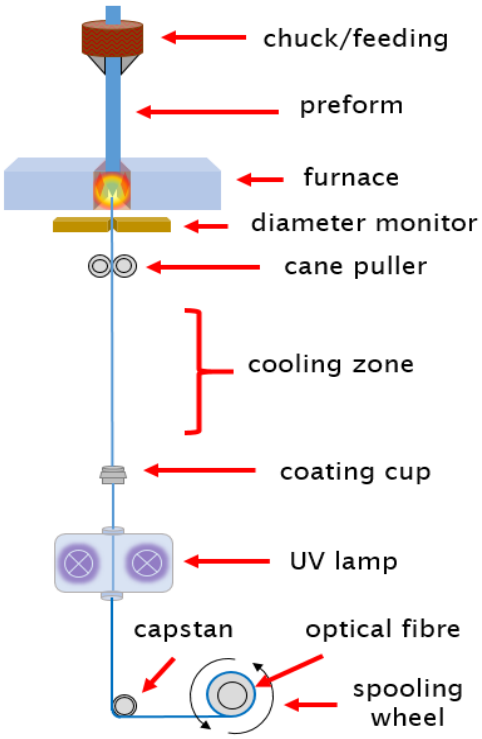

Figure 20. Fibre drawing tower diagram

The process starts by positioning the section of interest of the preform close to the hot zone of the heat source that provides a temperature increase in a controlled manner. For the purpose of this thesis, the heat source is a furnace with a graphite resistance that requires an inert gas atmosphere to prevent oxidation of the graphite element. Then, the furnace temperature is increased just above the softening temperature until the end of the preform falls by the effects of gravity[107].

From this point, the preform becomes naturally tapered, providing a transition to a smaller diameter. However, even if the diameter from the preform is reduced considerably (~20 times), the temperature of the glass just after the furnace exit can still be >100˚C. Thus, a cooling zone or a forced cooling system must be provided to cool down the resultant fibre before reaching any other element of the tower.

Subsequently, the fibre is passed through a coating cup containing an acrylate polymer to provide protection, flexibility and strength to the fibre as it is drawn and to provide an optical interface for double clad fibres. The coating is applied in a concentric layer and rapidly cured with a high intensity UV light by photo-polymerization[108].

Finally, the capstan and the spooling wheel collect the fibre where it is possible to vary the preform feed rate and the capstan speed to adjust the fibre dimensions and maintain a constant diameter.

Chapter 3 Vapour phase deposition: high aluminium-doped fibres

3.1 Introduction

It is important to add network modifiers such as aluminium oxide resides on the fabrication of rare earth doped fibres, since it has been shown that this prevents them from clustering and also allows the incorporation of higher levels of rare earth dopants to the silica matrix.

The solution doping technique is a method that can be used to fabricate rare earth doped fibres as an extension of the MCVD process. Due to its simple operation and versatility, it may be easy to increase the incorporation of aluminium oxide and so achieve higher concentrations levels of rare earth dopants by simply increasing the solution strength. However, it has been observed that the aluminium concentration over 4mol% tends to generate a core-cladding interface defect in the form of a star-like pattern, phase separation and formation of crystals when multiple solution doping stages are applied[109-113].

An alternative approach to solution doping is to disperse nanoparticles into the MCVD process[114]. In this method, alumina nanoparticles are used to lower the matrix phonon energy in rare earth ions vicinity and to prevent clustering[115]. It has been shown that the use of Al_2O_3 and other rare earth oxides nanoparticles improved the fluorescence characteristics of the fibres, as the nanoparticles form an optimized sub-micron environment around the rare earth ions[116]. However, the temperature for silica and Al_2O_3 processing is above 2000°C, which produces a high risk of nanoparticle decomposition and the unwanted formation of new phases during the MCVD fabrication process[117].Thus, the stability of this technique cannot be guaranteed.

It is possible to fabricate aluminium-doped fibres by a direct evaporation of chlorides with a vapour phase deposition process, obtaining doping levels beyond the standard solution doping method without core defects and enhancing bigger cores, better dispersion of the dopants and a more stable fabrication process.

However, the aluminium chloride used in the preform fabrication by solution doping is a hydrated form of the compound. Heating up this compound leads to an early reaction around 100°C, producing aluminium oxide. Thus, a temperature

of ~2500˚C is needed to generate sufficient vapour pressure for the deposition process. Alternatively, it is possible to use aluminium chloride in its anhydrous form, which can sublime just above the 100˚C with acceptable vapour pressure levels.

In this chapter, an all vapour phase deposition technique is presented. A set of aluminium-doped fibres were fabricated in order to study the effect of different aluminium concentrations, where the aluminium content exceeded the known limits >7mol%. The dopant distribution, showing a flat-top refractive index profile and uniformity along the length of the preform, is appreciated.

Moreover, as this is the starting point for a hybrid gas phase-solution doping technique, an aluminium-doped preform soaked in methanol and its characteristics is presented.

3.2 Experimental work

By using Equation 7, where P is the pressure in mmHg, T is the temperature in kelvin degree and A and B are specific constants previously characterised and available in the literature[96], it is possible to describe the relationship between the vapour pressure and the temperature of pure compounds and determine the trend that might exist in the thermodynamics of vaporisation.

$$logP = A - \frac{B}{T}$$

Equation 7. Antoine Equation[96]

However, due to the nature of the compounds themselves, a low pressure parameter set is used to describe the vapour pressure up to the normal boiling point and a second set of parameters is used for the range from the normal boiling point to the critical point. For this initial stage, the vapour pressure of the silicon tetrachloride and the aluminium trichloride going to the reaction zone were

calculated. Graph 4 shows the vapour pressure of these compounds at different temperatures.

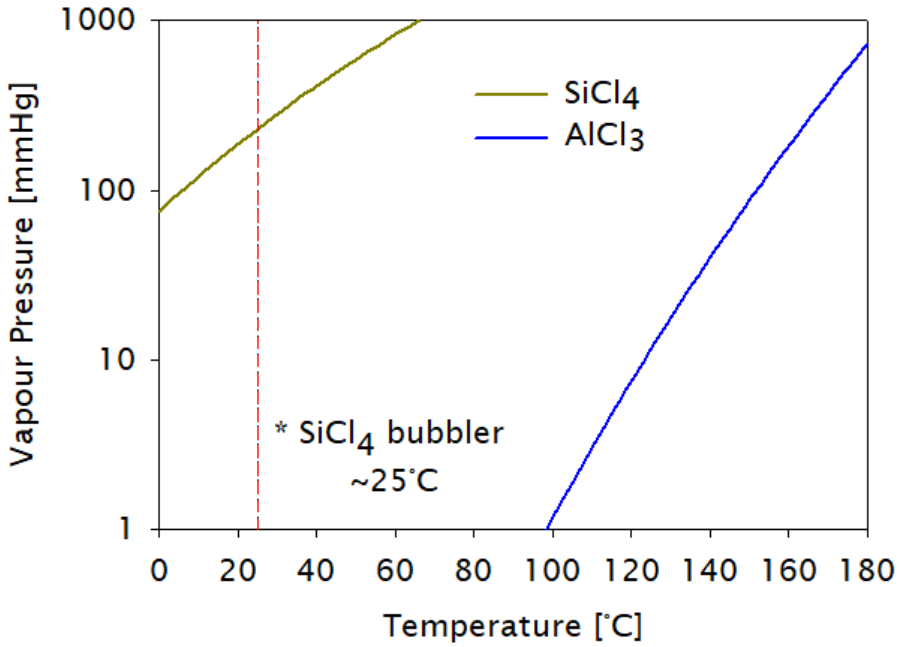

Graph 4. Chlorides vapour pressure as function of temperature

3.2.1 Preform fabrication

The aluminium-doped silica preforms were fabricated in an MCVD apparatus and a separate heated vapour phase delivery system, where the anhydrous $AlCl_3$ compound (Sigma-Aldrich, 99.999%) was placed inside a separate container and heated up between 100°C to 180°C to generate vapour pressure. By using helium as carrier gas, the aluminium chloride was transported to the reaction zone through a dedicated line. In order to prevent condensation in the system, all delivery lines were heated at approximately ~200°C. The process started on high quality silica tubes (F300 from Heraeus) with a nominal 20x16mm diameter and 500mm length.

First, the silica substrate tubes were cleaned in the MCVD lathe using sulphur hexafluoride (SF_6). Subsequently, a $SiCl_4$ gas flow of ~40sccm was carried into the reaction zone at high temperature. A transverse oxygen/hydrogen burner was used as an energy source to build up a fully sintered transparent layer as cladding. This first deposition layer is shown in Image 1, where it is possible to see the changes inside the glass tube due to different gas flow compositions.

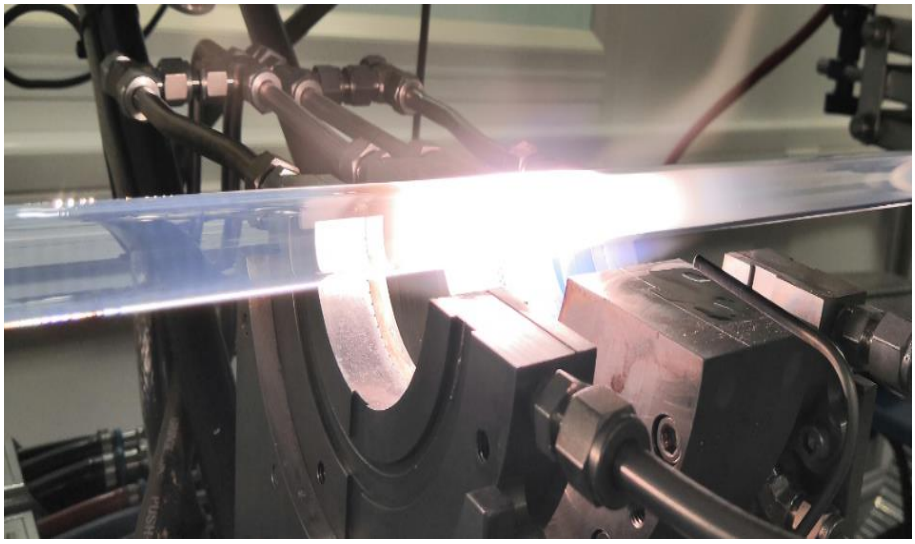

Image 1. MCVD process during $SiCl_4$ deposition

Then, the core layer was built up with a combination of ~50sccm of $SiCl_4$ and ~15sccm of $AlCl_3$ at 1950±10˚C as shown in Image 2. The temperature in the aluminium chloride container was varied in order to reduce or increase the dopant concentration.

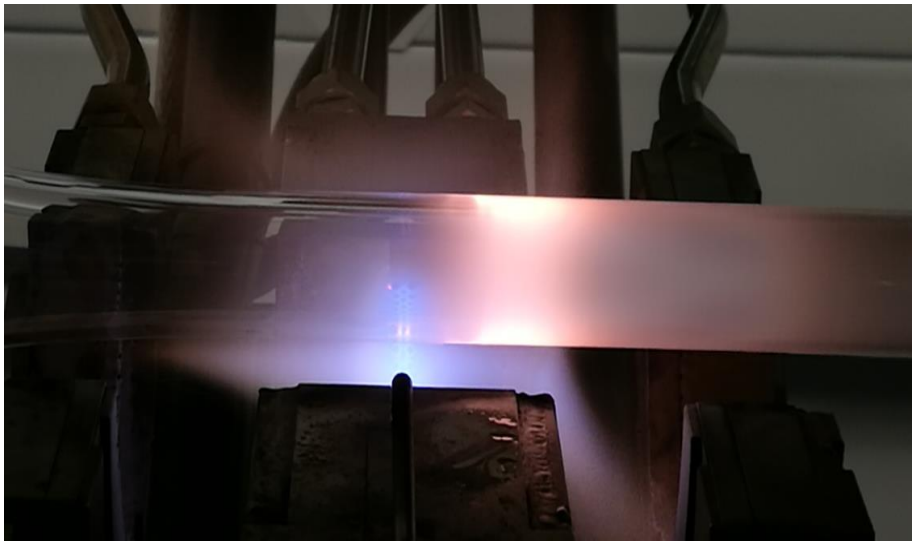

Image 2. MCVD process during $SiCl_4$ and $AlCl_3$ deposition (core formation)

After the core deposition, the tubes were collapsed above 2000˚C under O_2 atmosphere into preforms with an outer and core diameter of about 12mm and ~1.5±0.5mm respectively as can be seen in Image 3.

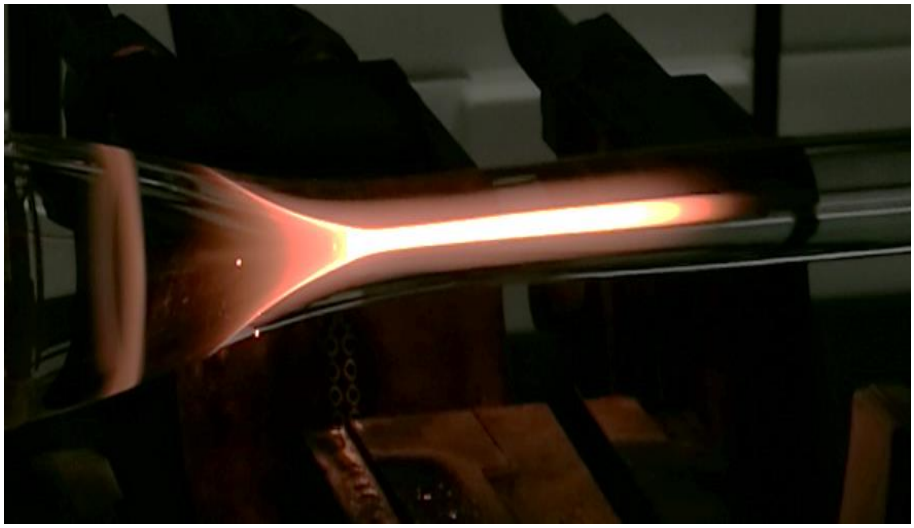

Image 3. Preform collapsing into a solid rod

3.2.2 Preform characterisation

The fabricated Al-doped preforms were targeted to contain Al_2O_3 dopant levels from 4mol% to 12mol%. The refractive index profile from each preform was analysed with a PK2600. All preforms showed no central dip and a flat top refractive index profile close to a step profile, which indicates a uniform incorporation of the Al_2O_3 across the core. Graph 5 shows the refractive index profile from the set of five fabricated preforms with their respective dopant concentrations. It is noticeable that high Al_2O_3 concentrations leads to wider core diameter and reduces the diffusion happening between the cladding and core.

When the Al_2O_3 concentration exceeds ~10mol%, a diminishing of the viscosity inside the tube was observed during the core deposition, however, since the burner turns off during each deposition pass, changing the temperature from a high to low level, the possibility of devitrification is neglected. Nevertheless, according to the SiO_2-$Al2O_3$ phase diagram, a change of phase can occur if the aluminium concentration is increased >20mol%, leading to an erratic behaviour during the deposition and instabilities within the core geometry.

This problem can be addressed by modifying the fabrication parameters during the deposition for further enhancement of aluminium content. However, in this case, the purpose of these fabrications was to establish a stable and repeatable process for the upcoming fabrication of thulium-doped fibres, thus the majority of this work has been directed using that approach.

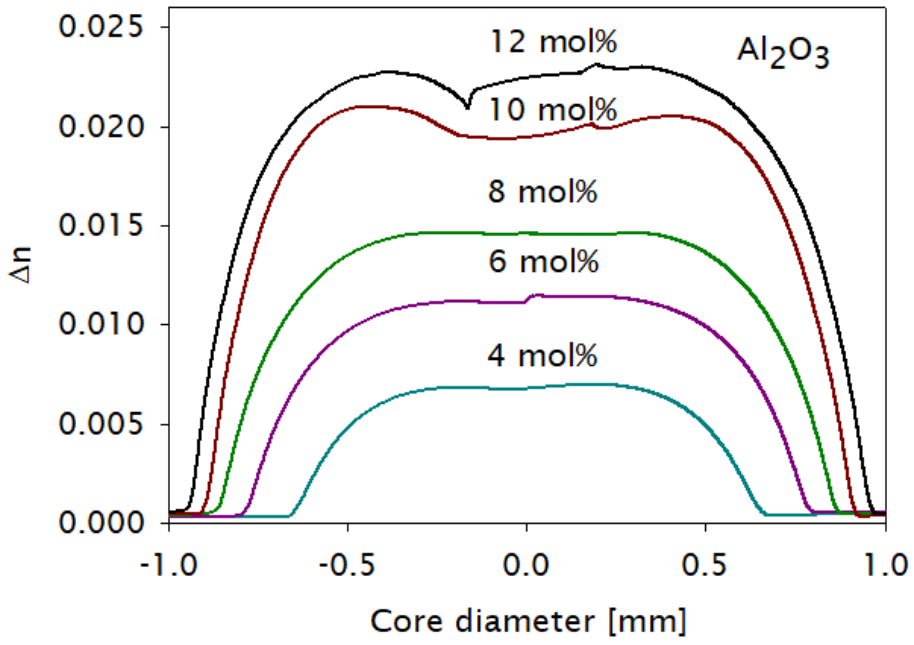

Graph 5. RIP from different Al-doped preforms (concentration increased)

The preforms were characterised every 60mm along the total length of the deposition. As observed in Graph 6, the preforms refractive index profiles are relatively uniform. For aluminium concentrations up to 8mol%, the RIP variation throughout the deposition length was ±0.0006 and for concentrations beyond 10mol%, the variation was ±0.002.

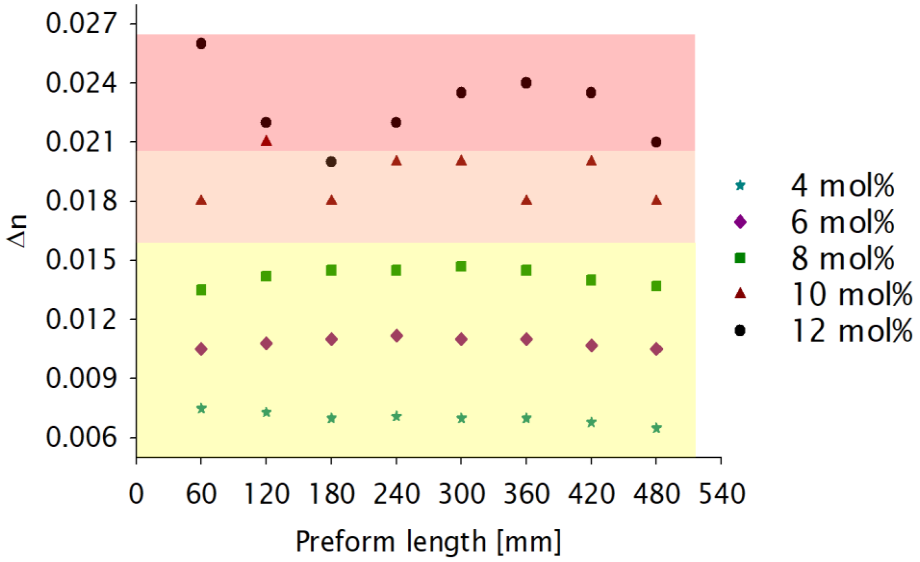

Graph 6. RIP stability along the preform (different Al concentrations)

Even the refractive index does not vary radically in all preforms, we suspect that aluminium concentrations above 12mol% will require further investigation when combined with other fabrication techniques, which is outside the scope of this thesis.

The results and analysis of this set of fabrications shows the effects of the aluminium incorporation by a vapour phase deposition technique, allowing a correlation between the gas flows and refractive index required to achieve a specific concentration as presented in Graph 7.

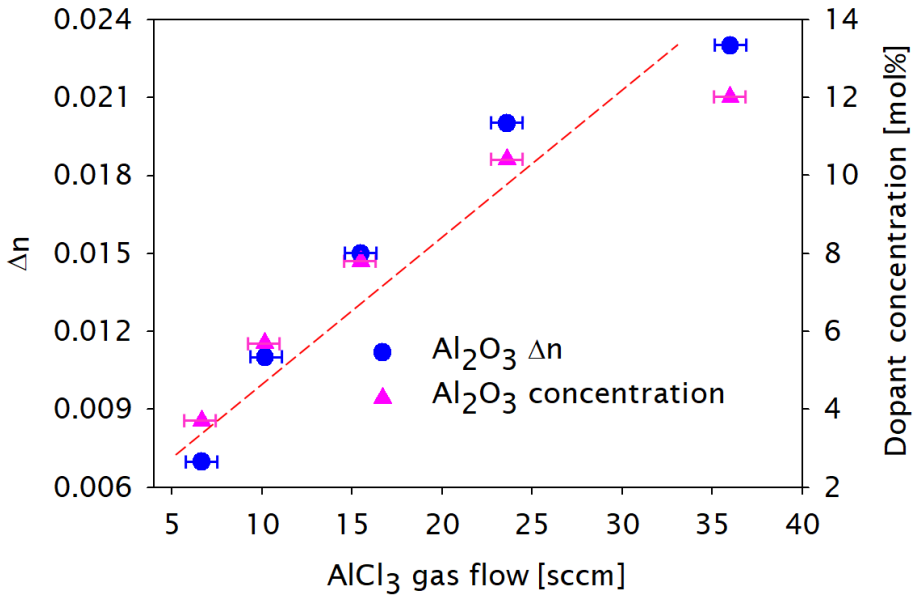

Graph 7. RIP and dopant concentration as function of $AlCl_3$ flow

3.2.3 Towards the HGSD technique

As the starting point of the hybrid gas phase solution doping technique (Chapter 4 and Chapter 5) and according to results that marked the limit for a stable process along the length of the preform, two aluminium-doped preforms with a refractive index of ~0.017 were fabricated. As aluminium is the only dopant incorporated to the silica matrix, it was possible to approximate the dopant concentration of the preforms as well as the $AlCl_3$ mass flow to be used during the process (extrapolated from the previous fabrications). The preliminary preform design characteristics are shown in Table 2.

Table 2. Al-doped preform design characteristics

Precursor	$AlCl_3$
Compound	Al_2O_3
Molar Mass	101.96 g/mol
Density	3.95 g/cm³
Total Δn required	0.017
Concentration (expected)	~9mol%
Molar Refractivity Ratio	1.9
Mass flow	30 – 60 mg/min

In addition, the expected preform dimensions were calculated and are shown in Table 3. As the objective with the preliminary fabrications was to compare the background loss characteristics from two preforms with the same parameters but different fabrication routes, the preforms were not post processed.

Table 3. Al-doped preform/fibre dimensions

Type of tube	Suprasil F300 (Heraeus)
Tube outer diameter	20mm
Tube inner diameter	16mm
Cross Sectional Area	113mm^2
Preform clad diameter (expected)	12mm
Preform core diameter (estimated)	1.6mm
Preform clad/core ratio	7.5
Fibre clad diameter (required)	125μm
Fibre clad/core ratio	7.5
Fibre core diameter (expected)	16.6μm

The first preform was fabricated following the all vapour phase deposition technique, as described before, with sufficient temperature to sinter the particles after the deposition layer as shown in Image 4.

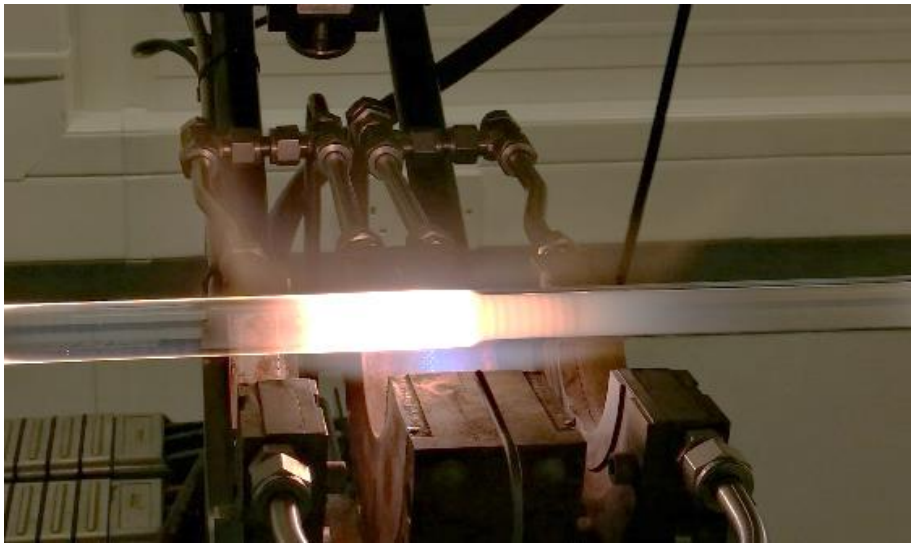

Image 4. Complete sintered layer during $SiCl_4$ and $AlCl_3$ deposition

The second preform followed a similar route but with an enhanced porosity layer. During the $AlCl_3$ deposition, the hot zone was reduced by using curtains and the temperature was reduced to the lowest possible level to be insufficient to consolidate the resultant particles (as shown in Image 5) but enough to oxidise the $SiCl_4$ and $AlCl_3$ chloride flow.

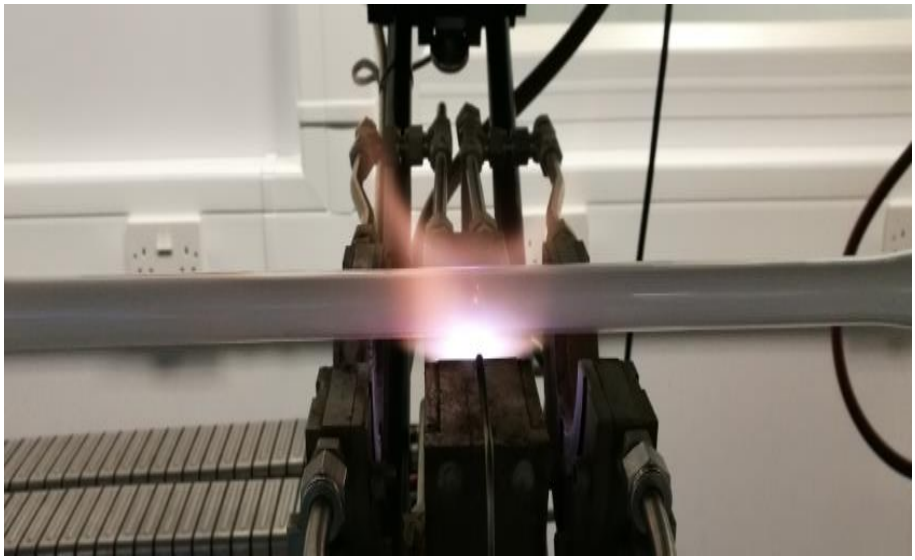

Image 5. Porous soot layer during $SiCl_4$ and $AlCl_3$ deposition

Subsequently, the tube was separated from the MCVD lathe and soaked in a pure methanol solution.

In order to verify the soot porosity and its adhesion to the inner glass surface, a set of experiments was carried out where a SiO_2/Al_2O_3 porous layer was grown in the inner wall of the substrate tube at different reaction temperatures. If the temperature was too high, the soot layer became partially sintered and built up a pore-free glass layer. If the temperature was too low, the soot layer did not adhere to the glass surface. Nevertheless, after the soot deposition, a low temperature "pre sintering" pass was applied to sufficiently adhere the soot layer to the glass surface. Image 6 shows the soot nature under different deposition temperature conditions when soaked in a MeOH solution.

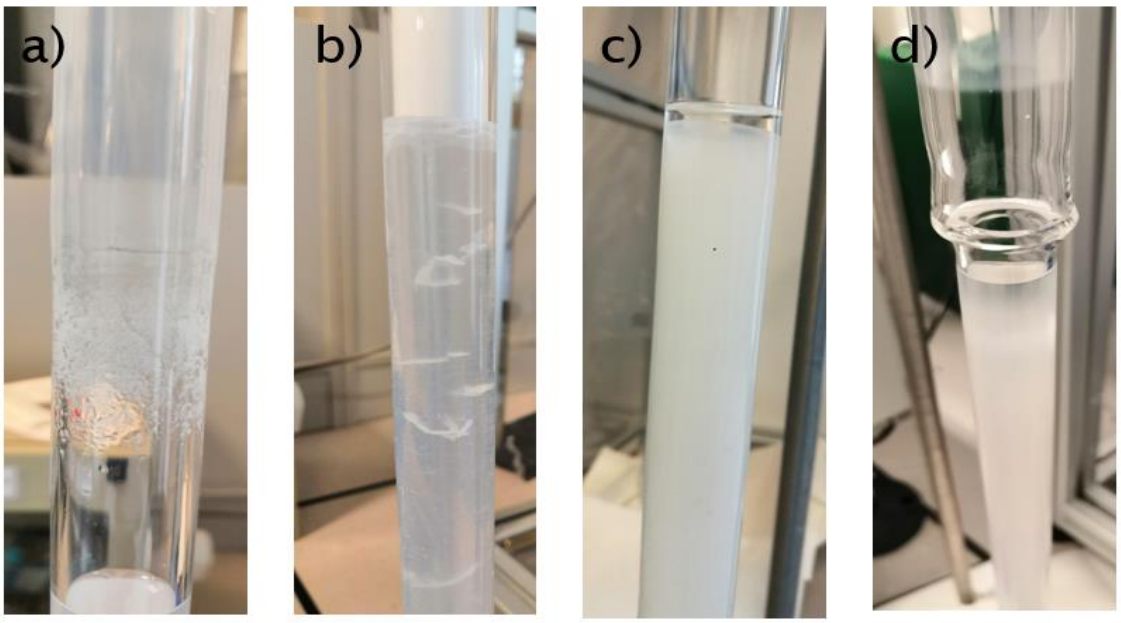

Image 6. Porous soot during methanol soaking.
a) Total deadhesion; b) Partial deadhesion; c) Partial consolidation; d) Minimum consolidation

After approximately one hour, the methanol was drained from the tube. Then, the tube with the impregnated porous soot layer was reinstalled on the MCVD lathe and dried with only oxygen and nitrogen. Finally, the substrate tube was collapsed and sealed in the usual manner. No additional dehydration step was added to the process since the intention was to compare both fabrication routes and exhibit the OH contribution with and without the methanol soaking step.

The refractive index profile analysis showed the characteristic flat-top profile with a core diameter of ~1.8mm. As presented in Graph 8, a small decreasing variation in the Δn can be seen from the beginning to the end of the preform. This fluctuation can be reduced by optimizing the porous soot layer during the deposition. However, it is necessary to clarify that the optimum soot deposition temperature will only exist for a specific set of process conditions.

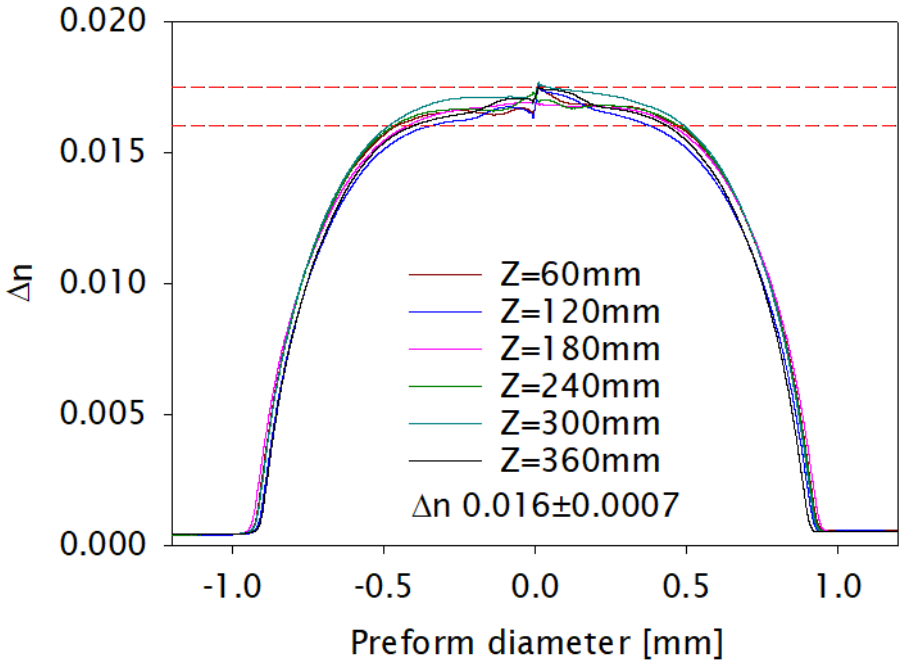

Graph 8. RIP stability along the length of the preform

Finally, a compositional analysis was performed using electron disperse X-ray spectroscopy. The analysis shows an Al_2O_3 doping concentration of ~9.35mol%, which matches with the 9mol% from our calculations. Graph 9 shows the overlap from the preform refractive index and the aluminium distribution within the core.

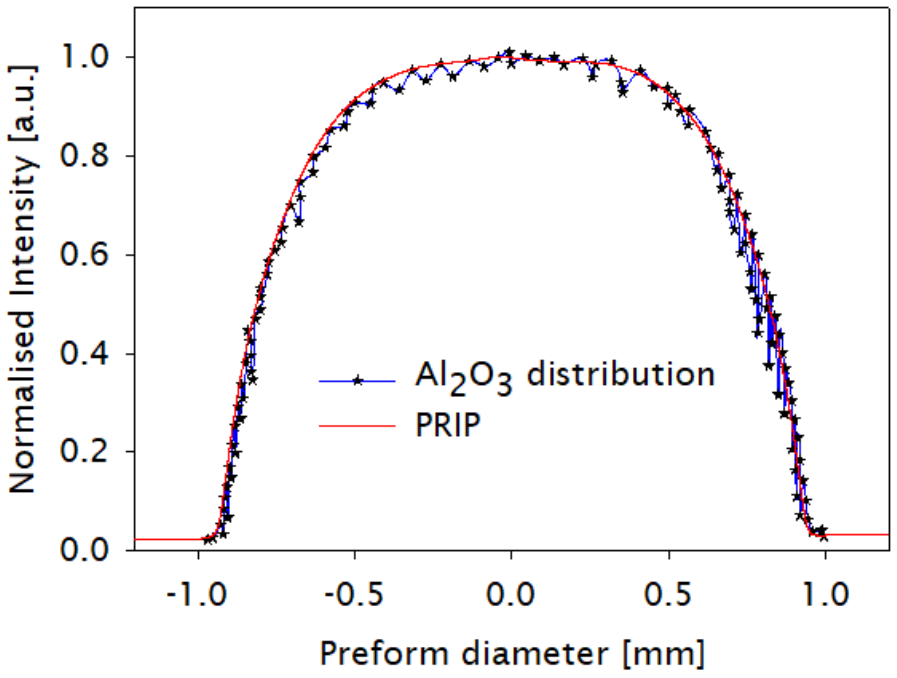

Graph 9. Al_2O_3 distribution overlapped with the preform RIP

3.2.4 Fibre characterisation

All preforms were drawn into 125µm diameter fibres and coated with a high index polymer to explore the impact of the vapour phase deposition technique in terms of background loss. As shown in Graph 10, there is a relatively low increment in the losses from 1100nm to 1700nm when the Al_2O_3 concentration is increased.

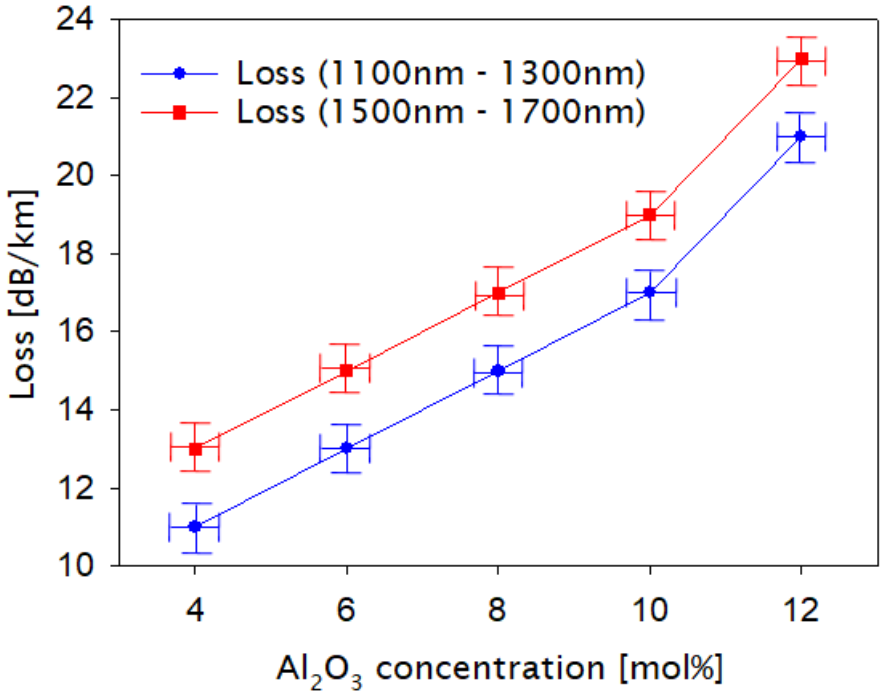

Graph 10. Al-doped fibre losses as function of dopant concentration

The background loss was also measured for the Al-doped fibre soaked with methanol to see the OH contamination. Graph 11 shows that there is an increment of ~30% in the losses between both fibres, which can be attributed to the lack of any additional dehydration process since the OH at 1380nm increased from 1ppm to 4ppm.

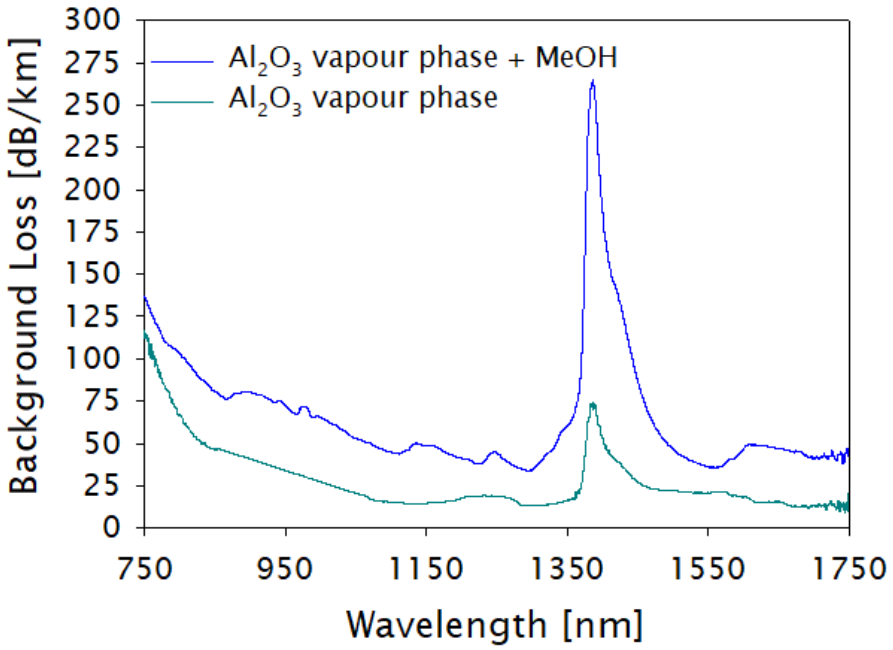

Graph 11. Al-doped fibres loss spectrum

A comparison of the measured properties of Al-doped preforms and fibres fabricated using the all vapour phase technique with and without methanol presence can be found in Table 4.

Table 4. Al-doped fabrication parameter and fibre characteristics

	Vapour phase	Vapour phase + MeOH
Number of soot layers	1	1
$SiCl_4$ gas flow	40sccm	40sccm
$AlCl_3$ gas flow	15sccm	15sccm
Soot characteristic	sintered	porous
Soaking time	N/A	60 min
Drying time	N/A	60 min
Preform core diameter	1.6±0.01	1.8±0.03
Preform Δn	0.016±0.0003	0.016±0.0007
Cladding diameter	125µm±0.2	125µm±0.3
Core diameter	16µm±0.2	18µm±0.3
OH @1380nm	~1ppm	~4ppm
Loss @1700nm	~15 dB/km	~40 dB/km

3.3 Summary

The standard technology to fabricate rare earth doped fibres is by MCVD in combination with solution doping, where aluminium and rare earth ion chlorides are dissolved in a solution and then incorporated to the silica matrix. However, when the rare earth concentration is increased, the aluminium chloride needs to be increased proportionally. When the aluminium concentration is >4mol%, unwanted effects such as changes of phase in the material and star diffusion within the core are presented.

To overcome this limitation, we have successfully demonstrated that the aluminium chloride can be incorporated with an all vapour phase deposition technique, achieving dopant concentrations >12mol% with no adverse effect within the core. Moreover, our results show no central dip as the volatility level in aluminium is much lower compared to other host, and a flat top refractive index profile close to a step index profile with a homogeneous distribution of the aluminium within the core.

The results above show that is it possible to fabricate high aluminium-doped preforms with an almost negligible refractive index variation along the length of the preform by using a vapour phase deposition system.

Chapter 4 Highly efficient thulium-doped high power laser fibres

4.1 Introduction

Thulium-doped fibres are commonly fabricated by a modified chemical vapour deposition technique in conjunction with the well-established solution doping method to introduce both Al_2O_3 and Tm_2O_3 into the fibre core. As mentioned in Chapter 3, the importance of aluminium as a network modifier is that it helps to prevent clustering. Hence, it allows the incorporation of higher levels of rare earths to the silica matrix.

Additionally, it is possible to exploit the two-for-one cross-relaxation process in thulium, generating two excited ions in the $^3F_4$ manifold for one pump photon when pumped by ~790nm high power laser diodes. This mechanism in thulium enables the possibility of reaching quantum efficiencies greater than 100% when the thulium concentration exceeds ~2wt%.

However, in order to increase the thulium concentration, the aluminium oxide concentration must be increased proportionally. As mentioned in Chapter 3, aluminium concentration over 4mol% are difficult to achieve using the conventional solution doping process. Thus, high thulium concentration in the fibre without an adequate level of aluminium oxide may cause adverse effects such as reduced lifetime and unwanted energy transfer upconversion processes.

The objective of this chapter is to present an alternative fabrication route for Tm-doped fibres and overcome the aforementioned limitations. It is possible to increase the aluminium oxide content in the core by using a vapour phase deposition technique. High-purity thulium halide precursors can be incorporated in the core by conventional solution doping within an optimized aluminosilicate glass host composition. With this approach, not only high dopant concentrations of Al_2O_3 and Tm_2O_3 can be reached, but also a more flat-top dopant distribution of both thulium and aluminium within the core over conventional MCVD-solution doping process.

4.2 Experimental work

4.2.1 Fabrication

Several Tm-doped fibers with thulium concentrations varying from 2wt% – 6wt% were fabricated. Nine preforms were fabricated by MCVD in combination with a hybrid gas phase-solution doping technique with different thulium and aluminium concentrations. An additional preform was fabricated with an optimized MCVD process and conventional solution doping technique, offering a maximum cross-relaxation process with this fabrication method.

4.2.1.1 General preform/fibre design

Due to the results obtained in Chapter 3, the aim for the thulium-doped preforms was to get an aluminium oxide concentration of around 7mol% (10.9wt%) to avoid instability along the length of the preform and variation in the deposition temperatures of the different thulium concentrations.

The calculated values for the preforms are presented in Table 5. For these calculations, the molar mass of Al_2O_3 and Tm_2O_3 was 101.96g/mol and 385.87g/mol, respectively. The estimated concentration is given in wt% as it is more appreciated in the literature when talking about the two-for-one cross relaxation in thulium doped fibres.

Table 5. Estimated preform design Δn

Preform	Estimated Conc. [wt%%] $SiO_2/Al_2O_3/Tm_2O_3$	Calculated Conc. [mol%] Al_2O_3/Tm_2O_3	Calculated Δn Al_2O_3/Tm_2O_3	Total Δn
HGSD-01	85/10.9/4	6.98/0.67	0.015/0.0045	0.019
HGSD-02	83/10.9/6	7.11/1.03	0.015/0.0069	0.022
HGSD-03	83.6/10.9/5.5	7.08/0.94	0.015/0.0063	0.021
HGSD-04	85/10.9/4	6.98/0.67	0.015/0.0045	0.019
HGSD-05	85.6/10.9/3.5	6.96/0.58	0.015/0.0039	0.019
HGSD-06	86/10.9/3	6.92/0.5	0.015/0.0033	0.018
HGSD-07	87/10.9/2	6.85/0.33	0.015/0.0022	0.017
HGSD-08	88/10.9/1	6.79/0.16	0.015/0.0011	0.016
HGSD-09	88.6/10.9/0.5	6.76/0.08	0.015/0.00054	0.015

The preforms were fabricated in a 20x16mm silica substrate tube and the idea was to expose the fabricated fibres to high power levels (>40W), therefore the cladding/core ratio needed to be changed for heat management purposes. The fibres were expected to be drawn with 200μm cladding and 8μm core.

As the Al-doped preform reported in Chapter 3 had a cladding diameter of ~12mm and 1.8mm core diameter, the cladding/core ratio is around 7. In order to obtain a ratio of 25, a series of post processing stages such as stretching and sleeving of the preform was performed. It is possible to use the single aluminium-doped preform as a reference due to the fact that the thickness of the layer will be only influenced by the amount of silica deposited, the dopant concentration through solution and the temperature used during the fabrication process.

4.2.1.2 Preform fabrication using MCVD and Solution doping

The preform was fabricated in an MCVD apparatus using a Suprasil F300 silica substrate tube from Heraeus with a nominal OD/ID of 20/16mm and 350mm length. As the tube becomes the outer cladding of the resultant fibre, it is important to be sure that any existence of intrinsic bubbles or other defects are removed from the inner wall of the tube as they can affect the attenuation and strength of the final optical fibre. Therefore, the tube was cleaned before use with an SF_6 flow to remove any contaminants that could lead to bubbles or impurity defects. In a similar way, in order to remove any surface irregularities and shrink any tubing bubbles, the tube was exposed to a fire polish process at high temperatures ~2000°C. Image 7 shows a silica substrate tube with an SF_6 flow for etching/cleaning purposes prior to the silica cladding deposition.

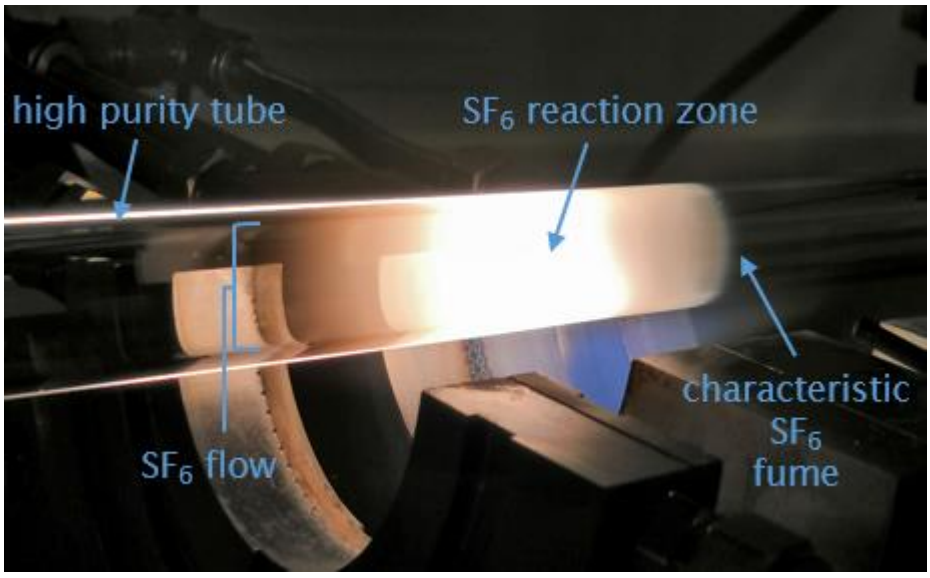

Image 7. SF_6 cleaning

Before the core host deposition, a few additional cladding layers of SiO_2 were deposited inside the tube followed by a porous soot layer of ~80sccm of $SiCl_4$ at an optimized temperature. Then, the preform was removed from the MCVD lathe and

soaked in a methanol solution with the required concentration of aluminium chloride ($AlCl_3.xH_2O$, 99.9999%) and thulium chloride ($TmCl_3.xH_2O$, 99.9999%) for approximately one hour.

Subsequent to the solution doping stage, the preforms were reassembled on the MCVD lathe and dehydrated in the presence of N_2 to eliminate any trace of solvents. Then, the dried porous layer was heated up in the presence of oxygen to convert the thulium and aluminium chlorides into their corresponding oxide. Finally, the porous core layer was sintered, collapsed and sealed in the usual manner.

4.2.1.3 Preform fabrication using HGSD technique

All thulium-doped preform fabrications conducted with the hybrid gas phase-solution doping technique were carried out in a Suprasil F300 silica substrate tube from Heraeus with a nominal OD/ID of 20/16mm and 350mm length.

As described in Chapter 3, layers of SiO_2 were deposited inside the tube to build up a fully sintered transparent layer as cladding. Next, an aluminosilicate soot layer was introduced by mixing $SiCl_4$ and $AlCl_3$ with oxygen at an elevated temperature. The $AlCl_3$ evaporator mass flow was set in the range of 30 – 60mg/min and helium was used as a carrier gas to transport the $AlCl_3$ to the deposition zone through a separate heated delivery line that was maintained at about ~200˚C.

Graph 12 shows the temperature set for the porous soot layer and the real temperature taken from the pyrometer of the MCVD lathe during the approximately 4 minutes of the deposition. Graph 12 also shows a clear variation of 30°C during this stage of the process, which directly influences the incorporation of dopants. Depending on the aluminium concentration in the gas mixture, the soot deposition temperature was manually adjusted to maintain an adequate porosity of the soot body and allow a uniform incorporation of thulium ions during the solution doping stage.

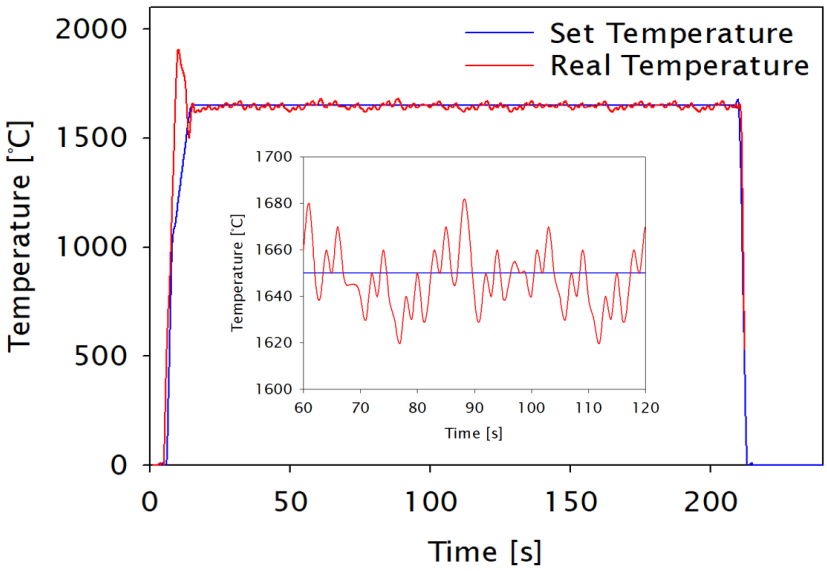

Graph 12. Porous soot deposition temperature

Subsequently, the preform was removed from the MCVD lathe and soaked for a period of one hour in a solution of methanol containing thulium chloride ($TmCl_3.xH_2O$, 99.9999%). Then, the solution was drained and the preform was reinstalled in the MCVD lathe to be dried with an oxygen and nitrogen flow.

During the dehydration stage, cracking and peeling of the porous soot layer due to the viscosity of the solution (depending on the thulium concentration) was noticed. As shown in Image 8, with relatively low thulium concentration, the soot seems homogeneous and smooth.

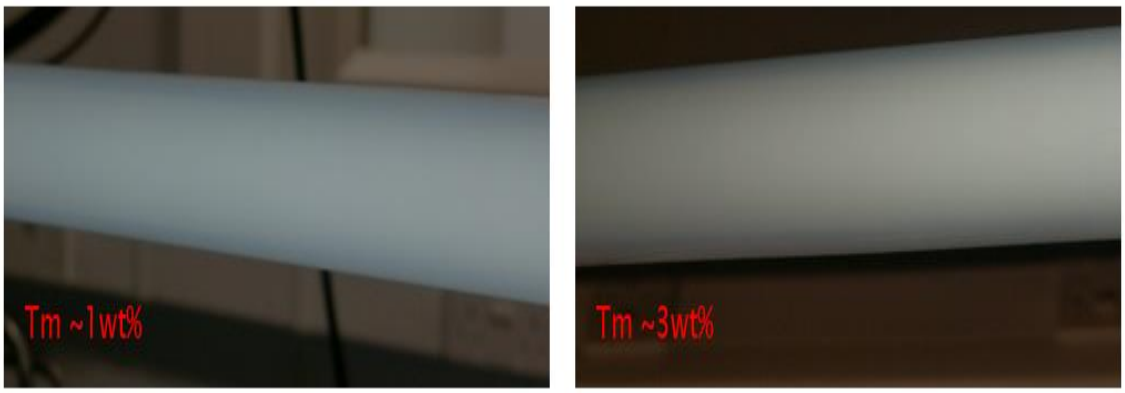

Image 8. Porous soot with a low Tm^{3+} doping concentration

On the other hand, when the thulium concentration was increased in the solution, the soot appeared to be cracked or peeled off from the substrate tube as shown in Image 9.

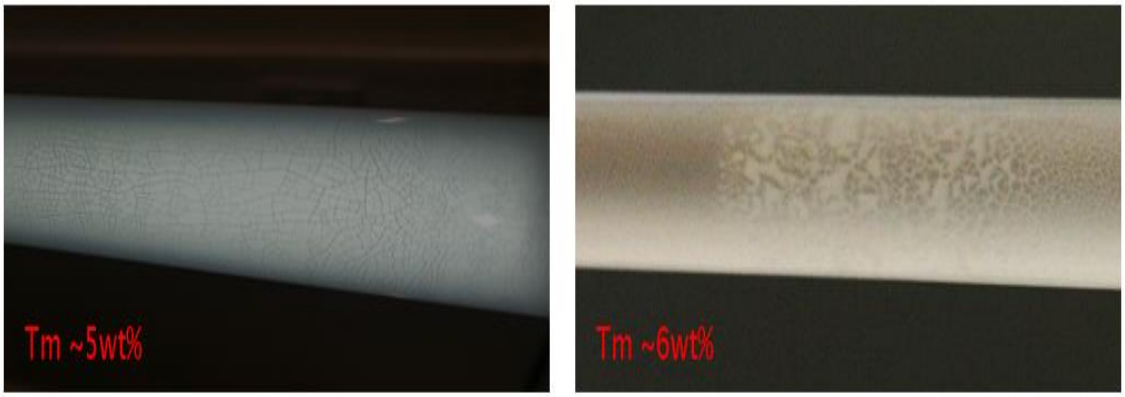

Image 9. Porous soot with a high Tm^{3+} doping concentration

This can be reduced by optimizing the temperature during the soot deposition or by changing the duration of the solution doping stage. However, it is worth remembering that the optimum conditions for the adhesion to the substrate tube and the optimum density for avoiding any cracking or peeling of the porous soot will only exist for a specific set of process conditions.

Finally, the substrate tubes were reassembled on the MCVD lathe for oxidation and sintering of the core layer. The tubes were then collapsed into a solid rod in the usual manner.

4.2.1.4 Cladding modifications

The preforms fabricated using the two different routes were post-processed to modify their core to cladding ratio by inserting the preforms inside a tube made of the same glass.

As the main complication of this process is the limited availability of the tube size, a high quality substrate tube was collapsed by an oxygen/hydrogen burner traversing the tube, the temperature was increased and the burner velocity was decreased. Hence, the viscosity of the cross sectional area of the tube was varied according to the controlled combination of both parameters, modifying the wall thickness and changing the outer and inner diameter of the tube proportionally.

The post process preform design stages are summarized in Table 6. It is important to mention that the following steps were used as reference (±3mm). For each post processed preform, the conditions and the size of the tubes varied due to the different preform characteristics such as core size, cladding size and availability of the preform.

Table 6. Post-processed preform design

Sleeving 1	
Initial preform diameter	~12mm
Sleeving tube size 1 (start)	25mmx19mm
Sleeving tube size 1 (end)	22mmx14mm
Core size 1	~1.9mm
*Core size if drawn to 200μm	~17μm
Stretching 1	
Initial preform diameter	~20mm
Core size 1	~1.9mm
New core size	~0.6mm
New preform diameter	~8mm
Sleeving 2	
Initial preform diameter	~10mm
Sleeving tube size 2 (start)	20mmx16mm
Sleeving tube size 2 (end)	16mmx10mm
Core size 2	~0.6mm
*Core size if drawn to 200μm	~8μm

For the sleeving process, the original Tm-doped preform was introduced into the collapsed tube and fixed inside tube with a suitable inner pressure to minimize the bubbles in the interface as shown in Image 10.

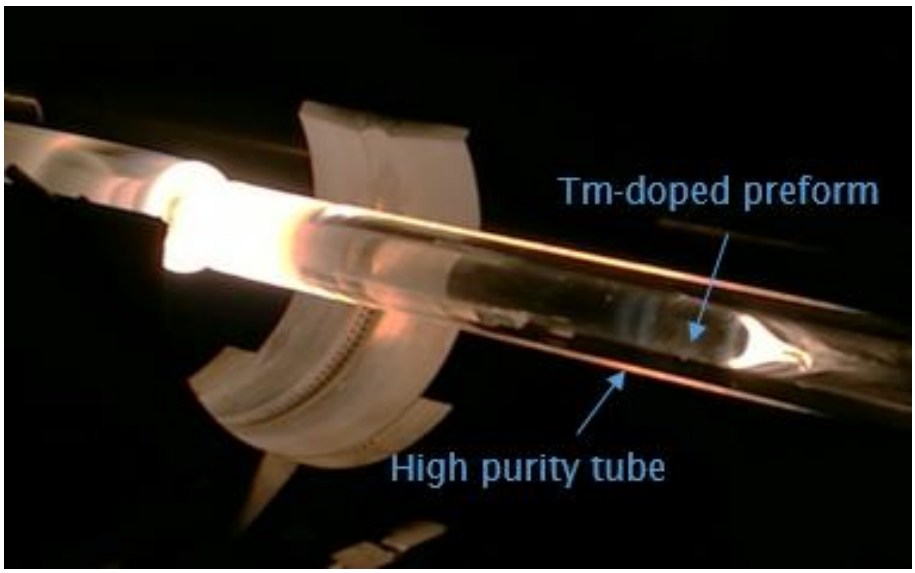

Image 10. Core / Clad ratio modification: preform sleeving

Subsequently, the temperature was increased again and the burner velocity was adjusted until the glass fused and turned into a solid rod. This process was repeated until the desired cladding/core ratio was reached. Image 11 shows the final preform with a modified core to clad ratio.

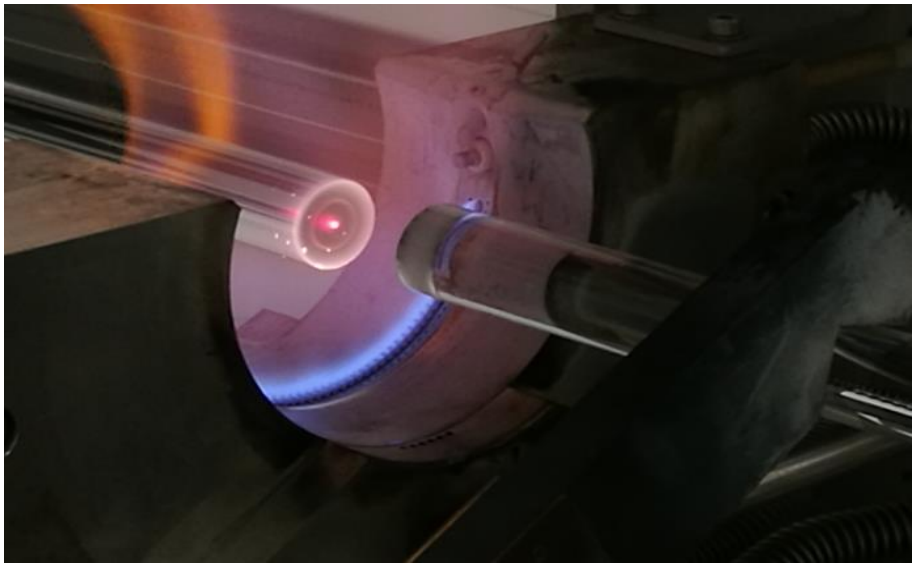

Image 11. Preform with modified core to cladding ratio

As explained in Chapter 2, it is possible that, due to the circular cladding of the preforms, the optical rays that propagate through the optical fibre do not pass through its axis, limiting the core absorption of the pump light. Therefore, it is necessary to break the circular symmetry of the fibre structure by reshaping the cladding to ensure an efficient pump absorption.

All the preforms presented in this thesis were modified by using an ultrasonic milling process as shown in Image 12, where a tool bit vibrates at an ultrasonic frequency and gradually removes glass material from the preform. It is possible that the surface of the preform acquires some degree of roughness due to the material removal which can lead to scattering losses during the fibre performance. However, this can be minimized if the speed of the tool bit is reduced.

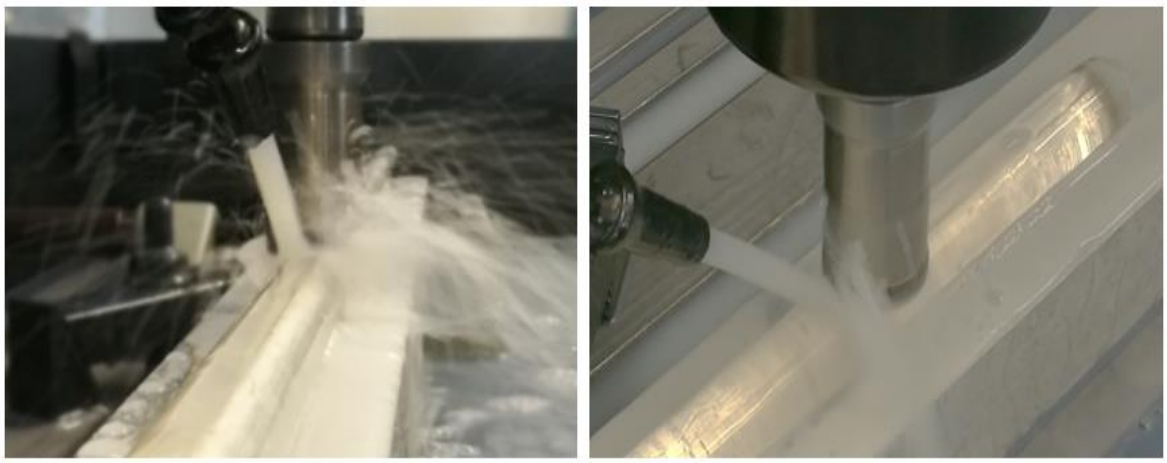

Image 12. Ultrasonic milling process

The preform with a remove section of the cladding surface is shown in Image 13.

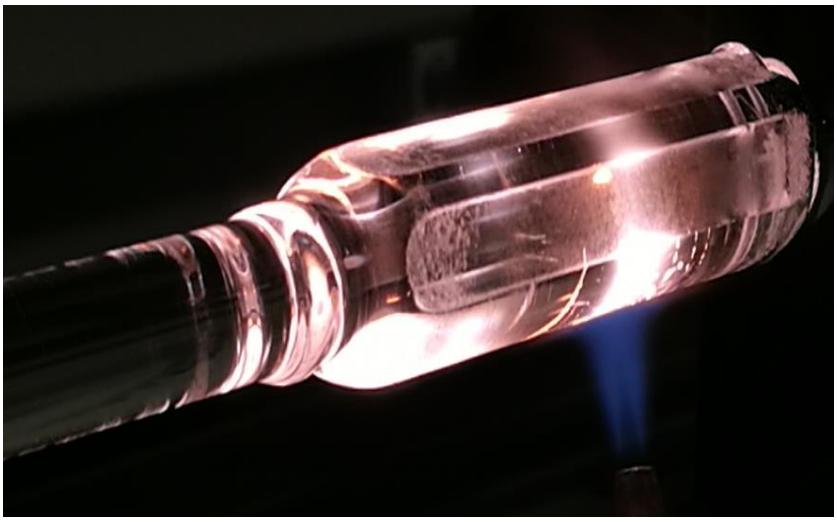

Image 13. Final preform after milling

Finally, the preforms were drawn into 200μm diameter fibres and coated with a low index polymer. Image 14 shows a cross sectional view of the final fibre with the clad/core of 200μm/8μm and the modified geometry. It also shows the two sleeving procedures that were done to the preforms.

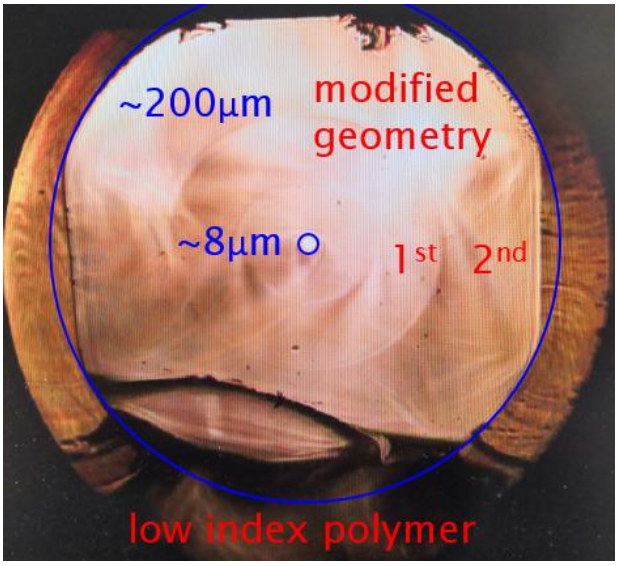

Image 14. Final fibre cross sectional view

4.2.2 Characterisation

The resultant fibers were characterized by an IFA-100 for the refractive index profile and by Electron Disperse X-Ray Spectroscopy in collaboration with Dr. Miguel Nunez-Velazquez to identify the core composition and dopant distribution. Additionally, cladding and core absorption measurements were carried out using a white light source and an optical spectrum analyser. As mentioned in Chapter 2, a combination of modified geometry and coiling shapes were applied to the fibres. Figure 21 and Graph 13 show the configuration used for the measurement of the absorption and the increase on the ~790nm absorption wavelength when the fibre was exposed to different coiling shapes and forced mode mixing, respectively.

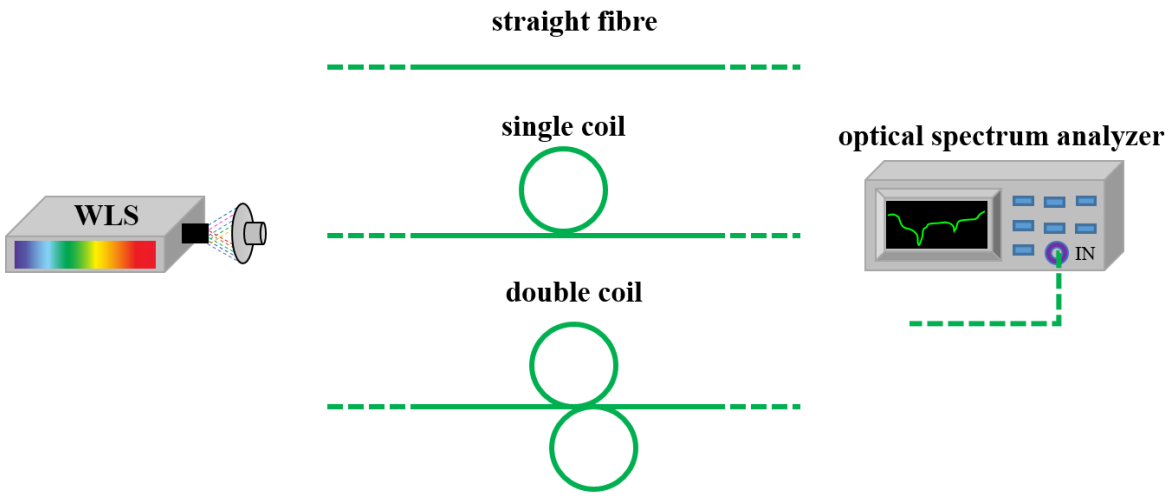

Figure 21. Absorption measurement configurations

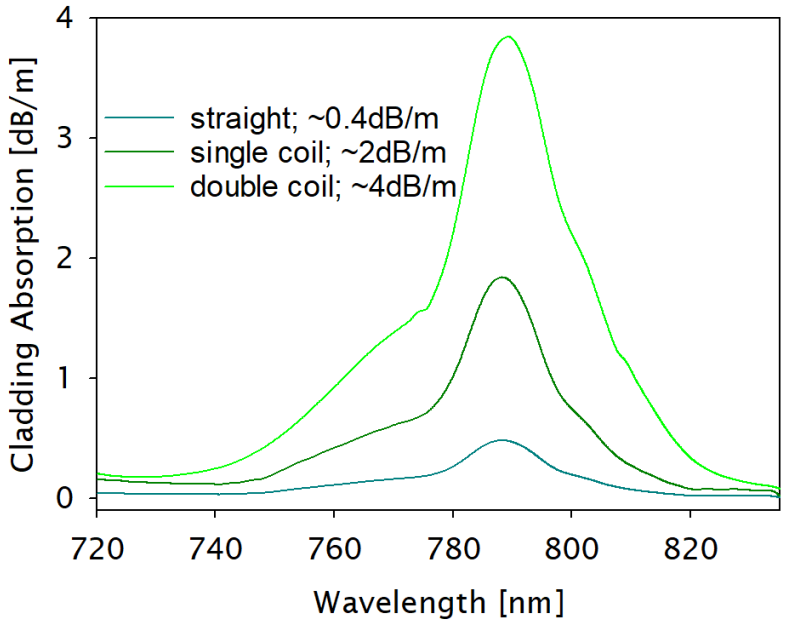

Graph 13. Enhanced mode mixing by coiling methods

The cladding absorption was taken directly from the absorption spectrum as all fibres were coated with a low index polymer that allowed the transmission of the light through the cladding. The core absorption was calculated using Equation 8. It is possible to approximate the dopant concentration of the fibre in parts per million by using an absorption coefficient previously characterised for a specific absorption band of the rare earth.

$$Core\ Abs = Clad\ Abs * \left[\frac{cladding}{core}\right]^2$$

Equation 8. Core absorption

The cladding absorption spectrum of the fibres is shown in Graph 14.

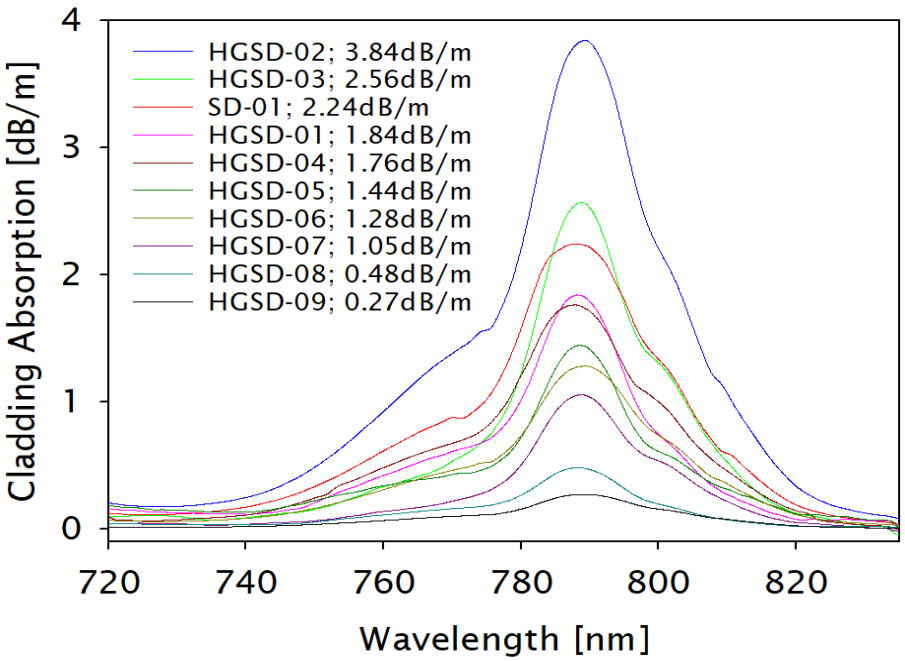

Graph 14. Thulium-doped fibre cladding absorption spectrum

The characteristics of the thulium-doped fibres are shown in Table 7.

Table 7. Thulium-doped fibre characteristics

Fibre	Clad/Core [µm]	NA	Core abs at 790nm [dB/m]	Tm_2O_3 [wt%]	Al_2O_3 [wt%]
SD-01	200/8	0.20	1400	5.1	6.8
HGSD-01	200/8	0.23	1150	4.3	10.6
HGSD-02	200/8	0.30	2400	7.0	15.0
HGSD-03	200/8	0.27	1600	6.4	11.6
HGSD-04	200/8	0.22	1100	4.0	9.3
HGSD-05	200/8	0.23	900	3.4	14.8
HGSD-06	200/8	0.22	800	2.8	9.6
HGSD-07	200/8	0.24	660	2.3	13.6
HGSD-08	200/8	0.19	300	1.0	9.8
HGSD-09	200/8	0.19	170	0.6	9.7

For the purposes of this thesis, the fibres HGSD-08 and HGSD-09 were not further tested due to their low thulium concentrations <2wt% and because we did not expect any two-for-one cross-relaxation.

4.2.2.1 HGSD vs SD

The dopant distribution of HGSD-01 and SD-01 fibers is compared. The core composition was 10.6wt% of Al_2O_3 and 4.3wt% of Tm_2O_3 for HGSD-01 and 6.8wt% of Al_2O_3 and 5.1wt% of Tm_2O_3 for SD-01. The results show that with the hybrid gas phase solution doping technique, the aluminium incorporation in the core can be significantly increased. The normalized thulium distribution in the core region overlapped with the fibre refractive index is shown in Graph 15.

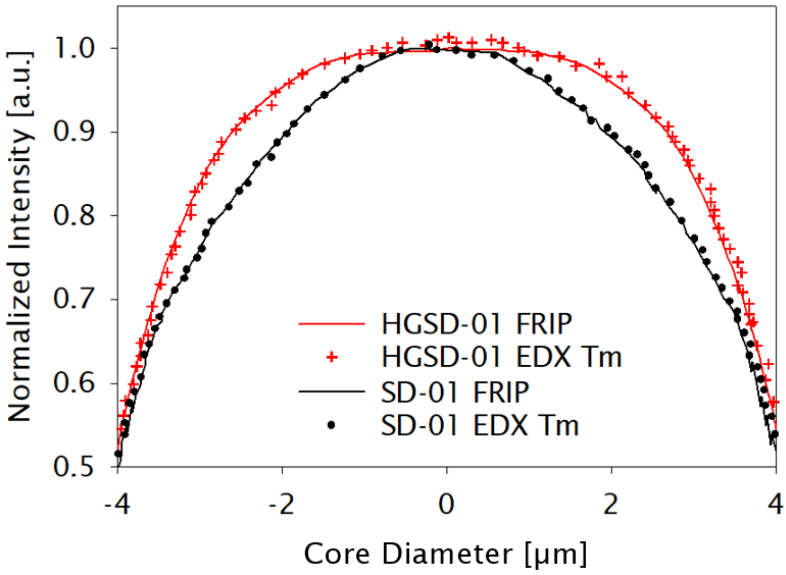

Graph 15. Thulium distribution overlapped with fibre refractive index profile

The thulium and aluminium dopants distribution follow the refractive index profile in both fibers. However, in the fibre HGSD-01, a flat-top dopant profile has been achieved, which will ensure more thulium doped regions take part in the cross-relaxation process.

4.2.2.1.1 Preform stability

The refractive index profile from each preform was analysed with a PK2600 to explore the impact of the hybrid technique in terms of fabrication stability along the length of the preform as presented in Graph 16 and Graph 17.

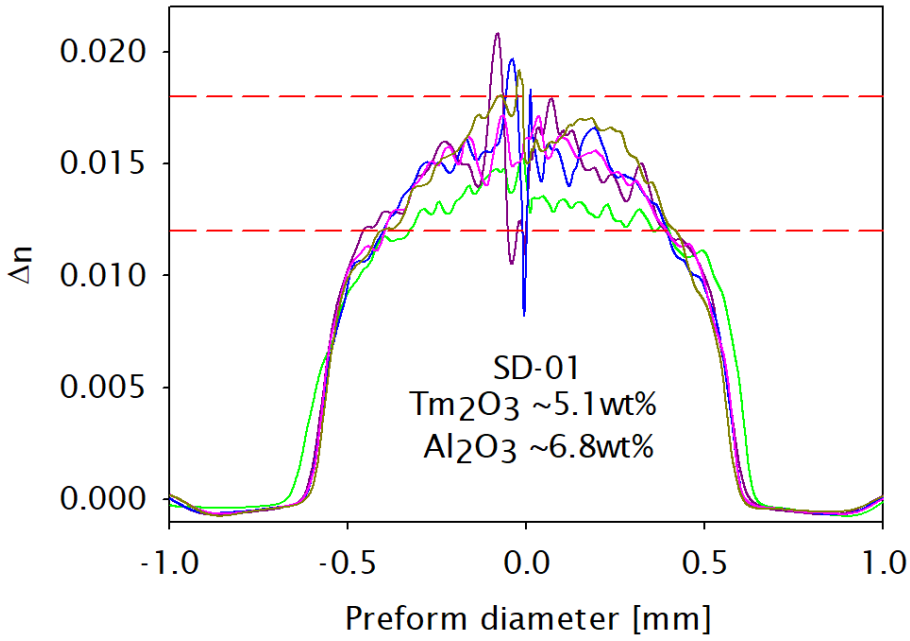

Graph 16. SD-01 preform refractive index profile (Solution Doping)

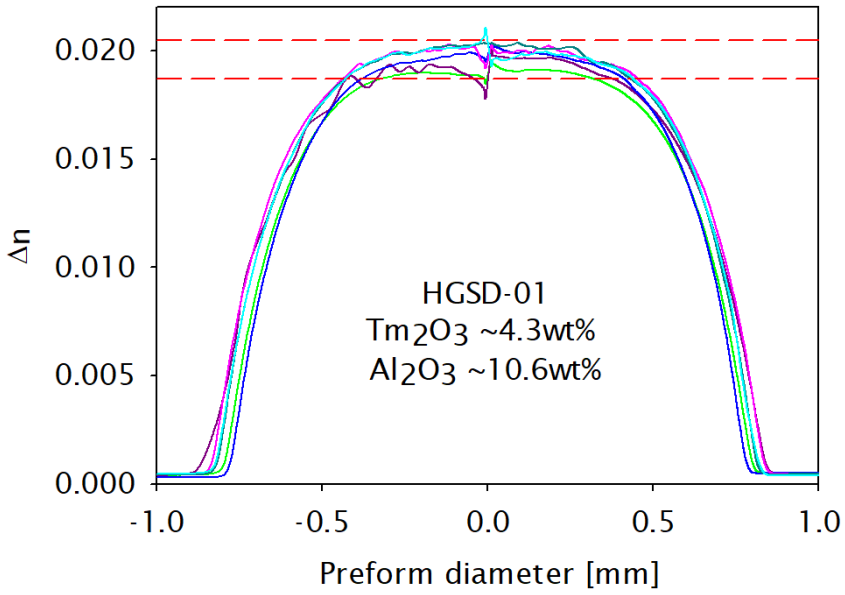

Graph 17. HGSD-01 preform refractive index profile (Hybrid technique)

Graph 18 shows the variation along the length of both preforms where the position at 60mm is the starting point of the deposition and soaking. It can be seen that conventional solution doping faces the characteristic Δn reduction. The non-uniformity along the length of the preform can be attributed to soot composition, the deposition temperature of SiO_2 and to the nature of the soaking method. On the contrary, the hybrid gas phase solution doping technique exhibits a more stable Δn variation due to the SiO_2/Al_2O_3 soot (all in one) composition, high aluminium concentration and the uniform distribution of the dopants due to the vapour phase deposition, allowing a direct increase in the thulium concentration and therefore, reducing the Δn dropping.

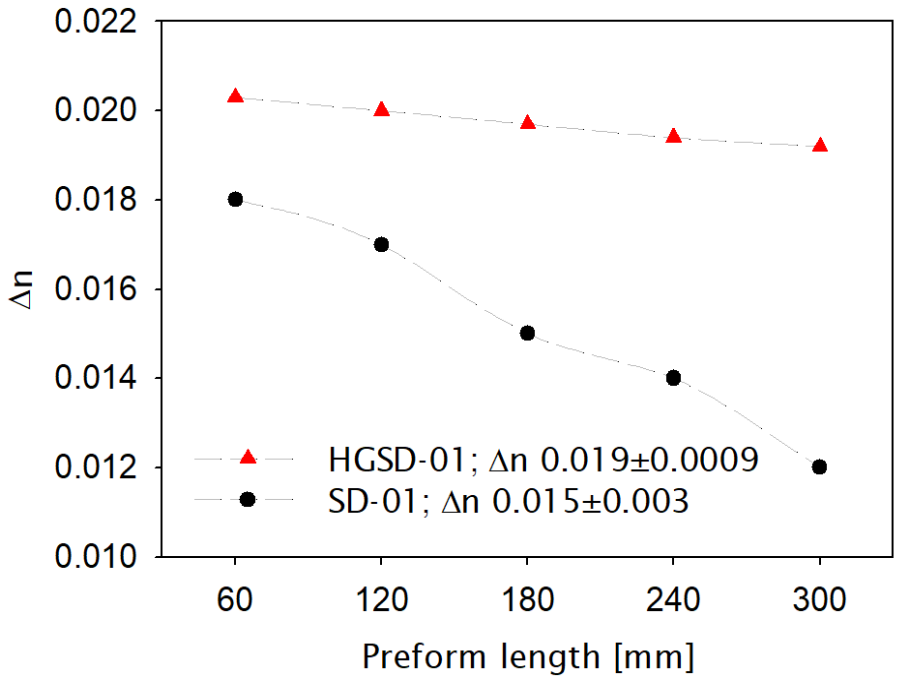

Graph 18. Longitudinal uniformity of Δn of HGSD-01 and SD-01 preforms

4.2.2.1.2 Lifetime measurements

The fluorescence lifetime of $^3F_4$ energy level manifold in thulium was measured with a 790nm diode modulated by a frequency generator with a modulation frequency of 10Hz and 10% duty cycle to produce pulsed pump light. An InGaAs photo-detector was placed close to an uncoated section of the fibre and transverse to the fibre under test to avoid any reabsorption or amplified spontaneous emission signals coming from the core to capture the 2μm fluorescence. The fibre under test was spliced directly to a passive fibre coming from the 790nm diode and mounted between two metallic base structures to keep the fibre straight during the measurement. Finally, the fluorescence decay from the excited level was recorded on an oscilloscope. The lifetime experimental set-up is shown in Figure 22.

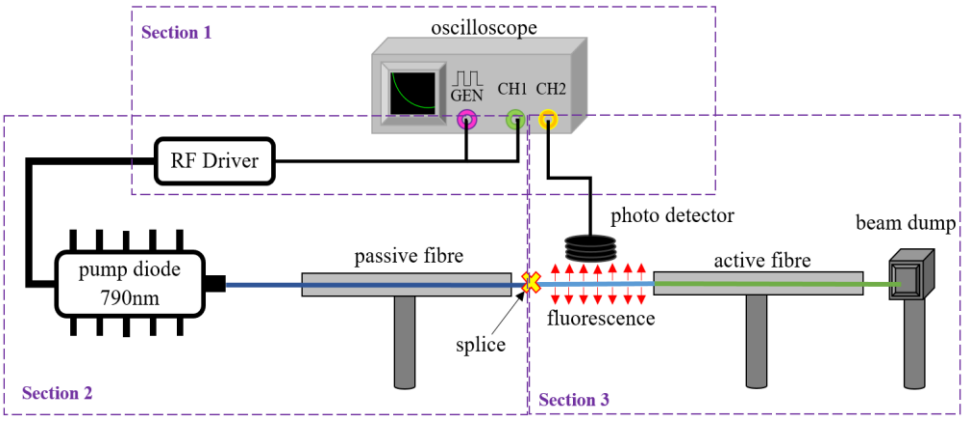

Figure 22. Schematic diagram for lifetime measurements

Even though all lifetime measurements were done under same conditions, a 2% error in the measurements was observed and attributed to the splices between the passive and active fibres. The experimental results were processed and fitted into a stretched exponential decay mathematical model expressed by Equation 9.

$$a * e^{(-(b*x)^p)} + c$$

Equation 9. Stretch exponential decay

The fluorescence lifetime decays of the thulium-doped fibres investigated in this section are shown in Graph 19.

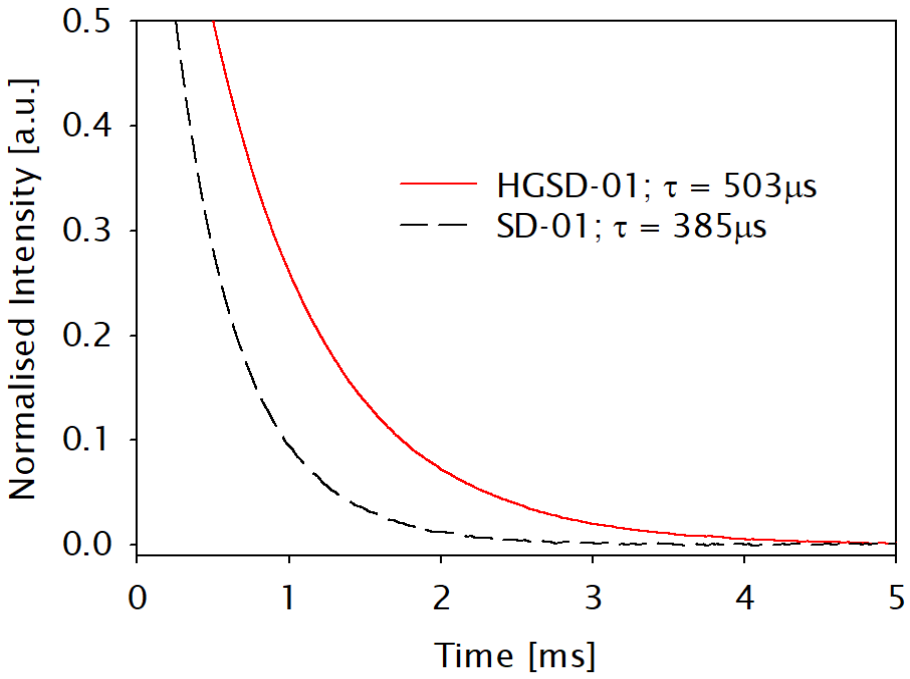

Graph 19. Fluorescence lifetime decays of HGSD-01 and SD-01 fibres

Owing to the high aluminium concentration and better distribution within the core, the fibre fabricated by the hybrid gas phase-solution doping technique has shown

a noticeable enhancement in the fluorescence lifetime compared to those fabricated using the conventional solution doping process from 385μs to 503μs.

4.2.2.1.3 Laser efficiency

The laser performance of both thulium-doped fibers was measured in a 4% – 4% laser cavity configuration. The fibers were placed on a water-cooled base and cladding pumped by a ~790nm fibre coupled multimode laser diode through a combination of collimating lenses (L1, L2). The pump launch efficiency in the fibres was estimated at ~90%. Dichroic mirrors (DM1, DM2) were used to separate the pump from signal wavelengths at both pump launch and pump throughput ends of the fibre as shown in Figure 23. *See Appendix B for the experimental set-up evolution.

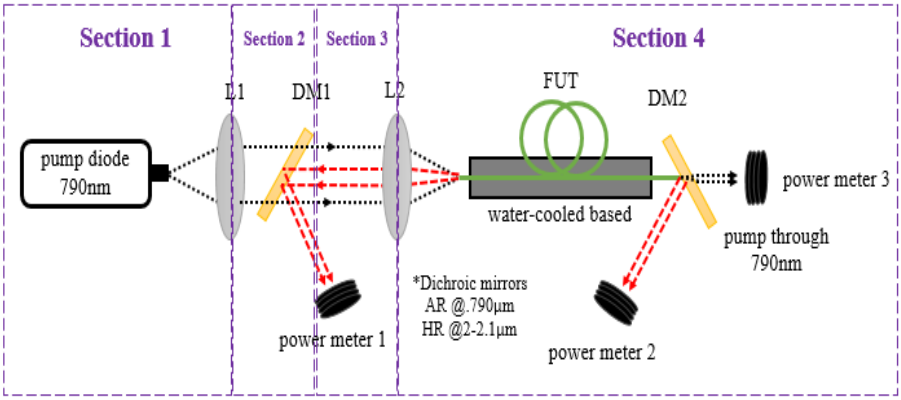

Figure 23. Schematic diagram of the experimental set-up

The slope efficiency was calculated with the total output power from both ends of the fibre. The fibre length was adjusted to obtain the maximum output power in a free-running laser cavity, which was 10m and 12m for HGSD-01 and SD-01 respectively. A monochromator was used to measure the 2μm emission band at its maximum output power, lasing around 2020±3nm.

The slope efficiency with respect to the absorbed pump power and the lasing threshold (Inset) of both fibres is shown in Graph 20.

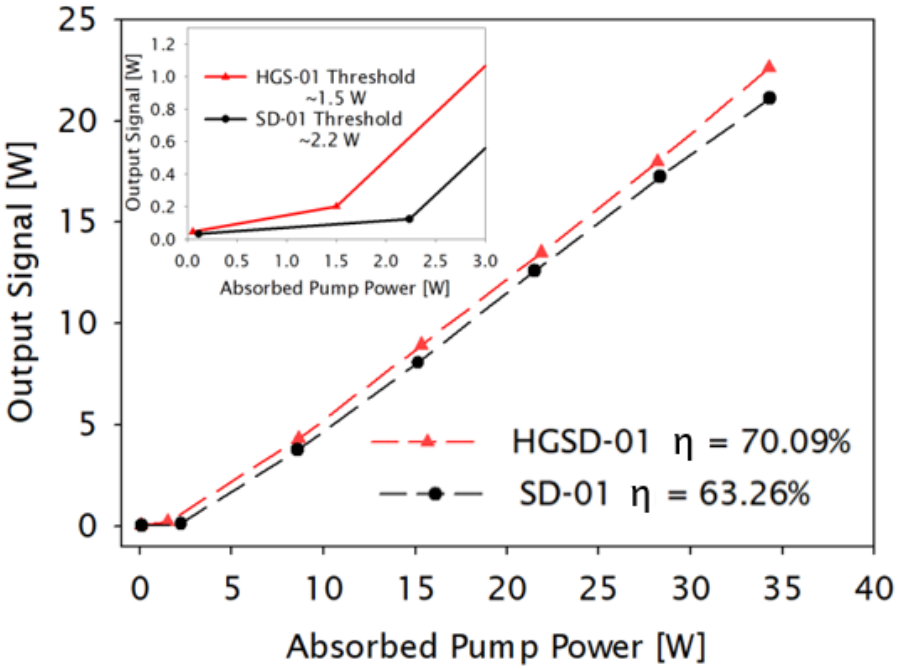

Graph 20. Laser characteristics of HGSD-01 and SD-01 fibres

The fibre HGSD-01 fabricated by the hybrid gas phase solution doping technique shows an improved two-for-one cross-relaxation process compared with the fibre fabricated by conventional solution doping due to a more uniform thulium doped profile in the core.

4.2.2.2 Evaluation of HGSD technique

4.2.2.2.1 Preform stability

As mentioned before, as the thulium concentration was increased in the solution, the soot appeared to be cracked or peeled off from the substrate tube. These irregularities were more visible during the sintering stage as shown in Image 15, making that section unusable. Nevertheless, more than 100mm comply with the Δn difference of ±0.002, similar to the Al-doped preforms presented in Chapter 3.

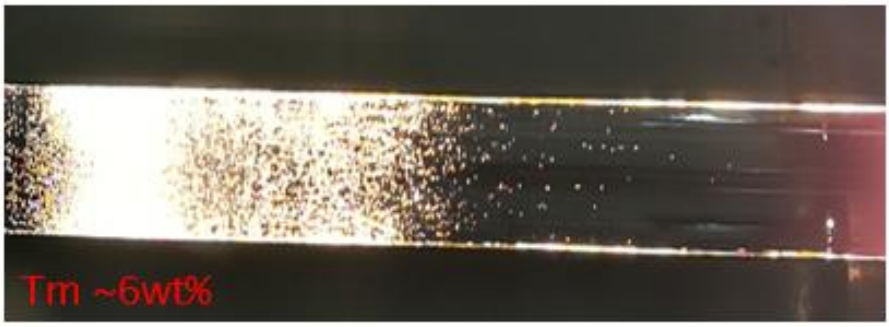

Image 15. HGSD-02 preform after sintering (Tm ~6wt%)

Regardless of the aluminium concentration, the Tm-doped preforms with thulium concentration <4wt% exhibit a refractive index profile variation almost negligible with a maximum difference of ±0.0009. However, when thulium concentrations exceed ~5wt%, the Δn variation becomes more unstable as shown in Graph 21.

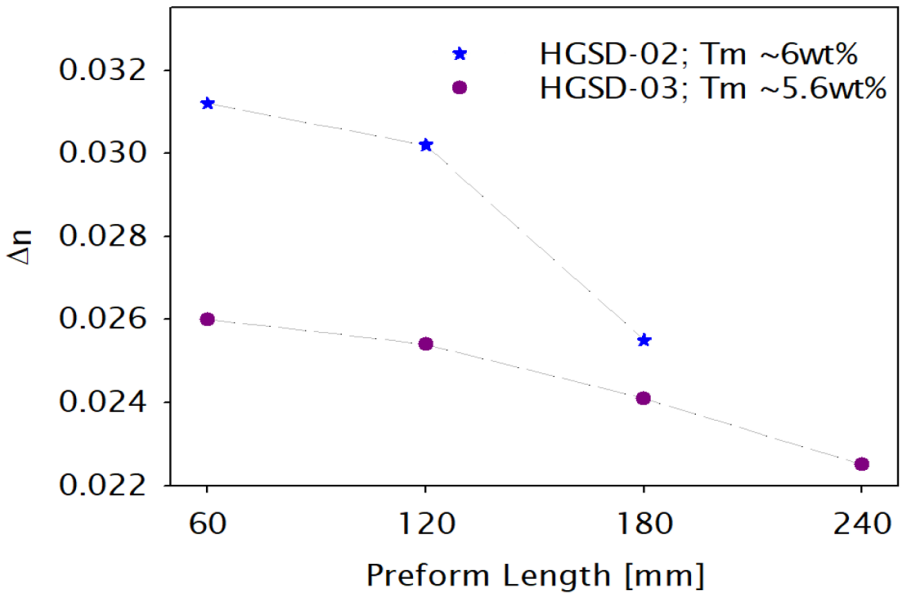

Graph 21. Longitudinal uniformity of Δn of HGSD-02 and HGSD-03 preforms

4.2.2.2.2 Fluorescence lifetime

The fluorescence lifetime values of the thulium-doped fibres fabricated by the hybrid gas phase solution doping technique against the Al_2O_3/Tm_2O_3 concentration ratio are presented in Graph 22.

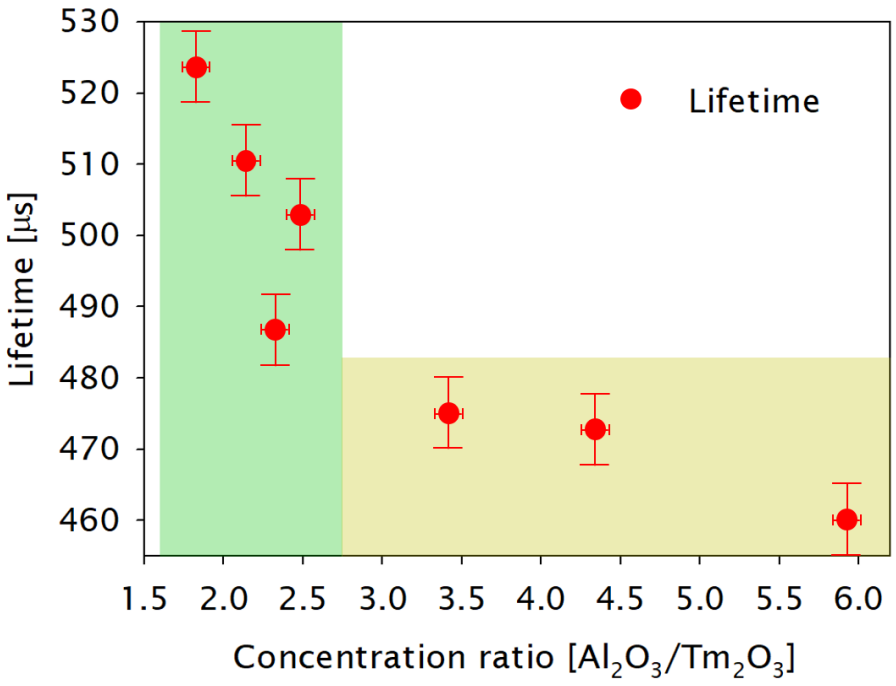

Graph 22. HGSD lifetime values

The different lifetime values are directly related to the amount of dopants contained in the core, however, the lifetime cannot be explained independently. According to our results, the highest lifetime values were obtained with an Al_2O_3/Tm_2O_3 concentration ratio of ~2:1. It is observed that when the concentration ratio is above ~3:1, the lifetime tends to decrease. This trend is shown with the reference lines in Graph 22, going from the ~500μs region (2:1) to the 470μs region (>3:1).

Comparing HGSD-06 and HGSD-07, both fibres contain a Tm_2O_3 concentration of ~2wt% but the Al_2O_3 content is higher for HGSD-07. The aluminium helps to reduce quenching, however, the enhanced dispersion of the dopants might produce a large separation between ions, thereby reducing the interaction between them and causing a continuous reduction of the lifetime.

4.2.2.2.3 Laser efficiency

The length of the Tm-doped fibres was adjusted in a free-running laser configuration to obtain a maximum laser efficiency. The results are summarized in Table 8.

Table 8. Performance of thulium-doped fibres fabricated using hybrid process

Fibre	Tm [wt%]	Al [wt%]	Length [m]	Emission [nm]	Pump Power [W]	η [%]	Output Power [W]
HGSD-01	3.8	5.6	11	2025	31.8±0.3	71.1	22.6±0.2
HGSD-02	6.1	7.9	7	2045	31.7±0.3	69.5	22.0±0.1
HGSD-03	5.6	6.1	8	2036	33.7±0.4	72.4	24.4±0.3
HGSD-04	3.5	4.9	12	2022	29.8±0.4	70.1	20.9±0.3
HGSD-05	3.0	7.8	9	2013	27.7±0.4	62.5	17.3±0.2
HGSD-06	2.5	5.1	10	2009	26.1±0.3	60.4	15.8±0.2
HGSD-07	2.0	7.2	12	2004	26.0±0.3	58.5	15.2±0.3

An increase in thulium concentration from ~2wt% to ~6wt% resulted in an improvement in the laser efficiency by ~18.5%. Fibres HGSD-01, HGSD-03 and HGSD-04 shows a slope efficiency of >70% as presented in Graph 23. Based on the results, a thulium concentration of ~3.5wt% is enough to maintain a good TDFL efficiency in the two-micron wavelength band when the diode is pumped at ~790nm.

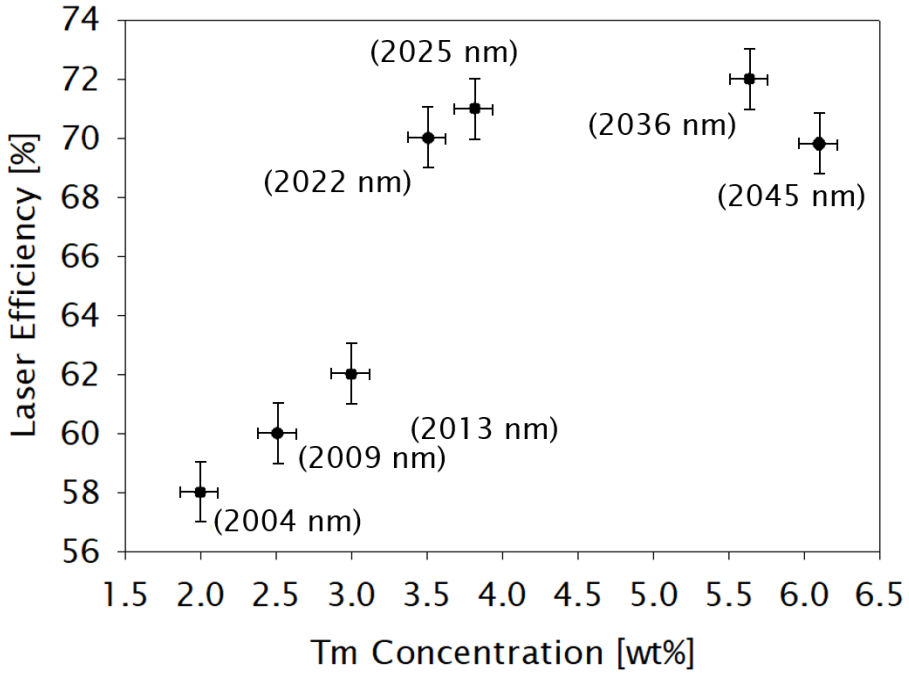

Graph 23. Laser efficiency and the corresponding laser emission wavelength as function of the thulium concentration

Furthermore, the Tm-doped fibres containing thulium concentrations of ~2wt%, ~3wt%, ~3.8wt% and ~5.6wt% were tested under a higher pump power 790nm diode maintaining the laser efficiency as shown in Graph 24, Graph 25, Graph 26 and Graph 27, respectively.

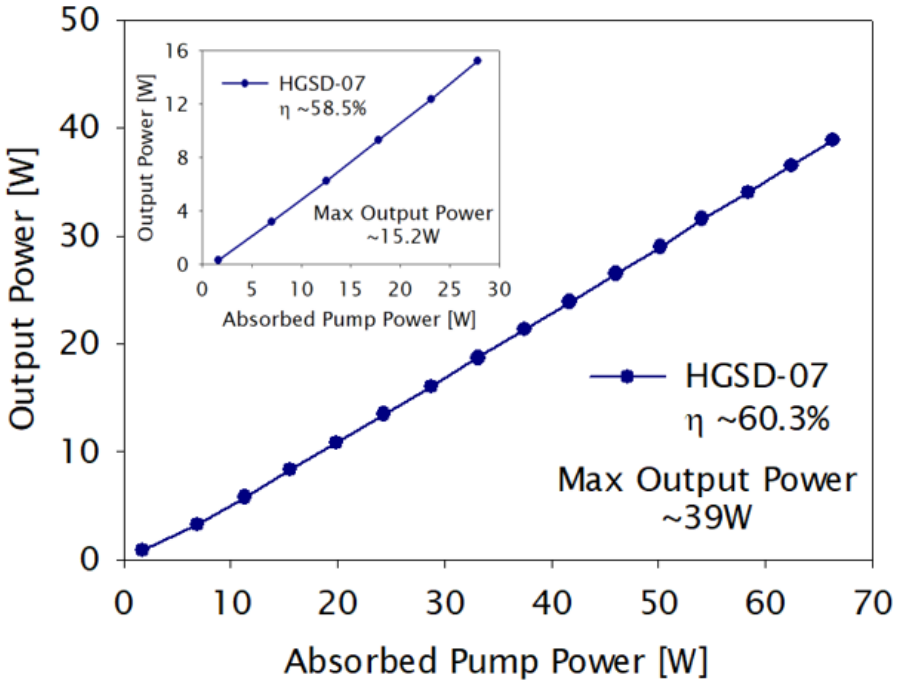

Graph 24. HGSD-07 (Tm ~2wt%) laser efficiency. Inset: performance at low power

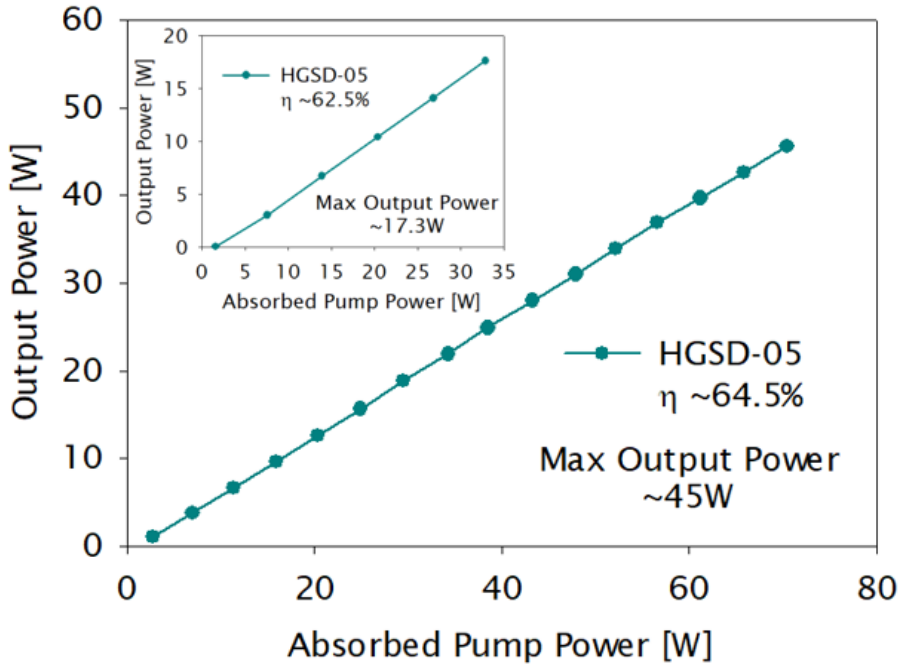

Graph 25. HGSD-05 (Tm ~3wt%) laser efficiency. Inset: performance at low power

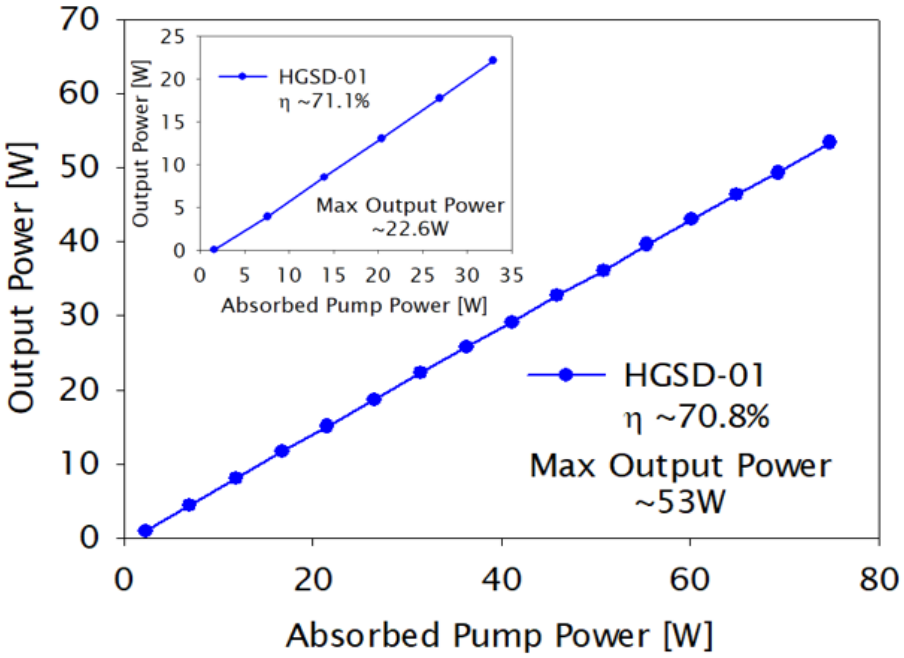

Graph 26. HGSD-01 (Tm ~3.8wt%) laser efficiency. Inset: performance at low power

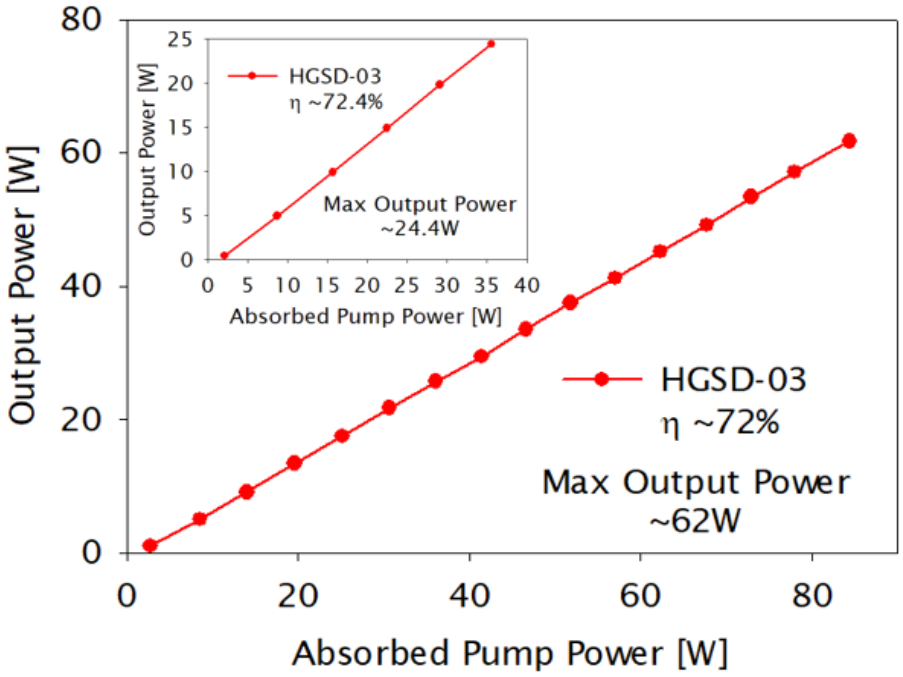

Graph 27. HGSD-03 (Tm ~5.6wt%) laser efficiency. Inset: performance at low power

The efficiency of TDFLs at their free-running emission was also measured by varying the fibre length for different thulium concentrations. The aim was to establish the spectral region where the TDFL would perform efficiently depending on the thulium concentrations. This has been applied to two Tm-doped fibers fabricated using the hybrid gas phase-solution doping process with thulium concentrations of 3.5wt% (HSGD-04) and 5.6wt% (HSGD-03).

Graph 28 shows the normalized emission spectrum at different wavelengths with the corresponding fibre length and the laser efficiency. Due to the characteristics of the fibre composition and the improved dispersion of the dopants within the core as a consequence of the aluminium deposition by vapour phase, a laser efficiency of 70±3% is maintained, covering the wavelength region from 1980nm to 2080nm.

It is worth mentioning that for a given laser system with an emission wavelength of ~2030nm, it is possible to use 12m of the HGSD-04 or 8m of the HGSD-03 with a Tm concentration of 5.6wt%, shortening the laser cavity due to the higher dopant concentration of the fibre, obtaining similar laser efficiencies.

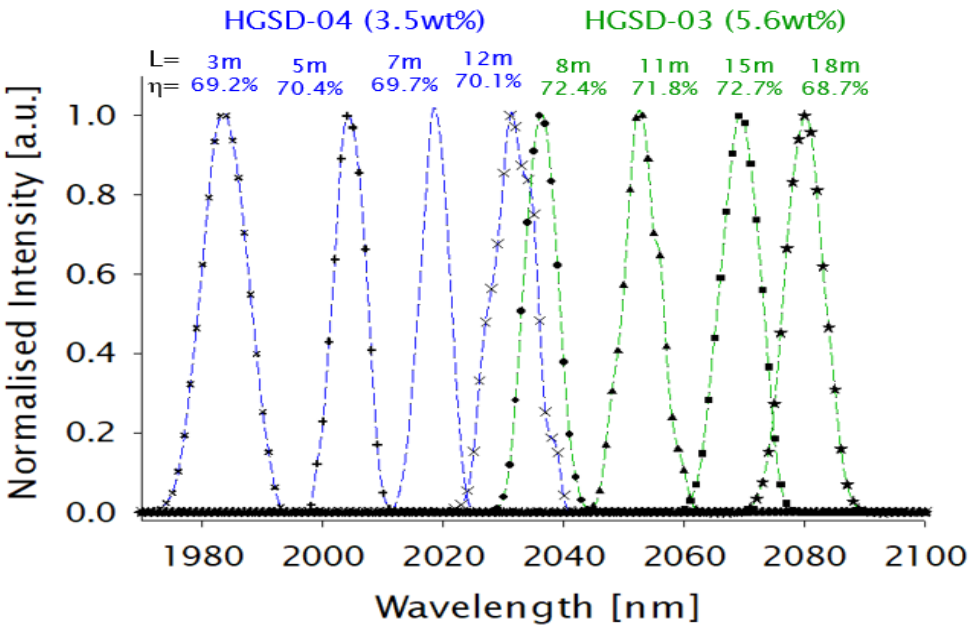

Graph 28. Emission spectra and laser efficiencies of HGSD-04 and HGSD-03 fibres

It is clear from Graph 28 that the laser tends to perform better at longer wavelengths for thulium concentrations >5wt%, whereas a lower thulium concentration of ~3.5wt% is needed when considering efficient operation at shorter wavelengths.

4.3 Thulium-doped fibre laser at 1950nm (Intro)

As mentioned in Chapter 1, due to the high absorption of liquid water and biological protein components available in humans and other animal species, thulium-doped fibre lasers have shown significant potential for medical applications.

However, the operation around 1950nm or below suffers from reabsorption losses. Moreover, in order to maintain an efficient two-for-one cross-relaxation process with ~70% of efficiency, a thulium concentration of ~3.5wt% has to be exceeded, leaving a fibre NA > 0.2 and a limited range availability in the core size for single mode operation. Therefore, the fibre design must include an analysis of the core composition, clad/core diameter and clad/core ratio.

As the NA cannot be reduced without compromising the laser efficiency, it is possible to create a local area surrounding the core that will produce a new primary cladding with a new local refractive index. Consequently, the core NA will be reduced as the change in the refractive index will take this new structure as cladding. This raised new structure is commonly known as a pedestal.

It is important to mention that this new design and the fabrication of an aluminosilicate pedestal were done as additional experiments to this thesis and unfortunately, due to the early closure of the facilities within the university (COVID-19), there was no continuity. In addition, in order to completely understand the nature of the pedestal structure, more background literature is required, which is not covered in this thesis.

4.3.1 Preliminary test

The HGSD-07 fibre length was adjusted in a free-running laser cavity in order to get an emission wavelength ~1950nm. With a core composition of 13.6wt% of Al_2O_3 and 2.3wt% of Tm_2O_3, the actual NA is 0.24. It is worth mentioning that for an optimum fibre length of 12m, the emission wavelength was ~2000nm with a laser efficiency of ~60% and 39W of laser output.

As shown is Graph 29, it is possible to achieve an emission wavelength at 1950nm.

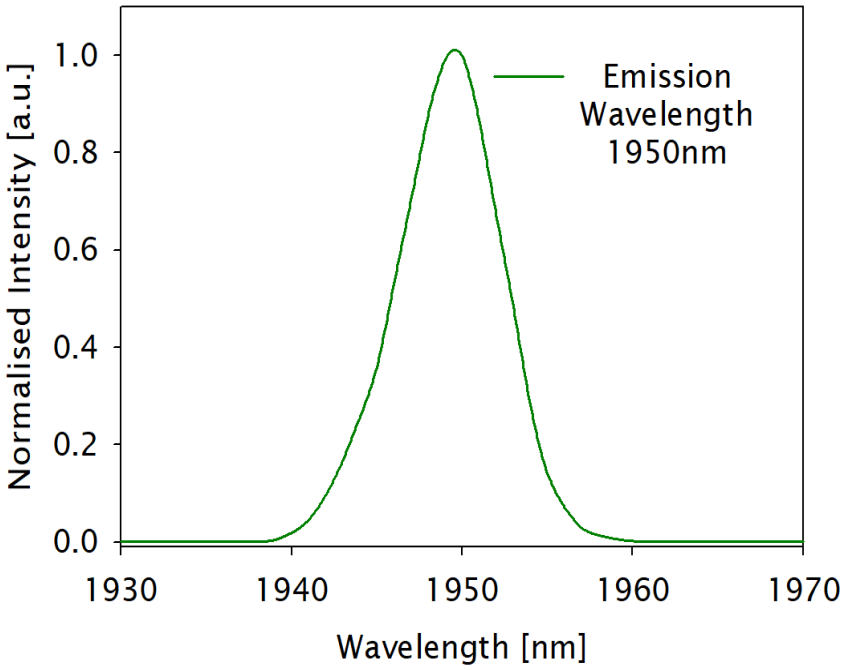

Graph 29. HGSD-07 emission wavelength at 1950nm

However, as shown in Graph 30, the laser efficiency drops considerably due to a combined effect of the core composition, reabsorption and a non-optimised design. Nevertheless, it was possible to obtain a maximum laser efficiency of 23% with respect to the absorbed pump power and a maximum output power of ~16W.

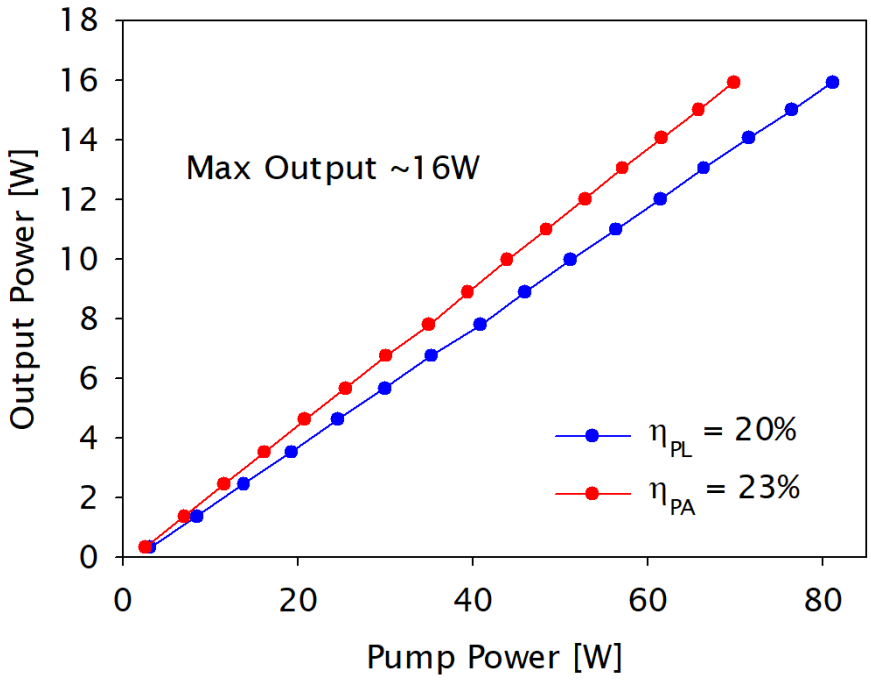

Graph 30. HGSD-07 laser efficiency at 1950nm

4.3.2 Pedestal structure design

The current commercial fibres available with a pedestal structure have a fibre core diameter of ~25µm and are drawn between 200µm and 600µm. It is commonly seen that the pedestal structure is ~5 times bigger than the core. Therefore, this design tries to match a fibre specification of 25µm/600µm core cladding diameter. The design characteristics are shown in Table 9.

Table 9. Clad/Pedestal/Core design

Type of tube	Suprasil F300 (Heraeus)
Tube outer diameter	20mm
Tube inner diameter	16mm
Cross Sectional Area	113mm^2
Fibre clad diameter (required)	600µm
Fibre core diameter (required)	25µm
Fibre clad/core ratio	24
Fibre pedestal diameter (expected)	115µm
Preform clad diameter (expected)	12mm
Preform pedestal diameter (estimated)	2.4mm
Preform core diameter (estimated)	0.5mm
Preform clad/pedestal ratio	5
Preform clad/core ratio	24

As this was the first fabrication with a pedestal structure, the design for a single mode operation was postponed. Similarly, as the clad/core ratio from the preform and fibre were the same and this was the initial test, no additional post process was required.

The core composition was expected to be around 7wt% of Tm_2O_3 and 15-18 wt% of Al_2O_3 with an NA of ~0.1. The estimated core composition and refractive index contribution is presented in Table 10 followed by the schematic design of the thulium-doped fibre with a pedestal structure in Graph 31.

Table 10. Pedestal structure refractive index calculations

Compound	Conc. [wt%]	Molar mass	Conc. [mol%]	Δn (calculated)
SiO2	75-78	60.08	86-89	----
Al2O3	15-18	101.96	10-12	0.022-0.026
Tm2O3	7	385.87	1.23	0.0083-0.0084
Total	100	----	100	0.030-0.035

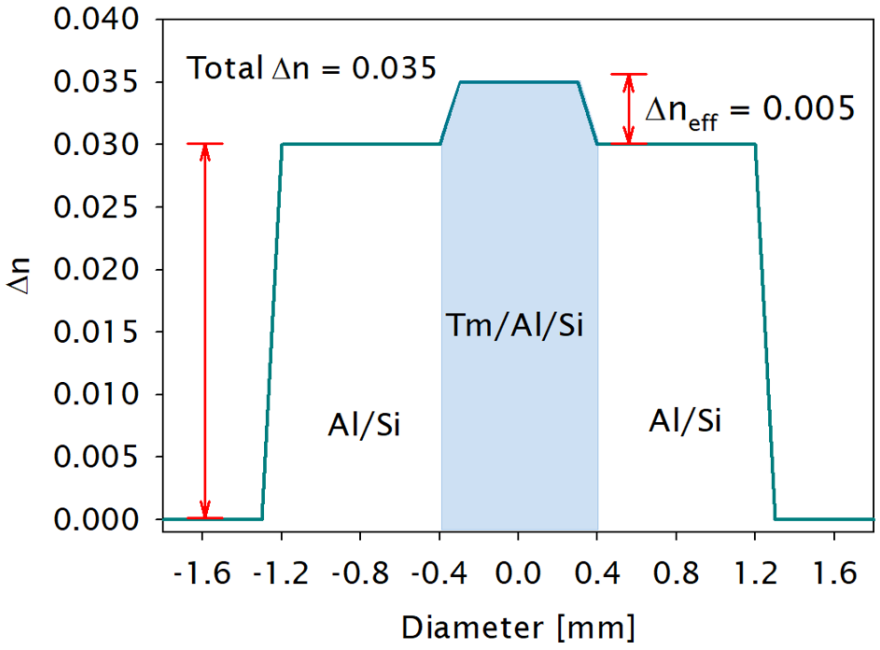

Graph 31. Thulium-doped fibre with pedestal structure design

4.3.3 Thulium-doped fibre with pedestal structure fabrication

The fabrication process was divided into two steps: first the MCVD process in combination with the vapour phase deposition for the aluminosilicate pedestal and second the hybrid gas phase solution doping technique. The process started with a high quality silica tubes (F300 from Heraeus) with a nominal 20x16mm diameter and 500mm length.

First, a silica substrate tube was cleaned in the MCVD lathe using sulphur hexafluoride (SF_6) at high temperature. Subsequently, several layers of SiO_2 were deposited to work as a matching interface between silica from the tube and silica that reacted from $SiCl_4$ and O_2. Then, in order to build a pedestal structure of

~2.4mm, two aluminosilicate layers with a reduced refractive index were deposited to minimise the gradient difference between the SiO_2 layers and Al_2O_3/SiO_2 layers with a high refractive index. Consequently, a series of aluminosilicate layers were deposited and sintered to form the pedestal structure. As presented in Image 16, after a couple of aluminosilicate layers, the tube glass looks transparent just after the burner passes the reaction zone, confirming that the sintering was performed successfully, leaving only the characteristic fume of silica which is always formed within the cold zone of the tube.

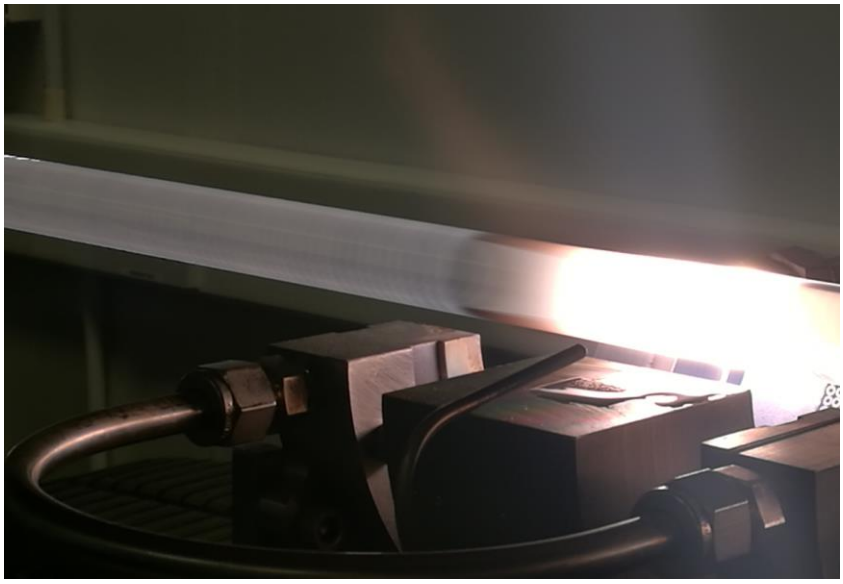

Image 16. Fully sintered aluminosilicate layers for pedestal structure

As the hybrid gas phase solution doping technique dictates, an unsintered aluminosilicate layer was created. Then, the substrate tube was removed from the MCVD lathe for the solution doping with thulium chloride ($TmCl_3.xH_2O$, 99.9999%) and reassembled again for oxidation and sintering of the core layer.

Finally, the tube was intended to be collapsed into a solid rod in the usual manner but an unexpected event near the tailstock of the lathe, accidentally stopped the rotation for a couple of seconds which unfortunately start to soften and melt down the glass of the tube as is shown in Image 17.

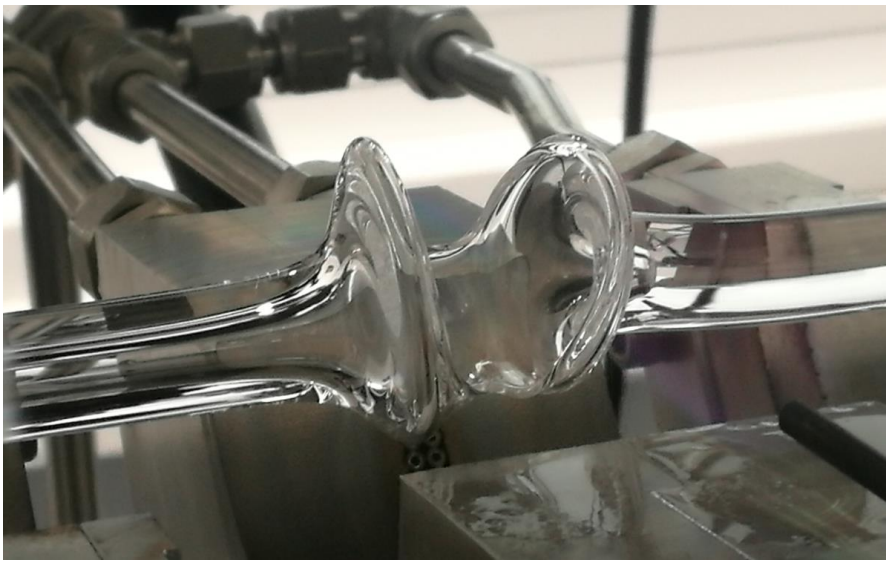

Image 17. TDF pedestal structure fail fabrication

As the tube was almost fully collapsed, the two remaining tubes were spliced again to be collapsed into a solid rod. During the collapse and final sealing of the tube, a whitish coloration within the core was observed, which is a clear indication of high aluminium incorporation as shown in Image 18.

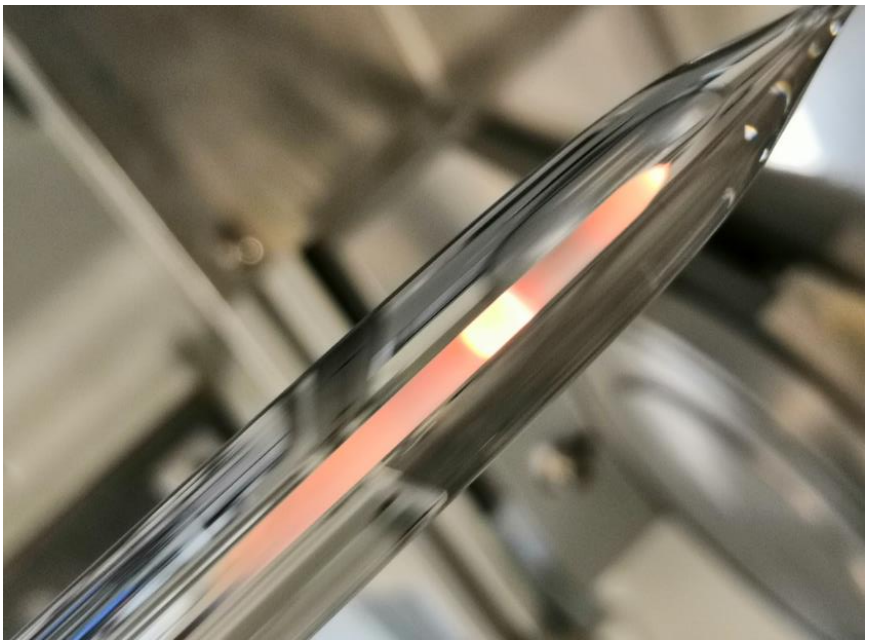

Image 18. Tm-doped preform with aluminium pedestal structure

This effect can be explained as a phase separation of the aluminium within the silica matrix when the aluminium concentration is relatively high and exposed to high temperature.

4.3.4 Thulium-doped fibre (pedestal structure) results

The refractive index profile was analysed with a PK2600 to visualise the impact of the pedestal structure and the hybrid technique. The estimated and measured refractive index profile is presented in Graph 32.

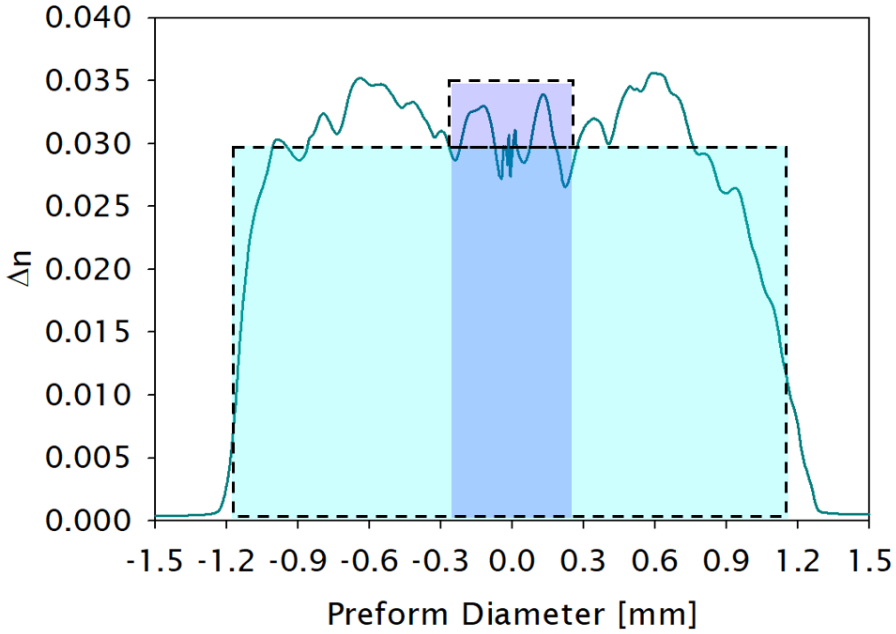

Graph 32. Thulium-doped fibre with pedestal structure profile

Unfortunately, due to external circumstances to the University of Southampton and the author's PhD studies (COVID-19), no further analysis was made to the preform and no fibre was drawn, holding all activities in standby.

4.4 Summary

A set of highly efficient thulium doped fibers were fabricated by combining solution doping and vapour phase deposition techniques in conjunction with the MCVD process were successfully demonstrated. The proposed fabrication route allows high Al_2O_3 incorporation into the silica matrix and a more uniform distribution of thulium ions across the fibre core region, leading to an efficient two-for-one cross-relaxation process in Tm-doped fibers with ~790nm pumping and therefore shows high slope efficiencies of >70%, which is >90% of the theoretical limit in the two-micron band.

Our study shows that a thulium concentration of about ~3.5wt% with a more uniform dopant profile is sufficient to maintain high slope efficiencies in TDFLs without going for much higher thulium concentrations. With a lower thulium concentration, the thermal load density in fibre will be reduced, and higher output power can be achieved in the two micron band without thermal damage.

The proposed technology also makes it possible to fabricate a large-mode-area Tm-doped fibre with a pedestal design, comprised of alumino-silicate layers that surround the core and are deposited via the vapour phase deposition process. Such pedestal layers, compared to germanium and/or phosphorous-doped silica layers, will significantly reduce the thermal mismatch with the silica cladding, offering much greater flexibility when there is a need for depositing a large pedestal and fabrication of a polarization-maintained fibre in a pedestal geometry.

Chapter 5 Towards the 2.1 μm band: Tm:Ho co-doped silica fibres

5.1 Introduction

Over the last decade, thulium-doped fibre lasers and holmium-doped fibre lasers have shown significant progress in the longer side of the near infrared region from 1800nm to 2200nm due to their energy level transitions Tm^{3+}: $^3F_4 \rightarrow {}^3H_6$ and Ho^{3+}: $^5I_7 \rightarrow {}^5I_8$. In TDFLs, when cladding is pumped at ~790nm, where the high power diodes are available, an excited Tm3+ ion in the $^3H_4$ manifold interacts with a nearby ground state ion in the 3H6 manifold, producing two excited ions to lase from the 3F4 manifold (two-for-one cross-relaxation process), reaching a quantum efficiency up to 200% in the two micron region[49].

In contrast, the Ho^{3+} ions have no absorption bands where high power diodes are currently available[118]. For accessing wavelengths beyond 2.1μm, the main absorption band for HDFLs lies at ~1.95μm ($^5I_7$ manifold). Consequently, an in-band pumping scheme using TDFLs as the pump source is commonly used[15,119]. However, the laser efficiency of ~790nm diode pumped TDFLs operating at ~1.95μm is somewhat less than when operating beyond 2μm[14]. As a result of this, the overall electrical-to-optical conversion efficiency of lasers operating at 2.1μm could suffer.

Moreover, the implementation of this pumping scheme brings additional complexity to fibre fabrication due to the need for an all-glass fibre structure with a fluorine doped cladding for low-loss pump guidance, as low-index polymer used in standard double clad fibers will incur a strong absorption in the 2μm region[12,55,120].

As an alternative to the in-band pumping scheme, co-doping of silica fibres with thulium and holmium can be considered[17,121]. In this case, ~790nm pump can be utilized to excite thulium ions and promote the two-for-one cross-relaxation process, followed by a dominant donor-acceptor energy transfer mechanism from thulium $^3F_4$ manifold to holmium $^5I_7$ manifold[59,122]. Laser sources based on the Tm:Ho co-doped silica fibres have been reported with a slope efficiency up to 42%[16] and it has been suggested that an improvement in the laser performance could be achieved with an optimized fibre core composition.

In this chapter, the effects of thulium and holmium dopant concentrations on the energy transfer efficiency between donor (Tm^{3+}) and acceptor (Ho^{3+}) ions and the laser performance at 2.1 μm in Tm-Ho co-doped silica fibers when cladding pumped at ~790 nm are studied.

5.2 Experimental Work

Preforms with 2wt% and 5wt% of Tm^{3+} concentrations and three different Tm/Ho concentration ratios of 5, 10 and 20 respectively were fabricated by the MCVD process in combination with a hybrid gas phase-solution doping technique. In addition, holmium free Tm-doped preforms with the same Tm^{3+} concentrations were fabricated and used to compare the performance and output characteristics. It is worth mentioning that a Tm^{3+} concentration greater than 2wt% is necessary to utilize a two-for-one cross-relaxation process in TDFL with 790nm pumping.

5.2.1 Preform fabrication

In the first step, cladding layers of silicon oxide (SiO_2) were deposited inside a substrate tube (Suprasil F-300) followed by an aluminosilicate soot layer deposited using the vapour phase deposition technique. The aluminium chloride ($AlCl_3$, 99.999%) was heated at ~140°C and the generated vapour was transported to the deposition zone through a dedicated delivery line using helium (He) as a carrier gas. As explained in Chapter 3 and Chapter 4, for different $AlCl_3$ flow, the soot deposition temperature and Si/Al ratio were adjusted to maintain good control over rare earth incorporation during the solution doping stage.

Then, the preforms were removed from the MCVD lathe and soaked in a solution of methanol containing thulium chloride ($TmCl_3.xH_2O$, 99.9999%) and holmium chloride ($HoCl_3.xH_2O$, 99.999%). The dopant concentrations in the solution were adjusted for getting a specific Tm/Ho ratio in the fabricated preforms.

An example of the solution doping stage is presented in Image 19.

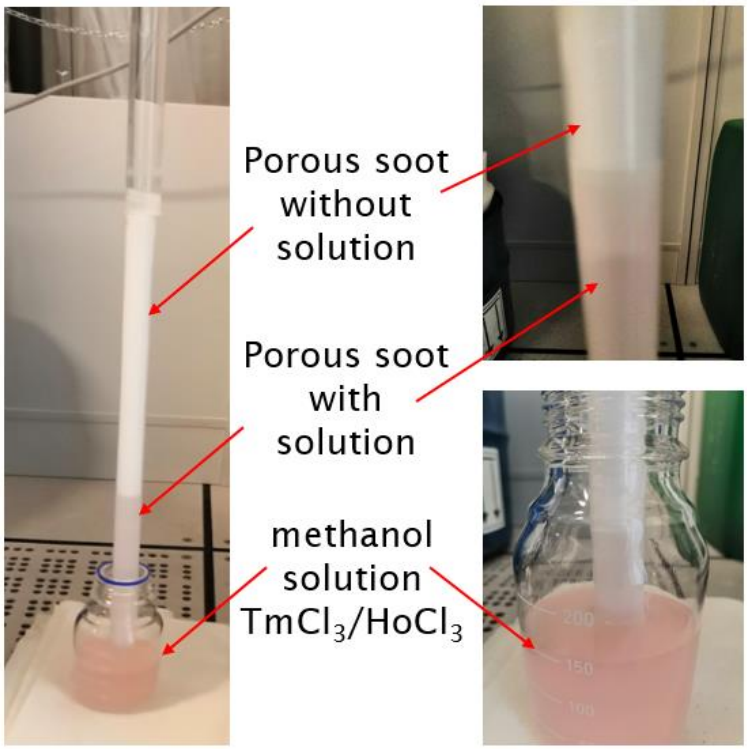

Image 19. Tm/Ho solution doping stage

Follow the solution doping, the tubes were reassembled on the MCVD lathe. As the ratio of the incorporated dopants by vapour phase deposition was adjusted at the same time as the deposition temperature, an improvement in the soot thickness and solution retain was noticed. As presented in Image 20, no cracking was observed in high thulium concentration preforms (compared to preforms fabricated in Chapter 4) which resulted in a totally cleared sintered layer.

Image 20. Enhanced porous soot layer after solution doping

Then, the core layer was oxidised and sintered. Image 21 shows the characteristic pink glowing of holmium chlorides when they are exposed to oxygen during the oxidation stage. The different intensity of the glow is due to the different concentration ratios of the Tm:Ho co-doped preforms.

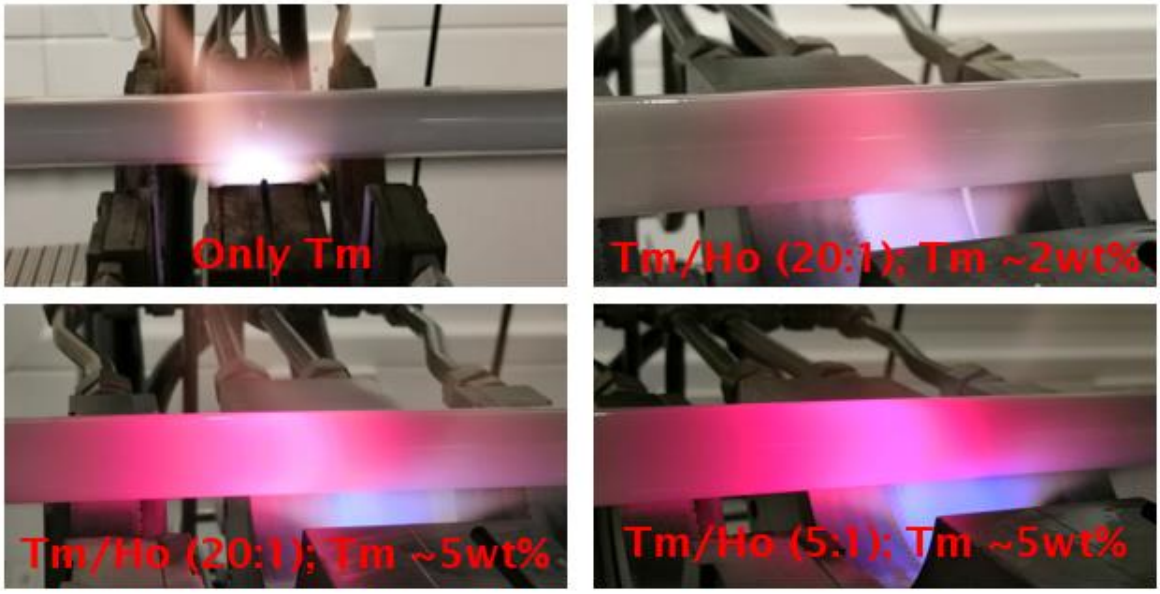

Image 21. Tm:Ho co-doped preforms oxidation stage

Finally, the preforms were collapsed into a solid rod in the usual manner followed by a post-process that achieved a core diameter of ~8μm in the final fibre. Additionally, the circular cladding was modified into a quasi-octagonal (Q_Oct) shape for enhanced pump absorption in a double clad fibre. The TDF and the THDF were drawn to a fibre diameter of 200μm and coated with a low index polymer. The post processing steps and timing for each step is summarized in Table 11.

Table 11. Tm and Tm/Ho post processing stages

Sleeving 1 (4 hours)	
Initial preform diameter	~12mm
Sleeving tube size 1 (start)	25mmx19mm
Sleeving tube size 1 (end)	22mmx14mm
Core size 1	~1.9mm
*Core size if drawn to 200μm	~17μm
Stretching 1 (2 hours)	
Initial preform diameter	~20mm
Core size 1	~1.9mm
New core size	~0.6mm
New preform diameter	~8mm
Sleeving 2 (4 hours)	
Initial preform diameter	~10mm
Sleeving tube size 2 (start)	20mmx16mm
Sleeving tube size 2 (end)	16mmx10mm
Core size 2	~0.6mm
*Core size if drawn to 200μm	~8μm
Milling (2 hours per side)	
D shape (Quasi Octagonal)	4 sides
Drawing (3 hours)	
Preform dimensions	15mmx0.6mm
Fibre dimensions	200μmx8μm

5.2.2 Characterisation

The optical absorption of the fibers was obtained by using a white light source and an optical spectrum analyser. The absorption was evaluated at ~790nm, which corresponds to the thulium absorption band. As the thulium concentration was kept constant, similar absorption in Tm-doped and Tm:Ho co-doped fibres was expected. The cladding absorption spectrum of the F-005 (TDF) and F-007 (THDF) at ~790nm is shown in Graph 33.

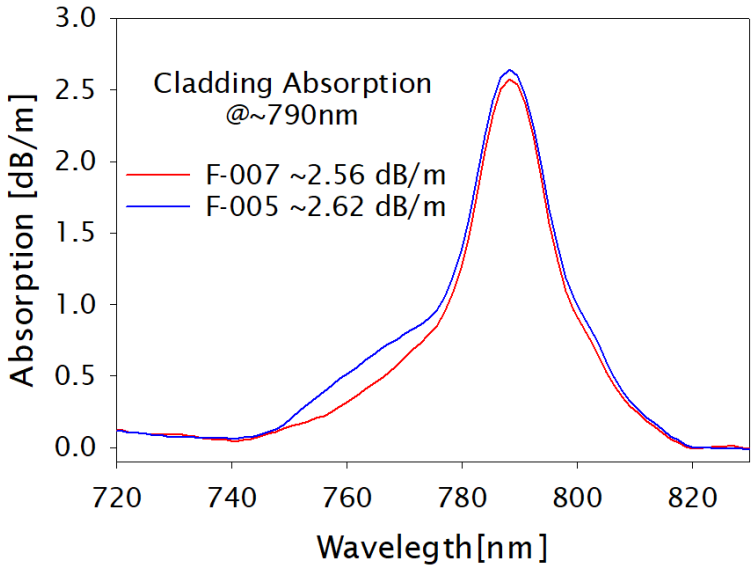

Graph 33. Spectral absorption of the Tm and Tm:Ho co-doped fibres

The fibre refractive index profiles were measured with an IFA-100. Figure 24 shows the two-dimensional refractive index profile of a Tm:Ho co-doped fibre (F-007) and the inset shows the core region without defects in the core/cladding interface.

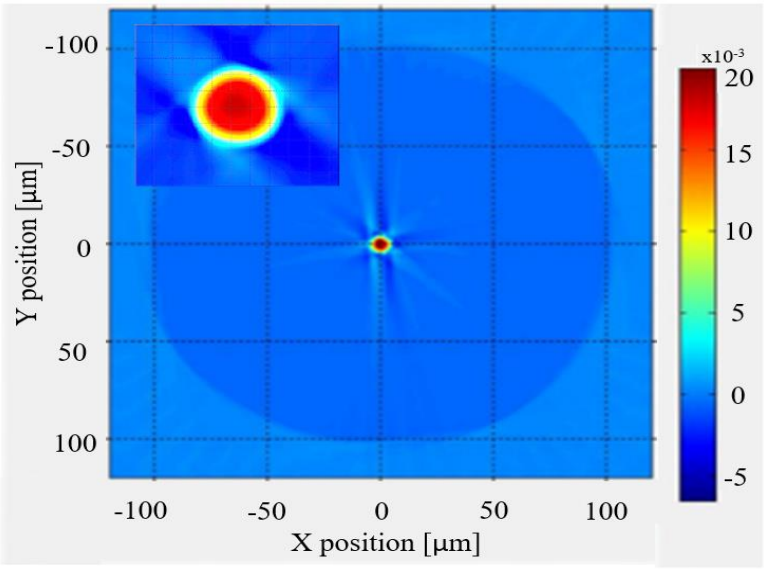

Figure 24. Tm:Ho co-doped fibre two-dimensional fibre refractive index profile

The correspondent dopant distribution and concentrations of aluminium, thulium and holmium in the fibers were measured in collaboration with Dr. Miguel Nunez-Velazquez by an Electron Disperse X-ray spectroscopy. To verify the EDX results, the measurement was performed 4 times: two in the preform (extreme sides of the preform) and two directly to the drawn fibre. An example of the dopant distribution is presented in Graph 34, which exhibits a homogeneous dispersion of the dopants within the core region and the characteristic of flat-top from the hybrid gas phase solution doping technique.

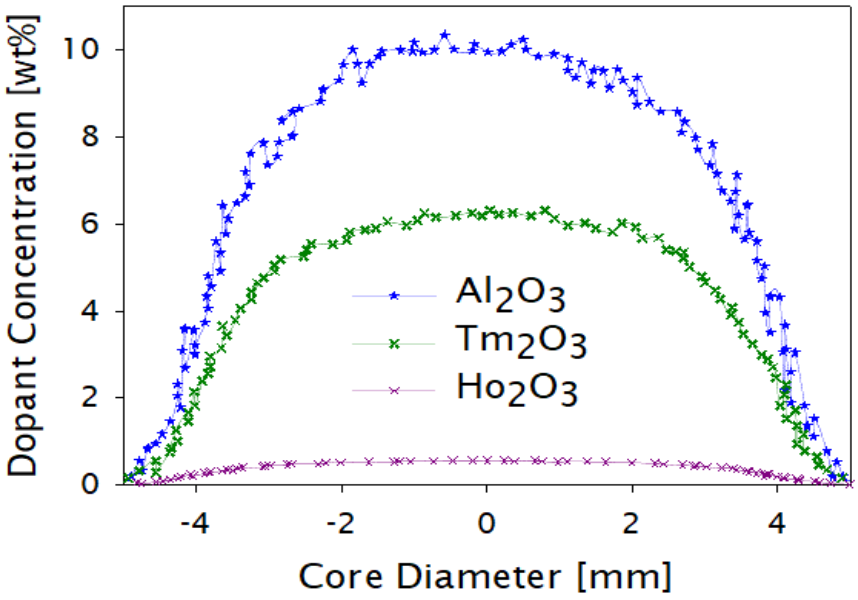

Graph 34. Tm:Ho co-doped fibre dopant distribution (F-007)

The characteristics of the fabricated fibres are summarized in Table 12. This new batch of fabricated fibres presents concentration characteristics similar to the single thulium doped fibres from the previous chapter, with the difference that it was aimed for higher aluminium oxide content, as more than 5wt% of thulium oxide and holmium were added to the aluminosilicate matrix. Thus, a proper dispersion of the dopants within the core was needed.

Table 12. Tm and Tm:Ho co-doped fibres characteristics

Fibre	NA	Core Abs at 790nm [dB/m]	Tm_2O_3 [wt%]	Ho_2O_3 [wt%]	Al_2O_3 [wt%]
F-001	0.24	770	2.35	----	13.66
F-002	0.25	820	2.4	0.11	11.31
F-003	0.25	750	1.84	0.17	9.96
F-004	0.24	850	2.04	0.41	9.58
F-005	0.27	1670	6.44	----	11.65
F-006	0.29	1650	5.2	0.22	13.1
F-007	0.28	1530	6.32	0.56	10.24
F-008	0.29	1840	5.38	1.0	13.25

Due to various situations beyond the control of the Silica Fabrication Group, (for example, an unexpected extraction shutdown of the clean room and a fire alarm within the building) several attempts were done during the F-006 fabrication. However, these situations help to verify the fabrication consistency and the dopants incorporation as presented in Table 13~~Table 12~~.

Table 13. F-006 dopant characteristic

Fibre	Tm_2O_3 [wt%]	Ho_2O_3 [wt%]	Al_2O_3 [wt%]
F-006.1	5.19±0.15	0.23±0.06	11.7±0.12
F-006.2	5.33±0.12	0.25±0.04	11.37±0.1
F-006.3	5.2±0.16	0.22±0.03	13.1±0.12
F-006.4	5.05±0.13	0.27±0.04	11.01±0.09

5.2.2.1 Fabrication consistency

Regardless of the unexpected situations during the four attempts of F-006, the refractive index profile from each preform was analysed with a PK2600. The profiles in Graph 35 show a consistency in the preform fabrication process using the hybrid gas phase solution doping technique.

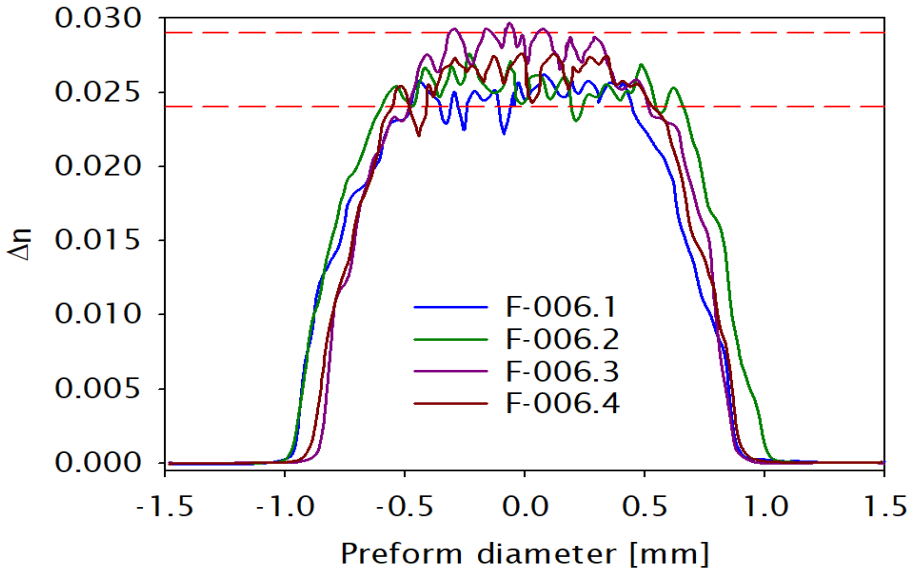

Graph 35. F-006 preforms refractive index profile (several attempts)

Considering the high Al_2O_3 and Tm_2O_3 concentration in each preform, the Δn difference between preforms is 0.0265±0.0025. However, further optimization needs to be done.

5.2.2.2 Energy transfer efficiency

The fluorescence lifetime of the Tm and Tm:Ho co-doped fibers was analysed to determine the Tm^{3+} to Ho^{3+} energy transfer, which can be observed by a shortening of the Tm^{3+} florescence decay time in the co-doped fibers as shown in Graph 36 and Graph 37. Lifetime from the $^3F_4$ energy level manifold in thulium was measured under ~790nm pulsed pump light with a modulation frequency of 10Hz and 10% duty cycle.

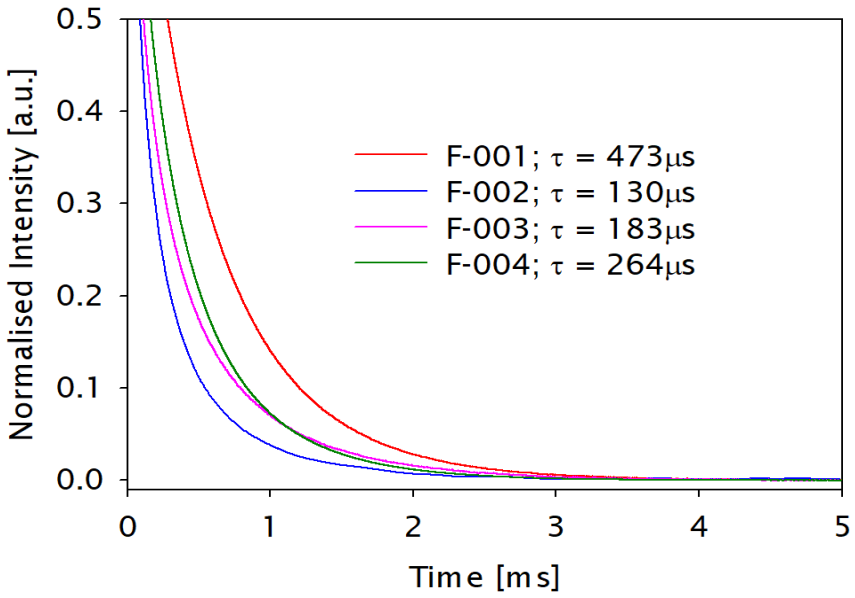

Graph 36. Fluorescence lifetime decays of Tm and Tm:Ho fibres with Tm^{3+} ~2wt%

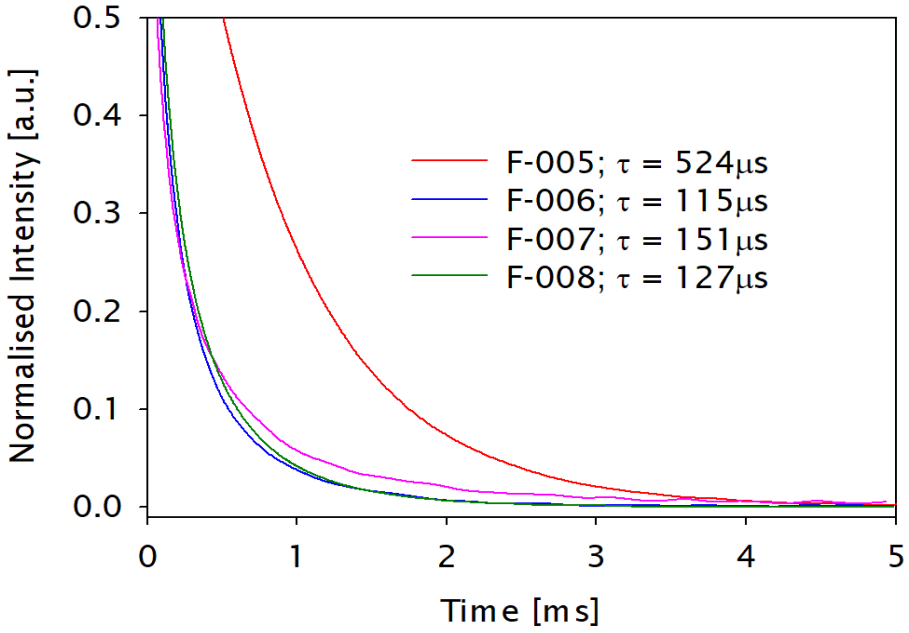

Graph 37. Fluorescence lifetime decays of Tm and Tm:Ho fibres with Tm^{3+} ~5wt%

An InGaAs photo-detector and a filter to suppress 2.1μm emission were used to capture fluorescence signal from thulium. The lifetime of the excited level was

recorded on an oscilloscope. The efficiency of energy transfer from Tm^{3+} to Ho^{3+} ions was evaluated using Equation 10[123]:

$$\eta_{ET} = 1 - \left(\frac{\tau_{Tm:Ho}}{\tau_{Tm}}\right)$$

Equation 10. Energy transfer efficiency calculation

where, τ_{Tm} is the lifetime of Tm ($^3F_4$ manifold) in absence of holmium and $\tau_{Tm:Ho}$ is the lifetime of Tm ($^3F_4$ manifold) in the Tm:Ho co-doped system.

As shown in Graph 38, there is a significant reduction of up to 3.5 times in the fluorescence lifetime of Tm^{3+} in presence of Ho^{3+}. The change in fluorescence lifetime is a clear indication that the energy transfer process from donor (Tm^{3+}) to acceptor (Ho^{3+}) is occurring. Moreover, as can be seen in the figure, for Tm/Ho ratios of 5 and 10, a higher Tm^{3+} concentration (Fibres: F-007 and F-008) has shown a much faster drop in Tm^{3+} lifetime compared to the lower thulium concentration (Fiber: F-003 and F-004). This is because an efficient two-for-one cross-relaxation process with a higher thulium concentration enables the availability of a greater number of excited ions available in the $^3F_4$ level and hence the energy transfer process from Tm^{3+} to Ho^{3+} is more efficient at a higher thulium concentration.

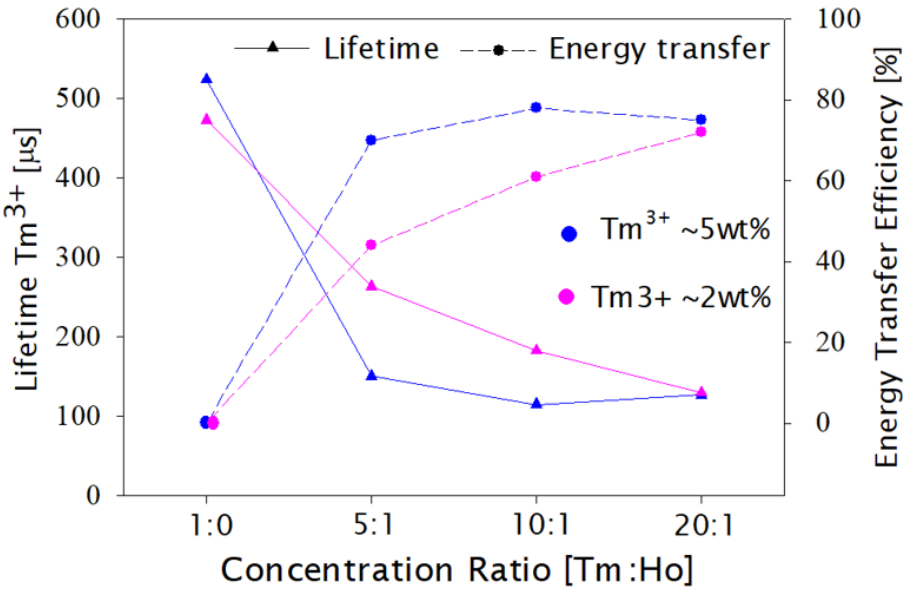

Graph 38. Lifetime of thulium into the $^3F_4$ energy level and the energy transfer efficiency as a function of Tm:Ho concentration ratio

5.2.2.3 Laser efficiency

The Tm-doped and Tm:Ho co-doped fibres were tested in a CW laser configuration when pumped with a ~790nm high power diode. The fibre length in all fibres was adjusted to obtain a maximum output power in a free-running (4% - 4%) cavity.

In the case of the Tm-doped fibre (F-005) with Tm^{3+} concentration ~5wt%, the optimum fibre length was found to be 8m and the corresponding emission wavelength was ~2030nm with a laser efficiency of ~70% as shown in Graph 39.

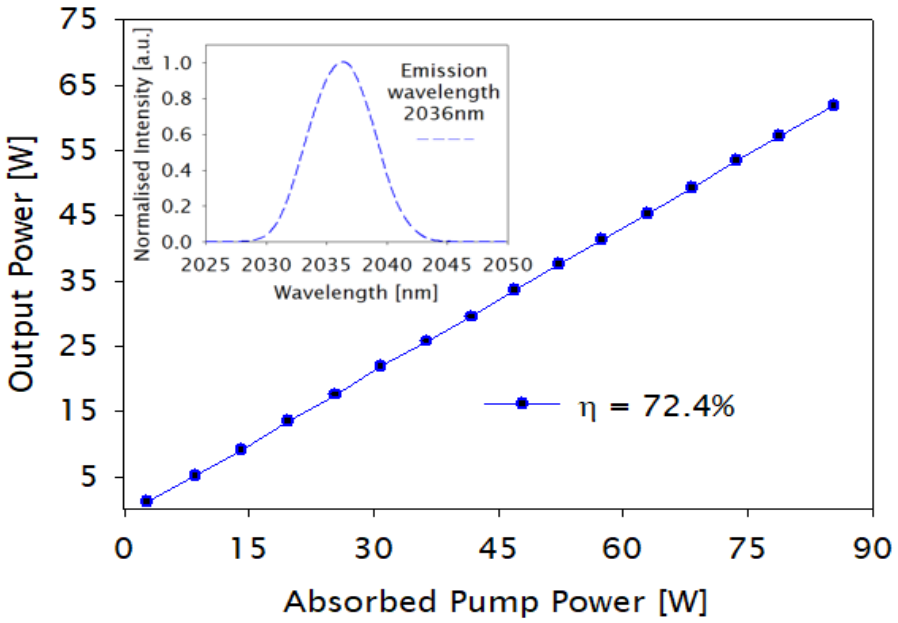

Graph 39. F-005 laser efficiency. Inset: emission at 2036nm

Subsequently, the fibre length was increased up to 30m. For this measurement, the fibre was not placed in any additional cooling system and was only arranged in a 15cm coil diameter. Also, the fibre was not properly distributed within the water-cooled based which produced thermally induced damage when the maximum output power was reached as shown in Image 22.

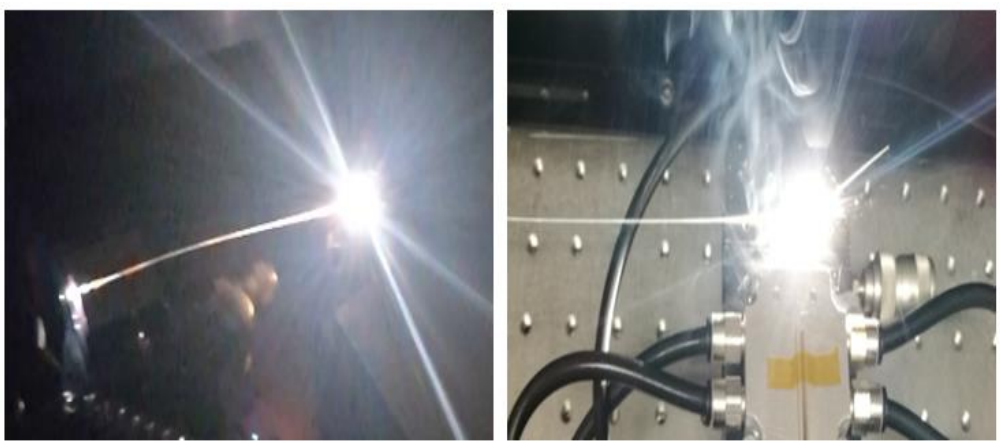

Image 22. 30m TDF burning during laser experiment

Even though the emission wavelength shifted to ~2100nm, the slope efficiency dropped to ~30% as a consequence of a non-optimum fibre length and the thermal induced effects as presented in Graph 40.

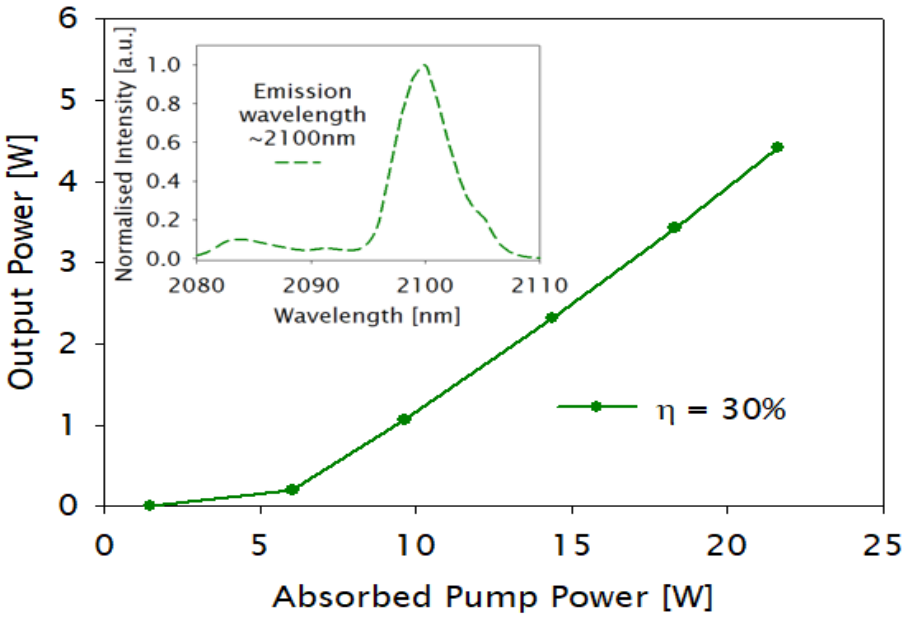

Graph 40. F-005 laser efficiency. Inset: emission at 2100nm

Finally, the slope efficiencies of Tm:Ho co-doped fibers with 2wt% and 5wt% of Tm^{3+} doping concentrations and different Tm to Ho ratios are presented in Graph 41 and Graph 42, respectively. The results of both graphs are summarized in Table 14~~Table 13~~.

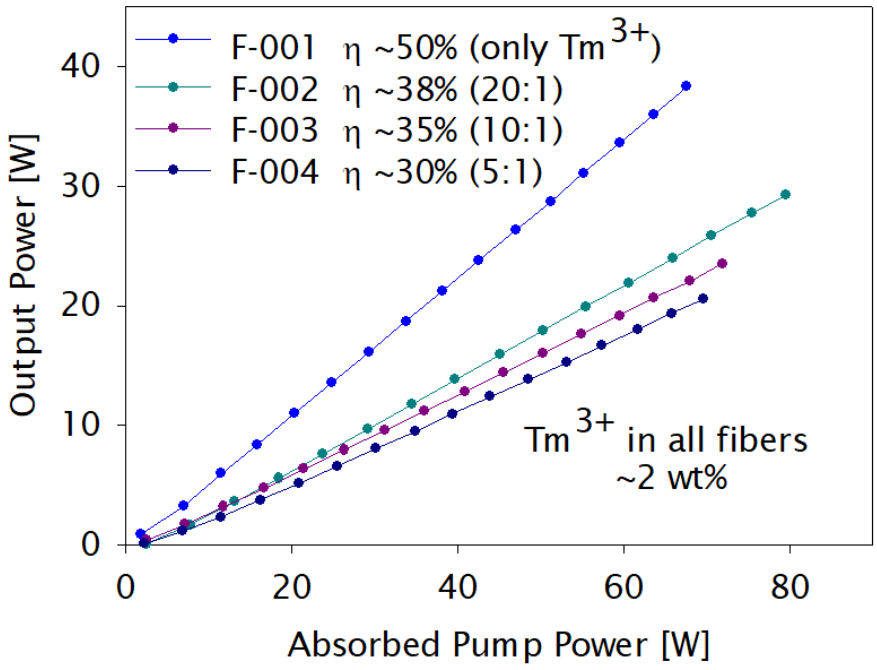

Graph 41. Laser efficiency of Tm and Tm:Ho co-doped fibres (Tm^{3+} ~2wt%)

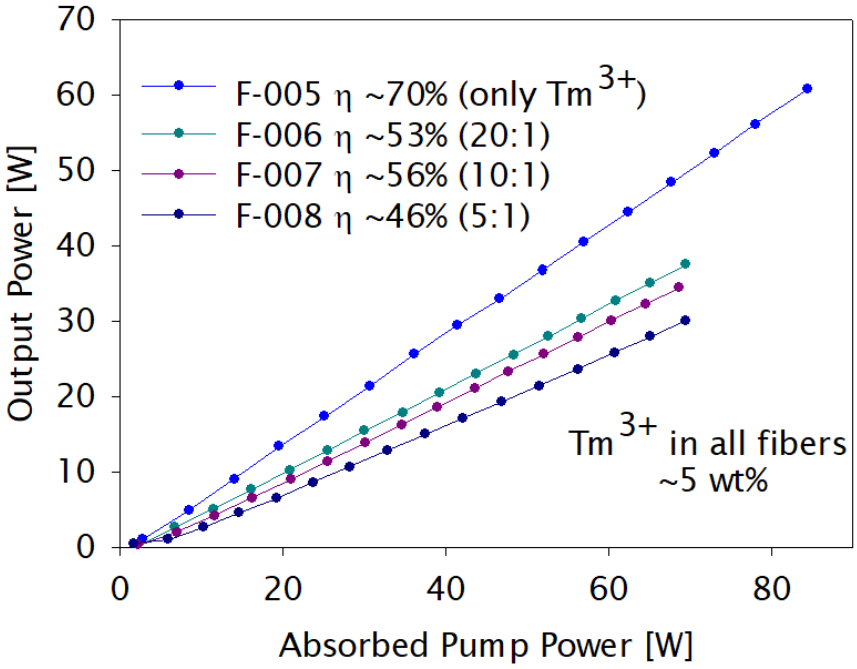

Graph 42. Laser efficiency of Tm and Tm:Ho co-doped fibres (Tm^{3+} ~5wt%)

Our results suggest that a better energy transfer efficiency occurs for Tm:Ho concentration ratios between 10:1 and 20:1. However, in order to achieve a maximum laser efficiency, the thulium concentration requires exceeding 2wt% to promote an efficient two-for-one cross-relaxation process. The results with fibers containing a thulium concentration of ~5wt% support these observations. It is observed that when the Tm:Ho ratio is below 10:1, the laser efficiency suffers. This can be explained by the fact that as the holmium concentration in fibre increases, undesired energy transfer processes between Ho-Ho ion pairs will occur, which will then influence the laser efficiency.

Table 14. Laser and energy transfer performance of Tm and Tm:Ho co-doped fibres

Fibre	Tm:Ho ratio	Length [m]	Emission [nm]	Tm:Ho ET η [%]	Laser efficiency [%]	Output power [W]
F-001	-----	12	2015	-----	50	38.3±0.02
F-002	20:1	13	2090	72	38	29.6±0.01
F-003	10:1	15	2095	61	35	23.5±0.02
F-004	5:1	11	2103	44	30	20.6±0.02
F-005	------	8	2036	------	72	60.7±0.06
F-006	20:1	8	2082	75	53	34.5±0.05
F-007	10:1	7	2105	78	56	37.7±0.07
F-008	5:1	6	2114	70	46	30.1±0.04

As F-002 exhibits the highest efficiency with Tm^{3+} ~2wt% and a concentration ratio of 20:1, the laser performance was analysed as a function of the fibre length. As shown in Graph 43, the Ho^{3+} contribution is noticeable with the emission wavelengths in the range of 2090±10nm.

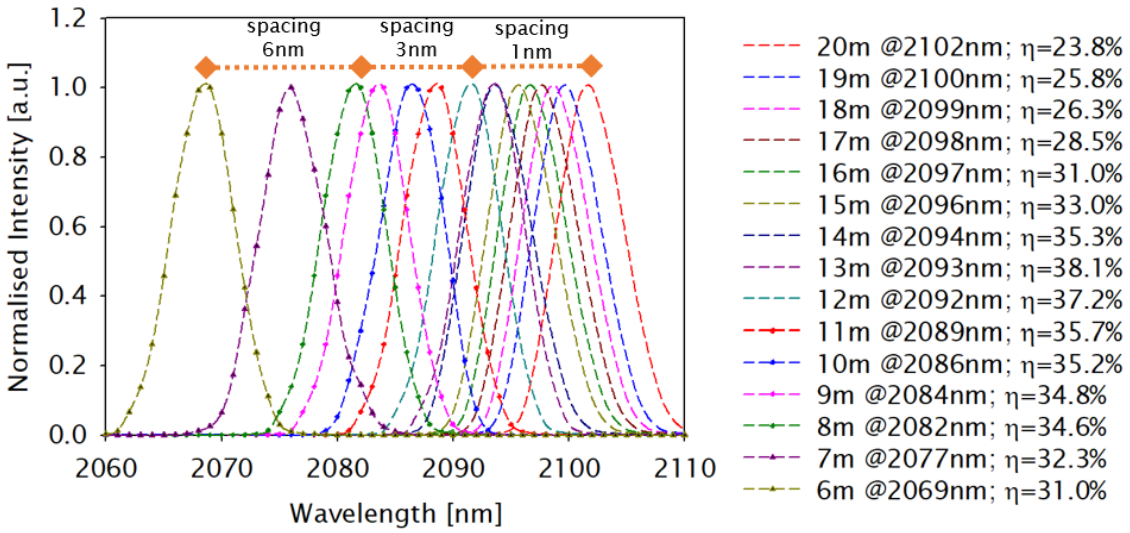

Graph 43. F-002 laser output spectrum as a function of fibre length

Also, F-007 with Tm^{3+} ~5wt% and a concentration ratio of 10:1 was analysed as a function of fibre length. As shown in Graph 44, as the fibre length is shortened, the laser emission in a free running cavity is shifted towards the shorter wavelengths and reaches 2030nm for 1m long fibre, while still maintaining a good laser efficiency, which means that the Tm:Ho co-doped fibres presented in Chapter 5 have the potential for an extended wavelength of operation in the 2.1μm spectral region when diode pumped at ~790nm.

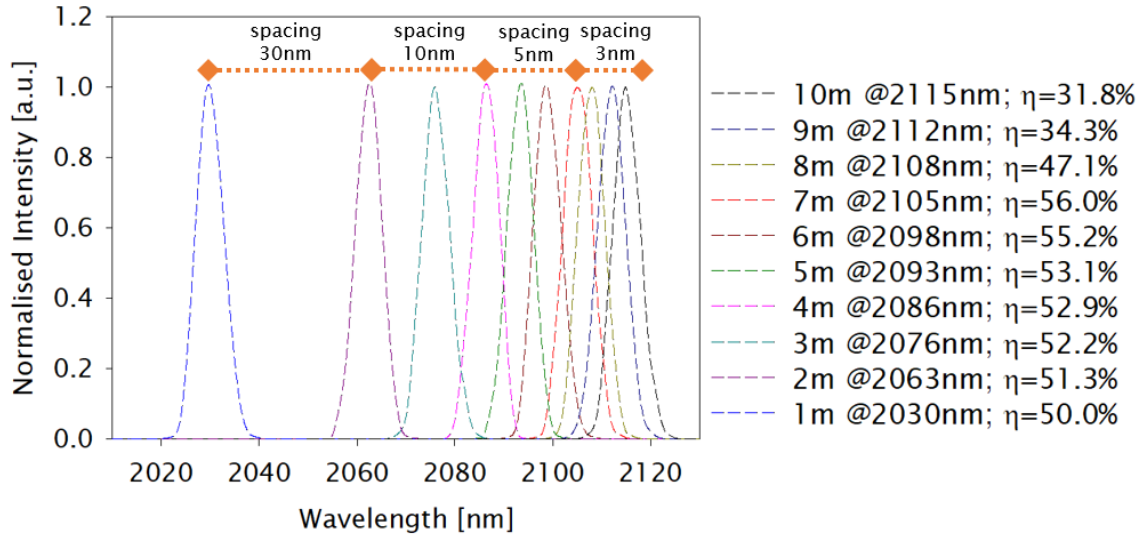

Graph 44. F-007 laser output spectrum as a function of fibre length

In order to verify any detrimental effects or parasitic laser emissions, the emission spectrum was recorded at both ends of the fibre at maximum output power from 150nm to 2400nm, as shown in Graph 45.

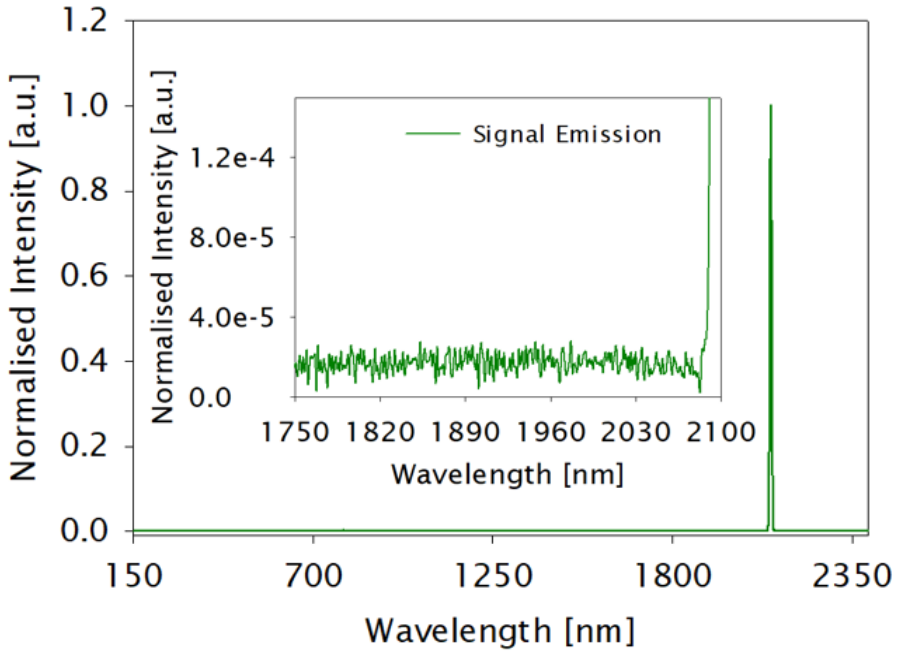

Graph 45. F-007 emission spectrum over 2250nm

Simultaneously, F-007 was tested for power stability and the superficial temperature of the fibre was recorded whilst increasing the pump power, and reached a maximum output power >37W (limited by the available pump power) as shown in Graph 46. A maximum temperature of ~50˚C was maintained during 120 seconds with a small variation in the output power of 0.075W as is demonstrated in Graph 47.

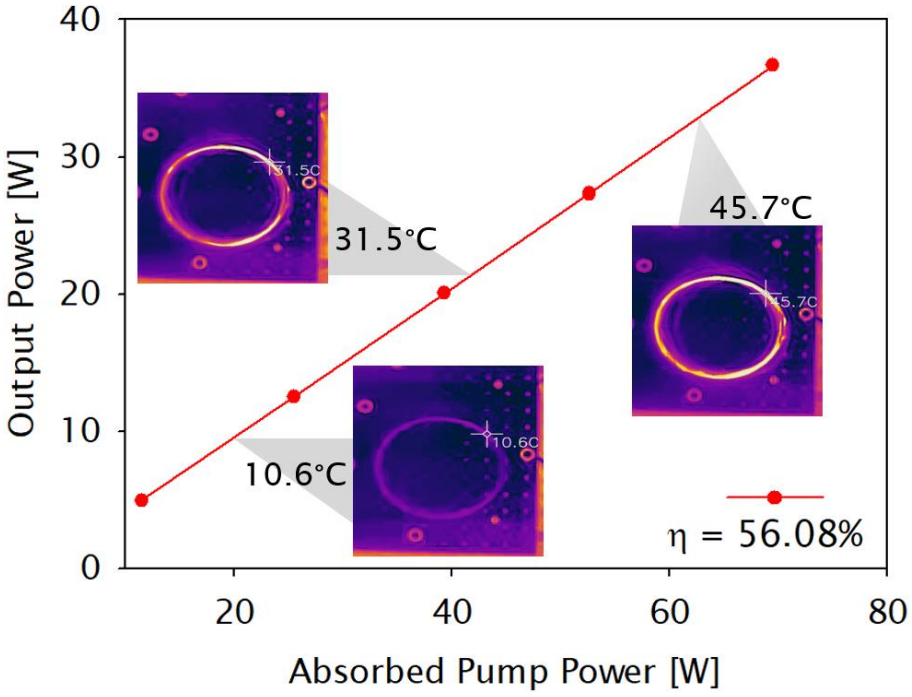

Graph 46. F-007 laser efficiency with fibre temperature at different pump power levels

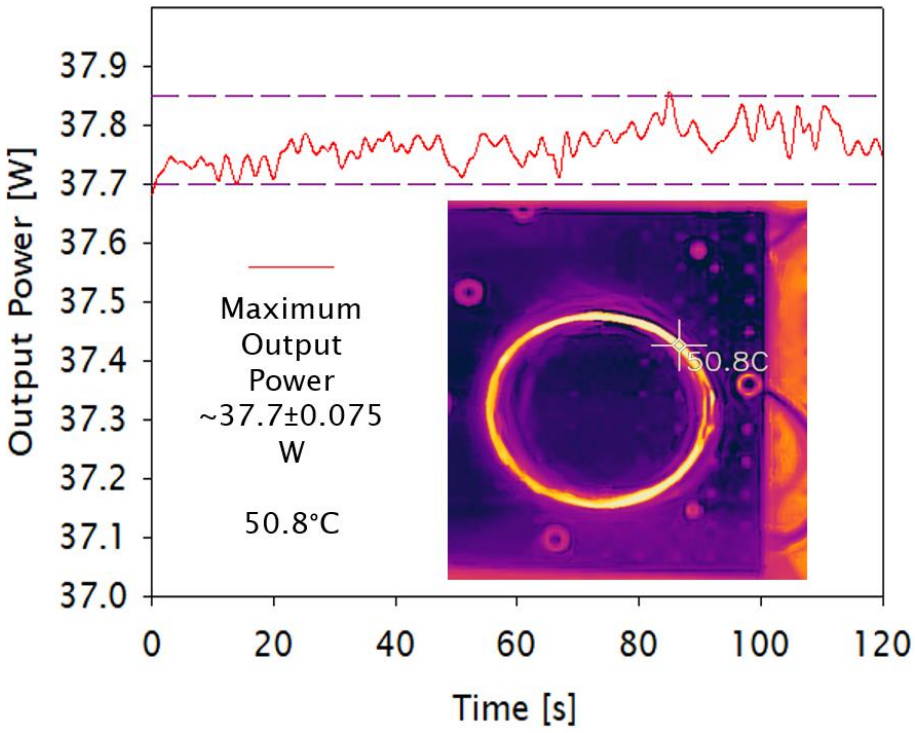

Graph 47. F-007 output power stability. Inset: fibre temperature at max output power

5.3 Summary

The Tm^{3+} ($^3F_4$) to Ho^{3+} ($^5I_7$) energy transfer and Tm^{3+} - Tm^{3+} cross- relaxation process as a function of the donor and acceptor concentrations in Tm–Ho co-doped aluminosilicate fibers was studied. Our study shows that the donor-acceptor concentration ratio that ranges from 10:1 to 20:1 and a thulium concentration of ~5wt% has resulted in the maximum laser efficiency for operation in the 2.1 microns wavelength region.

The hybrid gas phase-solution doping technique together with the MCVD process used to fabricate Tm-Ho co-doped fibres allows a more uniform distribution of the interacting rare earth ions across the core region. As a consequence, an efficient two-for-one cross-relaxation process in thulium followed by the energy transfer between thulium and holmium ions was obtained. Laser efficiency exceeding 55% at emission wavelengths of 2.1μm has been reached, demonstrating the possibility of achieving higher laser efficiency from further improvement in the donor acceptor energy transfer process.

Chapter 6 Additional project

6.1 Yb-doped fibres by vapour phase deposition

Ytterbium-doped fibre lasers (YDFL) have shown exponential improvement in the last decade due to the power scaling to multi-kW with direct diode pumping and tandem pumping with a good beam quality[124,125]. Therefore, the effort to improve the host material for the advancement of high power devices has become much more important as the ytterbium-doped fibre lasers suffer from photodarkening, which is a host glass dependant phenomenon.

The photodarkening occurs when the ytterbium-doped fibres are pumped by 915nm or 976nm diodes. This development can happen in minutes or very slowly over many hours, depending on the ytterbium density in the excited level, which then induces excess optical losses in the core of the fibre and a continued decrease in the output power of the fibre lasers. It is often viewed as the formation of colour centres in the presence of intensive resonant irradiation, which causes permanent damage to the doped core as the background loss is increased[126,127]. Hence, a modified preform fabrication process and a new host material are needed to reduce this phenomenon.

The most common approach is to co-dope ytterbium-doped fibres with a phosphosilicate host instead of the aluminosilicate host that is commonly used[128,129]. The phosphosilicate host minimises the photodarkening and also makes it possible to fabricate these fibres by a modified chemical vapour deposition technique in conjunction with the well-established solution doping. However, it is difficult to control the refractive index profile in the fibre due to the phosphorous evaporation within the core during the high temperature stages of the fabrication process, resulting in a central dip within the core refractive index profile that has detrimental effects on the output beam quality of fibre lasers[130,131]. In addition, ytterbium-doped fibres exhibit a lower absorption cross section in a phosphosilicate host as compared to a aluminosilicate host[132]. This can be overcome by using higher ytterbium concentration to attain sufficient pump absorption in double clap fibres without compromising the fibre length. However, this means that a higher content of phosphorous is required to disperse the high level of ytterbium ions within the core in a homogeneous manner, contributing to

a high core NA and posing a challenge to the fabrication of large mode area ytterbium phosphosilicate fibres, reaching the limits of the MCVD and solution doping approach[133,134].

As presented in Chapter 2, the use of chelates in conjunction with the MCVD process might overcome the solution doping limitations as the incorporation of the rare earth and modifier ions takes place simultaneously, allowing higher concentrations of rare earth ions within the fabrication process, an increase in the number of doped layers during the core deposition for large mode area preform structures and a better distribution of the dopants within the core, which thus reduces clustering.

In a similar way as in Chapter 3, an all vapour phase deposition technique is presented. A set of ytterbium-doped fibres in a phosphosilicate host were fabricated in order to explore the capabilities of this approach for low NA fibres and to overcome the solution doping technique limitations for large mode area fibres. In addition, the laser efficiency and beam quality was measured.

6.1.1 Experimental work

The main objective of this collaboration was to fabricate ytterbium-doped fibres in a phosphosilicate host with low NA (~0.1) by an all vapour phase deposition technique. Table 15 shows the glassware used during the fabrication and the required fibre parameters.

Table 15. Glass tube dimensions for fabrication

Type of tube	Suprasil F300 (Heraeus)
Tube outer diameter	20mm
Tube inner diameter	16mm
Cross Sectional Area	113mm^2
Preform clad diameter (expected)	12mm
Fibre clad diameter (required)	150μm
Fibre core diameter (required)	15μm
Fibre clad/core ratio	10
Fibre geometry	Quasi Octagonal

The ytterbium-doped silica preforms were fabricated in an MCVD apparatus and a separate heated vapour phase delivery system, where Yb-tris (2,2,6,6-tetramethyl-3,5-heptanedionato, 99.9%) was placed inside a separate container and heated up between 170˚C to 220˚C to generate vapour pressure. By using helium as carrier gas, the ytterbium-tris was transported to the reaction zone through a dedicated line. The vapour pressure and flows were calculated by using Equation 7 and Graph 3 as reference.

As presented in previous chapters, the process started on high quality silica tubes (F300 from Heraeus) with a nominal 20x16mm diameter and 500mm length. The tubes were cleaned in the MCVD lathe using sulphur hexafluoride (SF_6) followed by a deposition of several SiO_2 layers to reduce the mismatch with the F300 glass. Subsequently, a combination of $POCl_3$ and Yb-tris flow was carried into the reaction zone at a moderate temperature to form a fully sintered transparent layer as shown in Image 23, where the characteristic orange glow from $POCl_3$ reaction is appreciated.

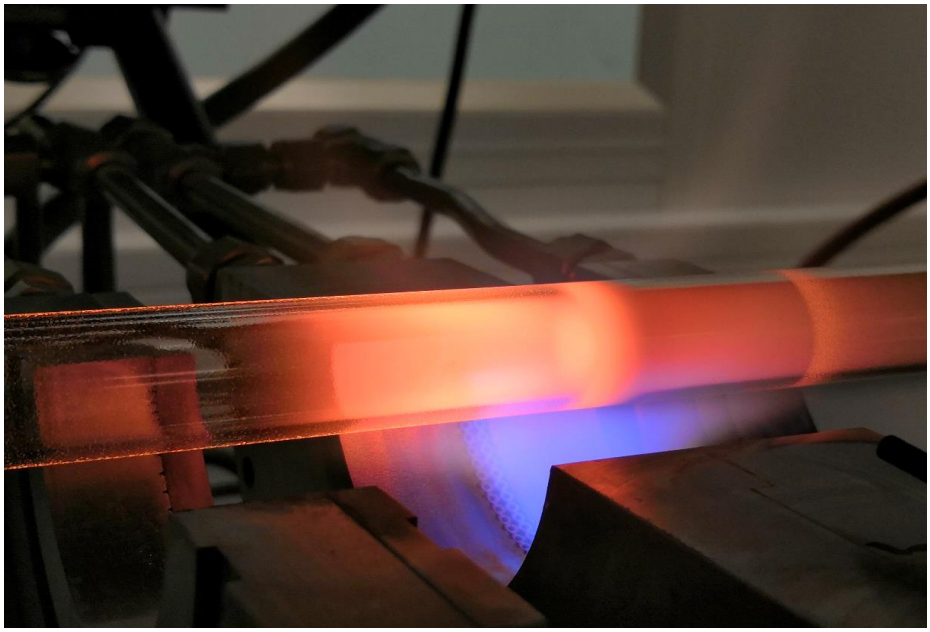

Image 23. Yb tris deposition in phosphosilicate host

Finally, the tubes were collapsed above 2000˚C and converted into solid rods.

6.1.2 Preform characterisation

The refractive index profile from the first preform was analysed with a PK2600. The preform showed a Δn ~0.0035 (NA ~0.1). Also, a central dip within the core was clearly noticed, which indicates that the phosphorous oxide had evaporated during the collapsing stages as shown in Graph 48. Disregarding the central dip, the refractive index profile was consistent along the length of the preform, achieving a maximum length of 200mm. Nevertheless, the preform was dismissed as the large central dip can cause a detrimental effect on the output beam quality of the fibre laser.

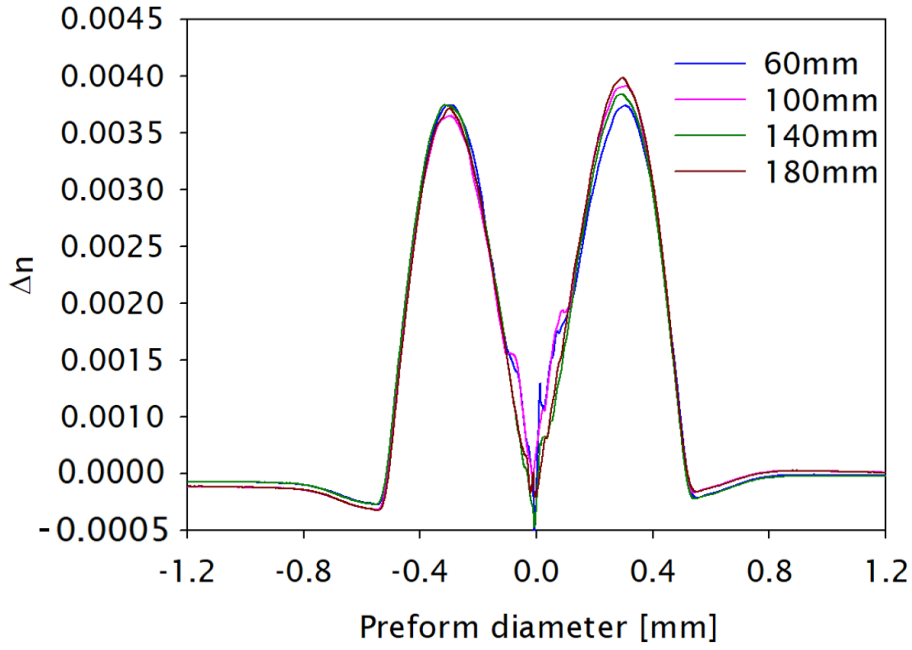

Graph 48. Yb-doped preform RIP with central dip

A second preform was fabricated with the same parameters but with an optimised collapse process to reduce the depth of the central dip within the core. As presented in Graph 49, the preform exhibited the same core size and Δn level with a stability along 350mm of the preform. Moreover, compared to the first fabricated preform, the central dip was reduced considerably which benefitted the output beam propagation.

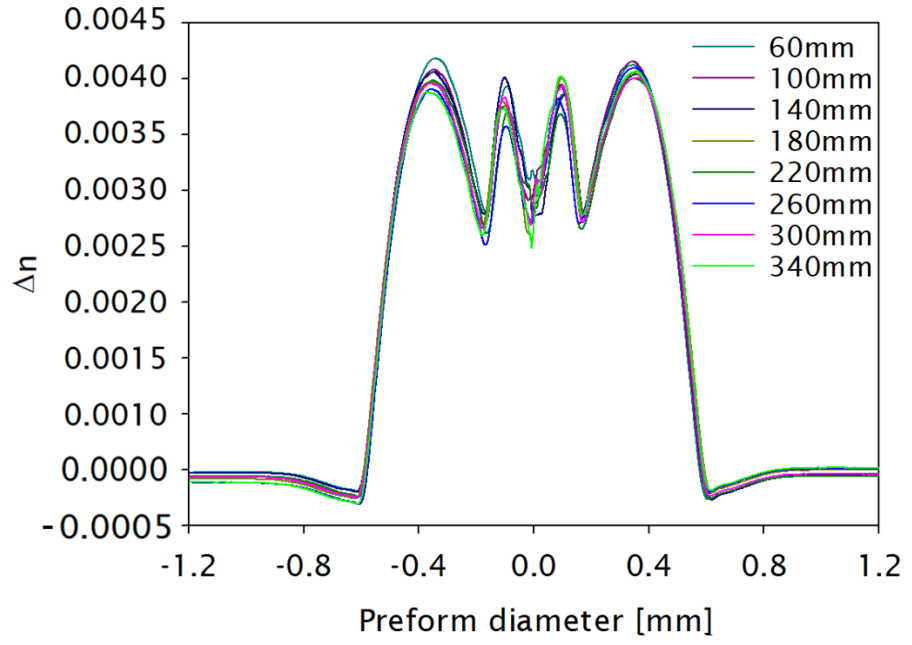

Graph 49. Optimised Yb-doped preform with reduced central dip

Subsequently, the preform was put through a series of stretching and sleeving processes to modify the clad/core ratio and to a milling process to remove glass

from the preform and modify the geometry of the circular surface. Finally, the preform was drawn into a 150µm/12µm diameter fibre and coated with low index polymer. By using an IFA-100, a two-dimensional refractive index profile from the resultant ytterbium-doped fibre was taken and presented in Figure 25. Yb-doped two-dimensional fibre refractive index profile~~Figure 25. Yb-doped two-dimensional fibre refractive index profile~~.

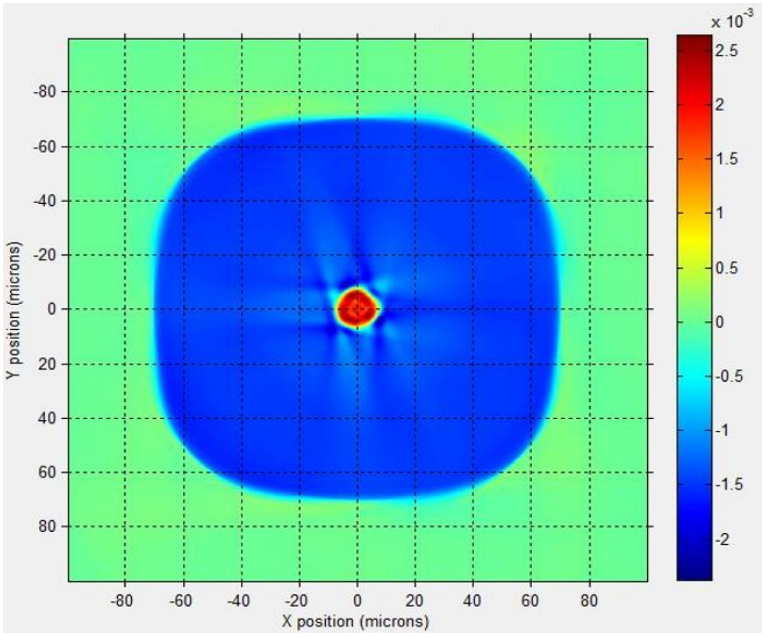

Figure 25. Yb-doped two-dimensional fibre refractive index profile

6.1.3 Fibre characterisation

The optical absorption of the fibre was obtained by using a white light source and an optical spectrum analyser. The absorption was evaluated at ~976nm and the Yb^{3+} concentration was estimated as explained in Chapter 4. Graph 50 shows the absorption spectrum of the fibre, making clear the characteristic curve for Yb-doped fibres in a phosphosilicate host (915nm flatten section).

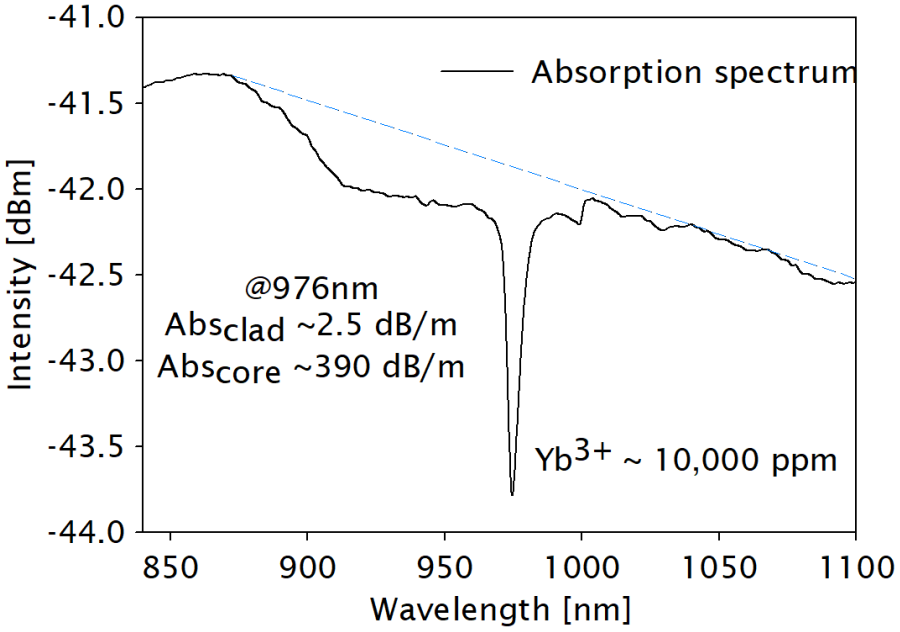

Graph 50. Yb-doped fibre absorption spectrum (centred at 976nm)

The laser performance was measured in a 4% – 4% laser cavity configuration. The fibre was cladding pumped by a ~976nm fibre coupled multimode laser diode through a combination of collimating lenses. The setup used for this test was as described in Figure 23, with the difference that no water-cooled base was used.

The Yb-doped fibre exhibited an output power >100W (limited by the available pump power) and a laser efficiency with respect to the absorbed pump power ~85%. The slope efficiency and the laser emission wavelength centered at 1066nm are presented in Graph 51 and Graph 52, respectively.

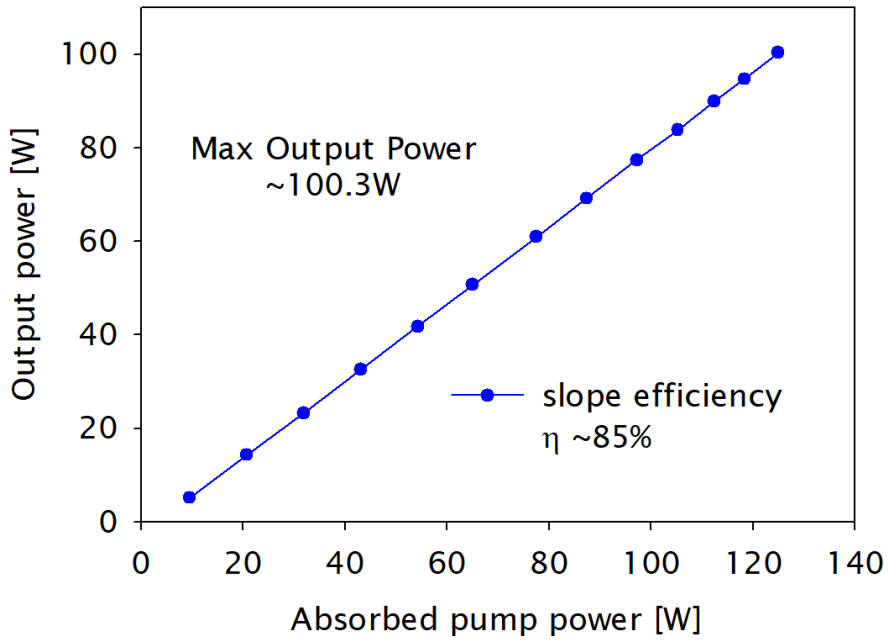

Graph 51. Yb-doped fibre slope efficiency

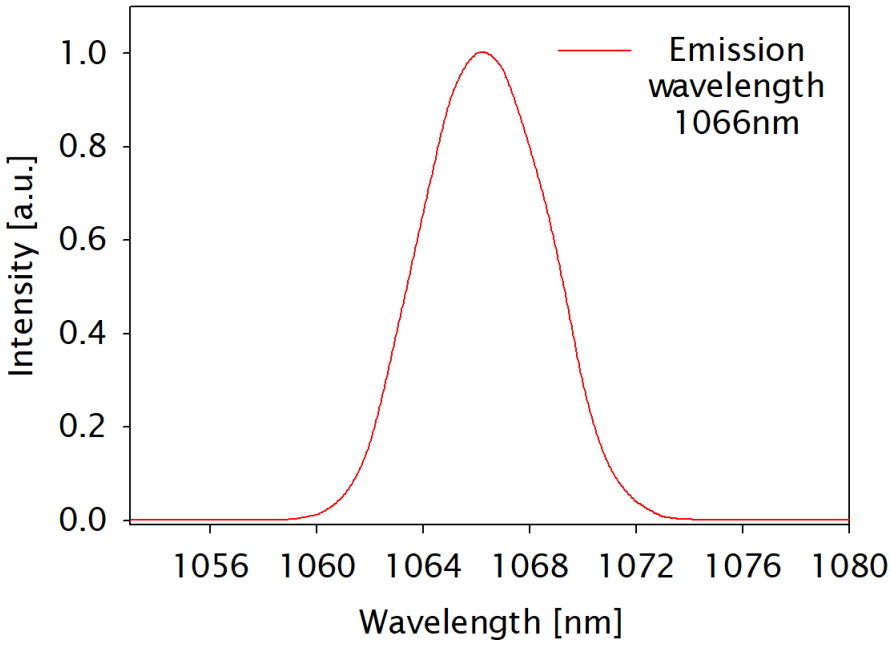

Graph 52. Yb-doped fibre emission wavelength

Additionally, an M2 measurement was performed by Dr. Di Lin, resulting in a beam quality of ~1.13 as presented in Graph 53.

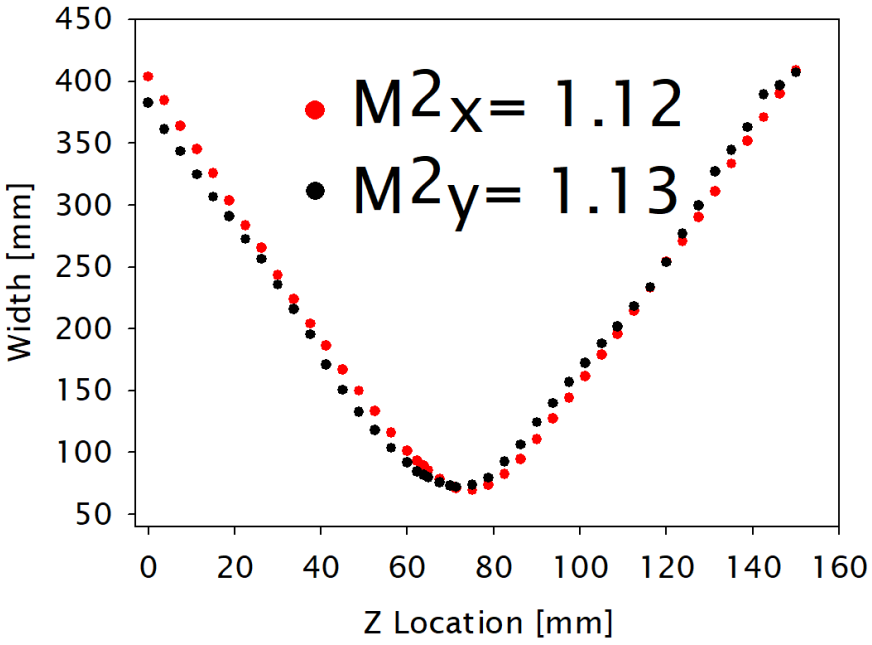

Graph 53. Yb-doped fibre M^2 approximation

6.1.4 Additional fabrication

The advantage of having an integrated system which covers the vapour deposition of conventional compounds ($SiCl_4$, $POCl_3$, $GeCl_4$) and rare earths (Yb-tris, Er-tris) is that it enables the possibility of fabricating large mode area preforms by just increasing the number of deposited layers and without the necessity of removing

the tube from the lathe, as is normally done with the multiple solution doping. Moreover, as the dopants are integrated to the reaction zone simultaneously, there is better control over the refractive index and a better distribution of the dopants within the core.

The preform was fabricated using the same glassware characteristics as the previous one and the number of deposited layer was adjusted to have a core preform diameter between 3mm and 4mm. Following the deposition, the tube was collapsed and sealed in the normal manner. A core diameter of ~3.6mm during the collapse and sealing stage can be seen in Image 24.

Image 24. LMA Yb-doped preform during collapse stage

The refractive index profile was analysed with a PK2600 resulting in a Δn ~0.0035 (NA ~0.1) and a Δn level with a stability along 280mm of the preform as shown in Graph 54.

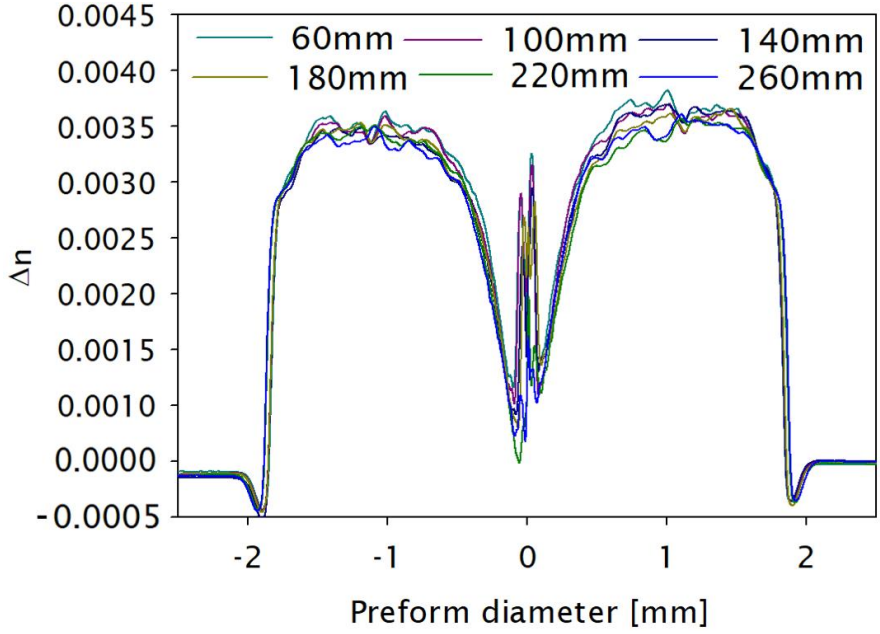

Graph 54. LMA Yb-doped preform RIP

Unfortunately, due to circumstances outside the control of the University of Southampton and the author's PhD studies (COVID-19), no further analysis was made to the preform, holding all activities in standby.

6.2 Summary

Ytterbium doped fibre lasers have reached continuous wave output powers in the kW level and have become the laser of choice for many industrial applications. One of the challenges of using high average power fibre laser is maintaining a long-term stability of the output power as it has been seen that photodarkening reduces the output power in ytterbium-doped fibres, reducing the operation lifetime of the devices.

Silica hosts that are co-dopant with phosphorous have shown more effectiveness than aluminium to suppress the photodarkening effect in YDF. However, ytterbium-doped in phosphosilicate host are generally considered difficult to fabricate due to evaporation of P_2O_5 during the preform fabrication process, resulting in a central dip in the core refractive index profile that has detrimental effects on the output beam quality of the fibre lasers.

In addition, in order to overcome the limited absorption cross section of phosphosilicate host, higher ytterbium concentrations are needed and therefore, higher concentration of P_2O_5. However, the MCVD process with conventional solution doping has reached its limit for the new required designs.

It has been seen that the use of chelates in conjunction with the MCVD process might overcome the solution doping limitations as the incorporation of the rare earth and modifier compounds takes place simultaneously, allowing higher concentrations of rare earth ions within the fabrication process. Moreover, in order to increase the core size for large mode area preforms, it is possible to increase the number of doped layers during the core deposition without additional steps.

So far, an efficient ytterbium doped fibre in phosphosilicate host fabricated with an optimized MCVD process and all-vapour phase deposition technique has been demonstrated, which shows the great potential of fabricating LMA Yb-doped phosphosilicate fibres for high power lasers.

Chapter 7 Overall conclusions

A hybrid fabrication technique for thulium-doped aluminosilicate fibres has been developed by combining an all vapour phase deposition technique for enhancing high aluminium content and the solution doping process for the incorporation of high purity rare earth halide precursor in conjunction with the well-known MCVD technique. The addition of >8mol% of Al_2O_3 to the silica glass in a controlled manner through a vapour phase deposition method has exhibited a characteristic flat-top refractive index profile and a better dispersion of the dopants within the core, which is suitable for high power fibre laser applications. Moreover, this hybrid approach has enabled a more stable fabrication process with a homogeneous refractive index profile along the length of the preform of >400mm which has a strong impact for the optical fibre fabrication industry.

7.1 Thulium-doped fibres

A direct comparison between the hybrid gas phase solution doping technique and the conventional solution doping method has been presented. The noticeable improvement on the thulium ions distribution in the core glass allowed an increment of 30% in the $^3F_4$ manifold lifetime from ~385µm to ~525µm. Moreover, it also ensured ~12% more of the doped region within the core to take part in the cross relaxation process.

The laser properties of thulium-doped fibres have been demonstrated by reaching superior laser performance in the two-micron band. It is noteworthy that the emission wavelength can be selected anywhere in a range from 1980nm to 2080nm with slope efficiencies >70%, which is evidence that the two-for-one cross-relaxation process can be achieved close to its full capability (>90% of quantum efficiency) without the necessity of a very high thulium concentration.

The potential of the hybrid gas phase solution doping technique for the fabrication of highly efficient thulium-doped fibres has shown that the technique can be easily adaptable to manufacturing environments. Moreover, the proposed technology makes it possible to fabricate a large-mode-area thulium-doped fibre with a pedestal design comprised of aluminosilicate layers surrounding the core, which are deposited via the all vapour phase deposition process. Such pedestal layers significantly reduce the thermal mismatch with the silica cladding, offering much

greater flexibility when there is a need for depositing a large pedestal and fabrication of a polarization-maintained fibre in a pedestal geometry.

7.2 Thulium:holmium co-doped fibres

Thulium-holmium co-doped fibres in contrast to holmium-doped fibres enjoy the benefit of the two-for-one cross-relaxation and can be pumped by ~790nm high power diodes. By using a co-doped system, it is possible to extend the emission characteristics to the 2.1μm band without the necessity of complex fibre structures or in-band pumping schemes.

The positive results coming from the spectroscopic measurements of the Tm:Ho co-doped system in aluminosilicate glass identified an efficient energy transfer process with moderate Tm^{3+} concentrations by balancing the trade-off between ions in the $^3F_4$ and $^5I_7$ manifold from thulium and holmium, respectively. However, careful manipulation of the dopant concentration ratio is required to maximize the two-for-one cross relaxation in thulium and the donor-acceptor energy transfer efficiency.

Our study indicates that for a thulium concentration that has resulted in an efficient two-for-one cross relaxation process with 790nm pumping and that maintained a Tm:Ho concentration ratio in the range ~ 10 to 20, the energy transfer efficiency can be reached above 75%. In a free-running laser cavity, lasing at 2105nm with a slope efficiency of 56% and >38W output power was demonstrated.

Substantial progress has been made in the development of thulium and thulium:holmium co-doped fibres for high power fibre laser applications. Moreover, the results presented in this thesis have shown that the fabrication technology can be directly transferred to the optical fibre fabrication industry with huge potential for further power scaling.

Chapter 8 Future work

Future work and areas of improvement identified during the realisation of this thesis are presented below. So far, the capability of using an all vapour phase deposition technique and the solution doping method in conjunction with the MCVD process has been demonstrated.

As mentioned in Chapter 1, the utilisation of thulium-doped fibre lasers for medical applications have shown potential advantages since the TDFLs can emit laser radiation at two primary wavelengths, 1908nm or 1940 nm, which closely match the high and low temperature water coefficient absorption peaks in tissue. However, for applications with emission wavelengths below 2000nm, the design of the fibres requires deeper study of how to maintain high thulium concentrations (>3.5wt%) in the core for efficient lasing at ~1950±20nm as well as how to optimize the length of the fibre and the core size for the single mode operation.

Therefore, the NA must be decreased from the actual fibres from 0.23±3 to approximately 0.10 so that the core diameter can be increased, allowing the power scaling that cannot be possible in small cores. The immediate approaches that can be followed are the use of a pedestal structure and/or the incorporation of thulium by an all vapour phase deposition technique.

The first approach is to produce a raised index cladding with tens of aluminosilicate layers that can be deposited on the silica substrate tube before the core deposition. With this pedestal structure, the core is exposed to a local low index step, producing a low NA whilst the core material is not altered at all. Additionally, pedestal refractive index profile fibres based on aluminosilicate host glass for tm-doped fibres can tolerate the post processing of the glass. However, the small tolerance in the index difference between core and cladding makes the process particularly critical.

Fabrication of large core thulium-doped fibres with an improved fabrication technique such as the hybrid gas phase solution doping allows the flexibility to use specific core compositions with high purity precursors as well as reproducibility, reducing the fabrication cost for the optical fibre fabrication industry.

The second approach is the use of an all vapour phase deposition technique to incorporate thulium and aluminium. Based on the results of this thesis, the implementation of aluminium by an all vapour phase deposition technique resulted

in high aluminium oxide concentrations and better dispersion of the dopants, which allowed to reduce the Tm concentration in the range of ~4wt%, and producing laser efficiencies of ~70%. Therefore, combining both dopants in an all vapour phase deposition technique not only optimized the distribution of the dopants within the core but also allowed the reduction of the thulium concentration.

Compared to rare earth chlorides, the lanthanide chelates can be sublimated directly from solid-state (~170˚C), thanks to the organic ligand, and decomposed directly in the reaction zone inside the silica tube. However, the use of an all vapour phase deposition technique requires an extensive study on the precursor's decomposition mechanism as well as the optimization of deposition conditions when rare earth concentration exceeds 2wt%.

The use of the all vapour phase technology will allow the simultaneous incorporation of a variety of dopants and larger cores without the necessity of additional processes, a better control of the refractive index along the length of the preform and faster processing time, which reduce the production cost.

In addition to the thulium-doped fibre development, the Tm:Ho co-doped system requires further study. It has been noted that with a large population density in the $^3F_4$ manifold from thulium and the right concentration ratio of the dopants, the energy transfer efficiency increased. However, exploring the effects on the aluminosilicate fibres when the Ho^{3+} concentration is increased was not explored and the fibres were also not exposed to higher pump power levels >150W to see if there are any detrimental effects.

Finally, due to circumstance external to the University of Southampton and the author's PhD studies (COVID-19), some experiments and/or tests could not be performed, such as the absorption and emission cross-section measurements and processing and measurements of the beam quality with a 2μm set-up.

Appendix A Fabrication Summary

A.1 Aluminium-doped fibres

Table 16. Aluminium-doped fabrications

Fibre/ Preform	Fabrication technique	Core/Clad [µm]	Geometry	Δn
Al-01	VP	15/125	Circular	0.011
Al-02	VP	18/125	Circular	0.014
Al-03	VP	15/125	Circular	0.007
Al-04	VP	25/200	Circular	0.014
Al-05	HGSD	15/125	Circular	0.017
Al-06	HGSD	25/200	Circular	0.016
Al-07	VP	15/125	Circular	0.018
Al-08	VP	15/125	Circular	0.016
Al-09	VP	15/125	Circular	0.020
Al-10	VP	15/125	Circular	0.023
Al-11	HGSD	15/125	Circular	0.015
Al-12	VP	15/125	Circular	0.012
Al-13	VP	N/A	N/A	0.008
Al-14	VP	N/A	N/A	0.006
Al-15	VP	N/A	N/A	0.009
Al-16	VP	N/A	N/A	0.009
Al-17	VP	N/A	N/A	0.012

A.2 Thulium-doped fibres

Table 17. Thulium-doped fabrications

Fibre/ Preform	Core Composition	Fabrication technique	Core/Clad [µm]	Geometry	Δn
Tm-01	Tm^{3+}, Al, Si	HGSD	16/125	Circular	0.011
Tm-02	Tm^{3+}, Al, Si	HGSD	16/125	Circular	0.013
Tm-03	Tm^{3+}, Al, Si	HGSD	16/125	Circular	0.026
Tm-04	Tm^{3+}, Al, Si	HGSD	16/125	Circular	0.017
Tm-05	Tm^{3+}, Al, Si	HGSD	16/125	Circular	0.018
Tm-06	Tm^{3+}, Al, Si	HGSD	16/125	Circular	0.019
Tm-07	Tm^{3+}, Al, Si	HGSD	8/200	Quasi_Oct	0.026
Tm-08	Tm^{3+}, Al, Si	HGSD	8/200	Quasi_Oct	0.017
Tm-09	Tm^{3+}, Al, Si	HGSD	8/200	Quasi_Oct	0.018
Tm-10	Tm^{3+}, Al, Si	HGSD	8/200	Quasi_Oct	0.019
Tm-11	Tm^{3+}, Al, Si	SD	8/200	Oct	0.020
Tm-12	Tm^{3+}, Al, Si	HGSD	8/200	Quasi_Oct	0.025
Tm-13	Tm^{3+}, Al, Si	HGSD	8/200	Quasi_Oct	0.027
Tm-14	Tm^{3+}, Al, Si	HGSD	8/200	Quasi_Oct	0.020
Tm-15	Tm^{3+}, Al, Si	HGSD	N/A	N/A	0.030
Tm-16	Tm^{3+}, Al, Si	HGSD	N/A	N/A	0.030

A.3 Thulium:Holmium co-doped fibres

Table 18. Tm:Ho co-doped fabrications

Fibre	Core Composition	Fabrication technique	Core/Clad [μm]	Geometry	Δn
TH-01	Tm^{3+}, Ho^{3+}, Al, Si	HGSD	8/200	Quasi_Oct	0.023
TH-02	Tm^{3+}, Ho^{3+}, Al, Si	HGSD	8/200	Quasi_Oct	0.022
TH-03	Tm^{3+}, Ho^{3+}, Al, Si	HGSD	8/200	Quasi_Oct	0.023
TH-04	Tm^{3+}, Ho^{3+}, Al, Si	HGSD	8/200	Quasi_Oct	0.027
TH-05	Tm^{3+}, Ho^{3+}, Al, Si	HGSD	8/200	Quasi_Oct	0.027
TH-06	Tm^{3+}, Ho^{3+}, Al, Si	HGSD	8/200	Quasi_Oct	0.017
TH-07	Tm^{3+}, Ho^{3+}, Al, Si	HGSD	8/200	Quasi_Oct	0.020
TH-08	Tm^{3+}, Ho^{3+}, Al, Si	HGSD	8/200	Quasi_Oct	0.020
TH-09	Tm^{3+}, Ho^{3+}, Al, Si	HGSD	8/200	Quasi_Oct	0.020

Appendix B Laser efficiency Set Up

B.1 Preliminary test

The laser performance was measured in a 4% – 4% laser cavity configuration. The fibre was cladding pumped by a 790nm fibre coupled multimode laser diode through a combination of collimating lenses. Dichroic mirrors were used to separate the pump from signal wavelengths at both pump launches and pumped throughout the ends of the fibre. The slope efficiency was calculated with the total output power from both ends of the fibre.

The first attempt to measure the laser efficiency was done on a circular version of the HGSD-03 fibre with a core/cladding diameter of ~16/125μm. The fibre was placed on an air-cooled arrangement to dissipate the heat produced by the fibre and twisted to force the mode mixing as shown in Image 25.

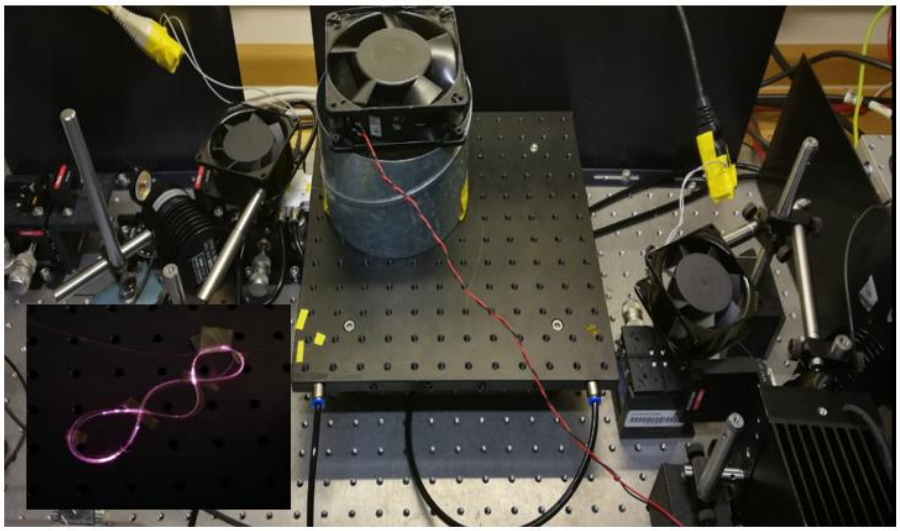

Image 25. Laser efficiency set-up Version I

However, the small signal absorption was inefficient, leading to very low laser efficiencies as can be seen in Graph 55.

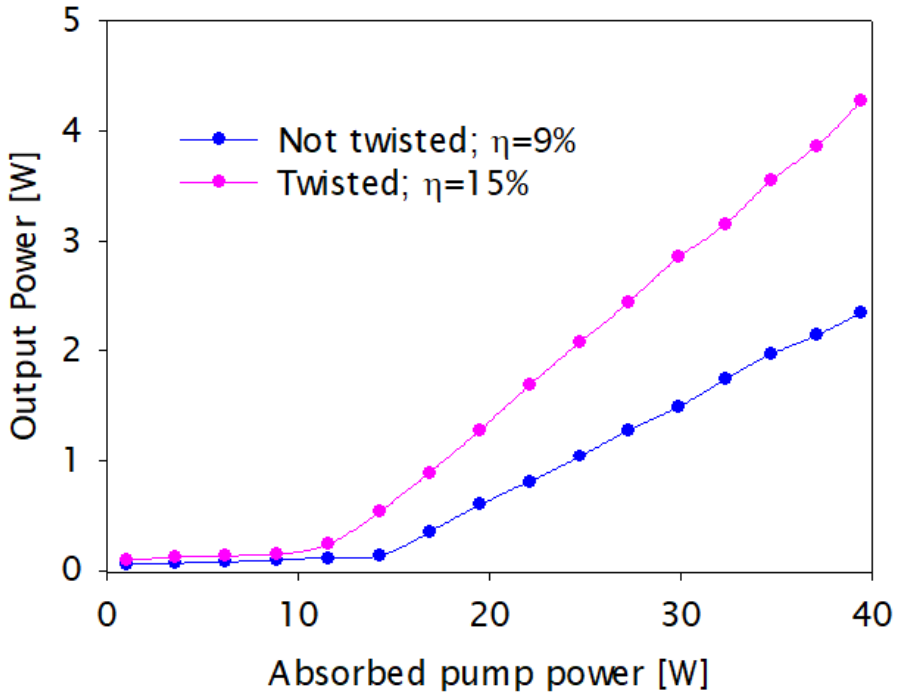

Graph 55. Laser efficiency of circular version HGSD-03

B.2 Auxiliary fibre test

Consequently, as the circular version of the HGSD-03 fibre was not promising, it was decided to test a fibre previously reported by the Optoelectronics Research Centre with a slope efficiency of ~68%. The fibre with a core/cladding diameter of ~19/200μm and a circumscribed D-shaped was placed on an aluminium plate with a ~15cm coiled as shown in Image 26.

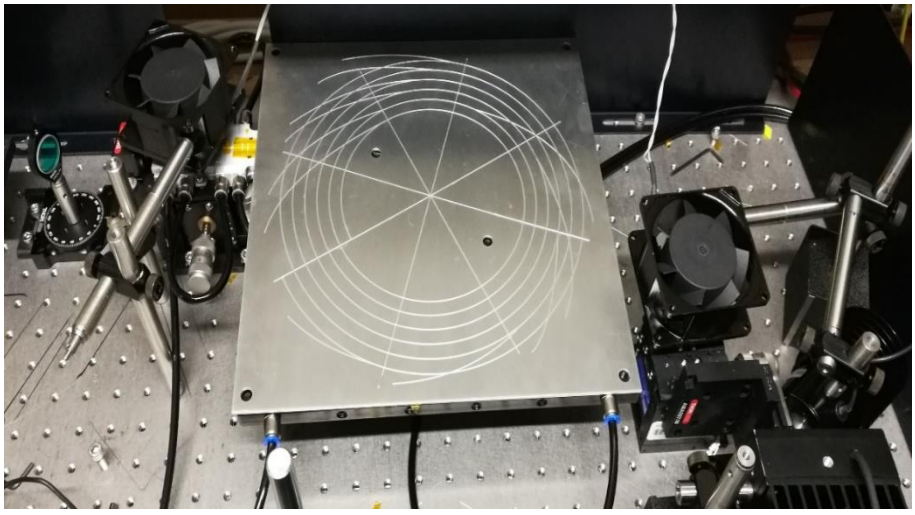

Image 26. Laser efficiency set-up Version II

Additional to the air-cooled arrangement, the fibre was placed on a water-cooled plate where the temperature was varied during the laser efficiency measurements as shown in Graph 56.

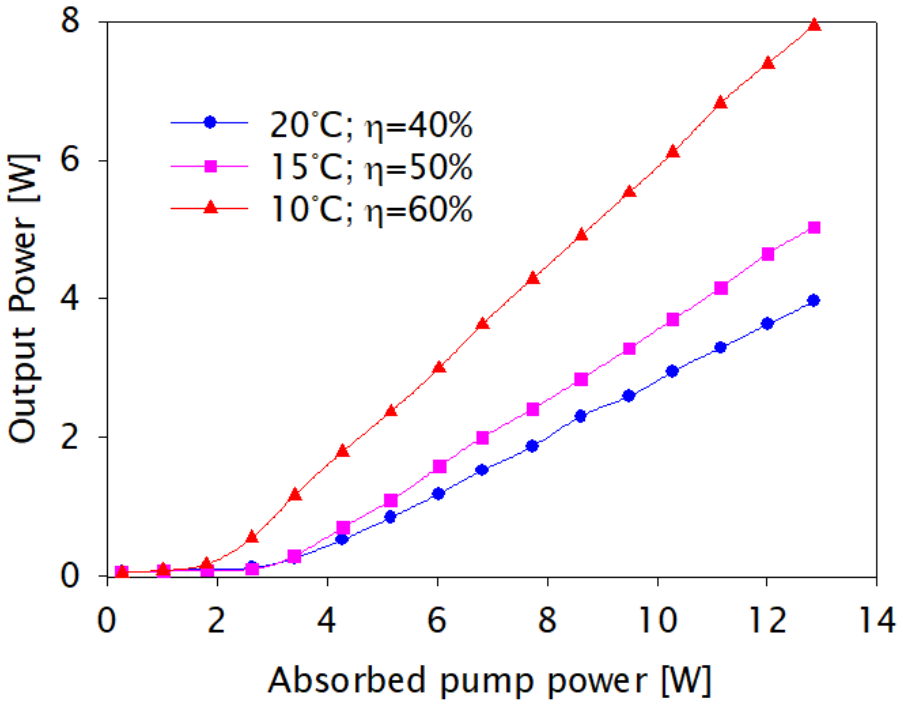

Graph 56. Laser efficiency of auxiliary fibre (D-shape)

B.3 Final set-up test

Another section from the HGSD-03 preform was post-processed to modify its core to cladding ratio to ~25 for heat management purposes. Then, a quasi-octagonal shape was circumscribed in the preform by using ultrasonic milling for breaking the geometry and enhancing the cladding pump absorption. The preform was drawn into 200μm diameter fibre in a double clad configuration.

Finally, all the air-cooled arrangements and the aluminium plates were removed. The laser efficiency set-up was optimised by placing the fibre on water-cooled base with circulating water at approximately 10°C. Image 27 shows the laser efficiency set-up used during all the laser measurements presented in this thesis.

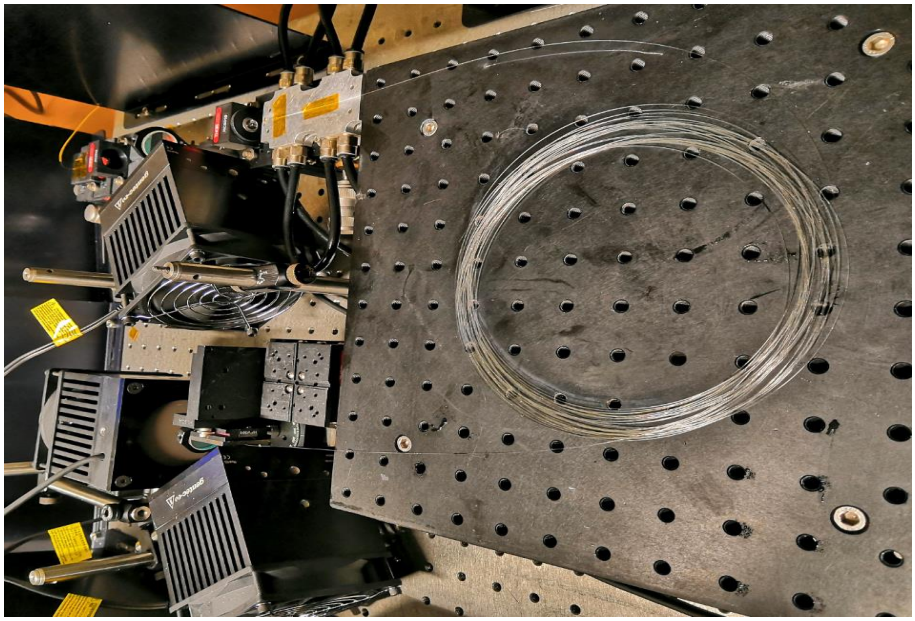

Image 27. Final laser efficiency set-up Version III

Appendix C Activity record

C.1 Activity record during PhD

The following tables provide a summary of all work undertaken and highlight the key activities during the PhD studies.

Table 19. 2016 - 2017

Activities	**Start of PhD studies**
	Complementary lectures: lasers and optical technologies
	ORC photonics lectures: season 1
	ORC photonics lectures: season 2
	Ge-doped fibres fabrication (supervised)
	Characterisation of pre-exiting Tm-doped fibres
	8th months report (examination)
Training	Endnote
	Introduction to teaching skills for PGRS (demonstrators)
	Presenting my research
	Technical writing skill
	Silica cleanroom training
	Use of MCVD (Heathway)
	Use of MCVD (SG)
	Use of Vapour Phase Deposition system
	Laser safety
	High power lasers (<50W)

Table 20. 2017 - 2018

Activities	Oral presentation at Mexican symposium (Durham)
	Ge-doped fibres fabrication (supervised)
	P-doped fibres fabrication (supervised)
	Al-doped fibres fabrication (supervised)
	Characterisation of FBGs under high power (external project)
	Tm-doped fibres fabrication by Hybrid technique (supervised)
	Post processes for Tm-doped fibres (supervised)
	Characterisation of Tm-doped fibres
	Analysis of Tm-doped fibres (1st batch)
	Oral presentation at CLEO USA 2018
	16th months VIVA and upgrade report
Training	Use of MCVD lathe (Heathway)
	Use of MCVD lathe (SG)
	Use of Vapour Phase Deposition system
	Glass working (preform post process)
	Ultrasonic milling
	Drawing tower (SG)

Table 21. 2018 - 2019

Activities	**Oral presentation at Advanced Photonic Congress 2018**
	Technical chair at Mexican symposium (Southampton)
	Tm-doped fibres fabrication by Hybrid technique
	Post processes for Tm-doped fibres
	Characterisation of Tm-doped fibres
	Analysis of Tm-doped fibres (2nd batch)
	1st journal paper at Optics Express (published)
	Characterisation of Yb-doped fibres
	Er-doped fibres fabrication by Hybrid technique (external project)
	P-doped fibres fabrication (external project)
Training	High power lasers (>100W)

Table 22. 2019 - 2020

Activities	Oral presentation at European Parliament (Strasbourg)
	Tm/Ho-doped fibres fabrication by Hybrid technique
	Post processes for Tm/Ho-doped fibres
	Characterisation of Tm/Ho-doped fibres
	Analysis of Tm/Ho-doped fibres
	Oral presentation at CLEO Europe 2019
	Ge-doped fibres fabrication (external project)
	Yb-doped fibres fabrication by Vapour phase deposition (external project)
	Yb-doped fibres characterisation (external project)
	Er-doped fibres fabrication by Vapour phase deposition (external project)
	Er-doped fibres characterisation (external project)
	Oral presentation at Photonic West 2020
	2nd journal paper at Optics Express (published)
	COVID-19 (lockdown)
	"Intention to submit"
	Thesis submission
	PhD VIVA examination

Appendix D Publications

D.1 List of publications

2020

- N. J. Ramírez-Martínez, M. Núñez-Velázquez and J. K. Sahu, "Study on the dopant concentration ratio in thulium-holmium doped silica fibers for lasing at 2.1μm," Opt. Express28, 24961-24967 (2020).
- M. Núñez-Velázquez, N. J. Ramírez-Martínez and J. K. Sahu, " Development of Tm:Ho Co-doped Silica Fiber for High-power Operation at 2.1μm," in Conference on Lasers and Electro-Optics, OSA Technical Digest (Optical Society of America, 2020), paper STh4P.7.
- Norberto J. Ramírez Martínez, Martín M. A. Núñez Velázquez, Jayanta K. Sahu, "Efficient cladding pump Tm:Ho co-doped fiber laser for operation in the 2.1 microns region," Proc. SPIE 11260, Fiber Lasers XVII: Technology and Systems, 112600H (21 February 2020.

2019

- N. J. Ramírez-Martínez, M. Núñez-Velázquez, and J. K. Sahu, "790nm Diode Pumped Thulium Sensitized Holmium-doped Fibre Laser Operating Beyond 2100nm," in 2019 Conference on Lasers and Electro-Optics Europe and European Quantum Electronics Conference, OSA Technical Digest (Optical Society of America, 2019), paper cj_8_5.
- J. K. Sahu, D. Lin, N. J. Ramírez-Martínez, A. A. Umnikov, M. Núñez-Velázquez, and P. Barua, "Pulsed Yb-doped Phospho-silicate Fiber MOPA Source with 25kW Peak Power and Excellent Beam Quality," in 2019 Conference on Lasers and Electro-Optics Europe and European Quantum Electronics Conference, OSA Technical Digest (Optical Society of America, 2019), paper cj_p_24.
- N. J. Ramírez-Martínez, M. Núñez-Velázquez, A. A. Umnikov, and J. K. Sahu, "Highly efficient thulium-doped high-power laser fibers fabricated by MCVD," Opt. Express 27, 196-201 (2019).

2018

- N. J. Ramírez-Martínez, M. Núñez-Velázquez, A. A. Umnikov, and J. K. Sahu, "Efficient Thulium-doped Fiber Laser Operating in the 1890 – 2080nm Wavelength Band," in Advanced Photonics Congress, OSA Technical Digest (Optical Society of America, 2018), paper SoTu4H.3.
- Halder, Di. Lin, A. A. Umnikov, N.J. Ramirez- Martinez, M. Nunez-Velazquez, P. Barua, S. Alam and J.K. Sahu, "Picosecond Yb-doped alumino-phospho-silicate fiber MOPA with >35kW peak power," in Advanced Photonics Congress, OSA Technical Digest (Optical Society of America, 2018), paper Tu3A.5.
- N. J. Ramírez-Martínez, M. Núñez-Velázquez, A. A. Umnikov, and J. K. Sahu, "Novel Fabrication Technique for Highly Efficient Tm-doped Fibers," in Conference on Lasers and Electro-Optics, OSA Technical Digest (Optical Society of America, 2018), paper SF3I.2.
- Halder, Di. Lin, A. A. Umnikov, N.J. Ramirez- Martinez, M. Nunez-Velazquez, P. Barua, S. Alam and J.K. Sahu , "Yb-doped Large-Mode-Area Al-P-Silicate Laser Fiber fabricated by MCVD," in Conference on Lasers and Electro-Optics, OSA Technical Digest (Optical Society of America, 2018), paper JTh2A.77.

List of References

1 Dong, L. Advanced Optical Fibers for High Power Fiber Lasers. doi:10.5772/58958 (2015).

2 Hemming, A., Simakov, N., Haub, J. & Carter, A. in *Workshop on Specialty Optical Fibers and Their Applications.* WT1A.3 (Optical Society of America).

3 Khamis, M. A. & Ennser, K. Theoretical Model of a Thulium-Doped Fiber Amplifier Pumped at 1570 nm and 793 nm in the Presence of Cross Relaxation. *Journal of Lightwave Technology* **34**, 5675-5681, doi:10.1109/jlt.2016.2631635 (2016).

4 Li, Z. *et al.* Thulium-doped fiber amplifier for optical communications at 2 μm. *Opt. Express* **21**, 9289-9297, doi:10.1364/OE.21.009289 (2013).

5 Frith, G., Carter, A. L. G., Samson, B. & Town, G. Design considerations for short-wavelength operation of 790 nm pumped Tm doped fibres. *Appl Opt* **48** (2009).

6 Jackson, S. D. & Mossman, S. Efficiency dependence on the Tm3+ and Al3+ concentrations for Tm3+-doped silica double-clad fiber lasers. *Appl Opt* **42**, 2702-2707 (2003).

7 Shardlow, P. C., Jain, D., Parker, R., Sahu, J. & Clarkson, W. A. in *2015 European Conference on Lasers and Electro-Optics - European Quantum Electronics Conference.* CJ_14_13 (Optical Society of America).

8 Jackson, S. D. & Terence, A. K. High-power diode-cladding-pumped Tm-doped silica fiber laser. *Opt Lett* **23** (1998).

9 Kurkov, A. S., Dvoyrin, V. V. & Marakulin, A. V. All-fiber 10 W holmium lasers pumped at λ=1.15 μm. *Opt. Lett.* **35**, 490-492, doi:10.1364/OL.35.000490 (2010).

10 Pal, D., Dhar, A., Sen, R. & Pal, A. in *13th International Conference on Fiber Optics and Photonics.* Tu3E.2 (Optical Society of America).

11 Simakov, N., Hemming, A., Clarkson, W. A., Haub, J. & Carter, A. A cladding-pumped, tunable holmium doped fiber laser. *Opt. Express* **21**, 28415-28422, doi:10.1364/OE.21.028415 (2013).

12 Holmen, L. G. *et al.* Tunable holmium-doped fiber laser with multiwatt operation from 2025 nm to 2200 nm. *Opt. Lett.* **44**, 4131-4134, doi:10.1364/OL.44.004131 (2019).

13 Kim, J. W., Boyland, A., Sahu, J. K. & Clarkson, W. A. in *CLEO/Europe and EQEC 2009 Conference Digest.* CJ6_5 (Optical Society of America).

14 Hemming, A. *et al.* An Efficient, High Power, Monolithic, Single Mode Thulium Fibre Laser. *Workshop on Specialty Optical Fibers and their Applications* (2013).

15 Simakov, N., Hemming, A., Clarkson, W. A., Haub, J. & Carter, A. A cladding-pumped, tunable holmium doped fiber laser. *Opt Express* **21**, 28415-28422, doi:10.1364/OE.21.028415 (2013).

16 Jackson, S. D., Sabella, A., Hemming, A., Bennetts, S. & Lancaster, D. G. High-power 83 W holmium-doped silica fiber laser operating with high beam quality. *Opt. Lett.* **32**, 241-243, doi:10.1364/OL.32.000241 (2007).

17 Kochanowicz, M. *et al.* Tm3+/Ho3+ co-doped germanate glass and double-clad optical fiber for broadband emission and lasing above 2 µm. *Opt. Mater. Express* **9**, 1450-1458, doi:10.1364/OME.9.001450 (2019).

18 DiGiovanni, D. J. Fabrication of Rare Earth Doped Optical Fiber. *SPIE Fiber Laser Sources and Amplifiers* **1373** (1990).

19 Suzanne, R., Nagel, J. B. & Kenneth, L. W. An Overview of the MCVD process and performance. *IEEE Transactions on Microwave Theory and Techniques* **MMT-30** (1982).

20 Poole, S. B., Payne, D. N., Mears, R. J., Fermann, M. E. & Laming, R. I. Fabrication and Characterization of Low Loss Optical Fibers Containing Rare Earth Ions. *Journal of Lightwave Technology* **LT-4** (1986).

21 Townsend, J. R., Poole, S. B. & Payne, D. N. Solution Doping Technique for Fabrication of Rare Earth Dope Optical Fibres. *Electronics Letters* **23** (1987).

22 Christensen, S., Frith, G. & Samson, B. in *LEOS 2008 - 21st Annual Meeting of the IEEE Lasers and Electro-Optics Society.* 728-729.

23 Heidt, A. M. *et al.* 100 kW peak power picosecond thulium-doped fiber amplifier system seeded by a gain-switched diode laser at 2 μm. *Opt. Lett.* **38**, 1615-1617, doi:10.1364/OL.38.001615 (2013).

24 Ehrenreich, T. *et al.* in *Fiber Lasers III: Technology, Systems, and Applications.* 7580-7112 (SPIE).

25 Jackson, S. D. & Lauto, A. Diode-pumped fiber lasers: a new clinical tool? *Lasers Surg Med* **30**, 184-190 (2002).

26 Yu, J., Singh, U. N., Barnes, J. C., Barnes, N. P. & Petros, M. in *Second International Asia-Pacific Symposium on Remote Sensing of the Atmosphere, Environment, and Space.* 8 (SPIE).

27 Xiaonong, Z. & Shibin, J. 2 Micron Fiber Laser Enable Versatile Processing of Plastics. *Industrial Laser Solutions*, 17-23 (2016).

28 Fried, N. M. Recent advances in infrared laser lithotripsy [Invited]. *Biomed. Opt. Express* **9**, 4552-4568, doi:10.1364/BOE.9.004552 (2018).

29 Traxer, O. & Keller, E. X. Thulium fiber laser: the new player for kidney stone treatment? A comparison with Holmium:YAG laser. *World journal of urology*, doi:10.1007/s00345-019-02654-5 (2019).

30 Aboumarzouk, O. M., Somani, B. K. & Monga, M. Flexible ureteroscopy and holmium:YAG laser lithotripsy for stone disease in patients with bleeding diathesis: a systematic review of the literature. *International braz j urol : official journal of the Brazilian Society of Urology* **38**, 298-305; discussion 306, doi:10.1590/s1677-55382012000300002 (2012).

31 Hardy, L. A., Vinnichenko, V. & Fried, N. M. *Holmium:YAG vs thulium fiber laser dusting of calcium oxalate monohydrate stones*. Vol. 10852 PWB (SPIE, 2019).

32 Saleh, B. E. A. & Teich, M. C. *Fundamentals of Photonics*. Second edn, 1177 (2009).

33 Silfvast, W. T. *Laser Fundamentals*. Second edn, (2004).

34 K Dutta , N. *Fiber Amplifiers and Fiber Lasers*.

35 Ball, D. W. *Field Guide to Spectroscopy*. (SPIE Press, 2006).

36 Judd, B. R. Optical Absorption Intensities of Rare-Earth Ions. *Physical Review* **127**, 750-761, doi:10.1103/PhysRev.127.750 (1962).

37 Ghiggino, K. P., Harris, M. R. & Spizzirri, P. G. Fluorescence lifetime measurements using a novel fiber - optic laser scanning confocal microscope. *Review of Scientific Instruments* **63**, 2999-3002, doi:10.1063/1.1142599 (1992).

38 Paschotta, R. *et al.* Lifetime quenching in Yb-doped fibres. *Optics Communications* **136**, 375-378, doi:https://doi.org/10.1016/S0030-4018(96)00720-1 (1997).

39 Reisfeld, R. 53-98 (Springer Berlin Heidelberg).

40 Cajzl, J. *et al. Characterization of fluorescence lifetime of Tm-doped fibers with increased quantum conversion efficiency*. Vol. 9450 PPR (SPIE, 2015).

41 Barnes, N. P. Solid-State Lasers From an Efficiency Perspective. *IEEE Journal of Selected Topics in Quantum Electronics* **13**, 435-447, doi:10.1109/JSTQE.2007.895280 (2007).

42 Crump, P. *et al.* Efficient High-Power Laser Diodes. *IEEE Journal of Selected Topics in Quantum Electronics* **19**, 1501211-1501211, doi:10.1109/jstqe.2013.2239961 (2013).

43 Ter-Mikirtychev, V. V. in *Encyclopedia of Spectroscopy and Spectrometry (Third Edition)* (eds John C. Lindon, George E. Tranter, & David W. Koppenaal) 481-491 (Academic Press, 2017).

44 Haque, N., Hughes, A., Lim, S. & Vernon, C. Rare Earth Elements: Overview of Mining, Mineralogy, Uses, Sustainability and Environmental Impact. *Resources* **3**, 614-635 (2014).

45 Karraker, D. G. Coordination of trivalent lanthanide ions. *Journal of Chemical Education* **47**, 424, doi:10.1021/ed047p424 (1970).

46 Blanc, W. *et al.* Thulium environment in a silica doped optical fibre. *Journal of Non-Crystalline Solids* **354**, 435-439, doi:10.1016/j.jnoncrysol.2007.06.083 (2008).

47 Agger, S. D. & Povlsen, J. H. Emission and absorption cross section of thulium doped silica fibers. *Opt. Express* **14**, 50-57, doi:10.1364/OPEX.14.000050 (2006).

48 Li, Z. *et al.* Thulium doped Fiber Amplifier for Optical Communications at 2 μm. *Opt Express* **21**, 9289-9297 (2013).

49 Jackson, S. D. Cross relaxation and energy transfer upconversion processes relevant to the functioning of 2 μm Tm3+-doped silica fibre lasers. *Optics Communications* **230**, 197-203, doi:10.1016/j.optcom.2003.11.045 (2004).

50 Kaierle, S. *et al.* Cross relaxation in Tm-doped fiber lasers. **8796**, 87961W, doi:10.1117/12.2011078 (2013).

51 McComb, T. S. *et al.* High-power widely tunable thulium fiber lasers. *Appl. Opt.* **49**, 6236-6242, doi:10.1364/AO.49.006236 (2010).

52 Moulton, P. F. *et al.* Tm-Doped Fiber Lasers: Fundamentals and Power Scaling. *IEEE Journal of Selected Topics in Quantum Electronics* **15**, 85-92, doi:10.1109/jstqe.2008.2010719 (2009).

53 Peterka, P., Kasik, I., Dhar, A., Dussardier, B. & Blanc, W. Thulium-doped silica fibers with enhanced 3H4 level lifetime Modelling the devices for 800-820nm band. (2012).

54 Simpson, D. A. *Spectroscopy of Thullium Doped Silica Glass* Doctor of Philosophy thesis, Victoria University, (2006).

55 Shardlow, P. C. *et al.* in *2017 European Conference on Lasers and Electro-Optics and European Quantum Electronics Conference.* CJ_11_14 (Optical Society of America).

56 Guhur, A. & Jackson, S. D. Efficient holmium-doped fluoride fiber laser emitting 2.1 μm and blue upconversion fluorescence upon excitation at 2 μm. *Opt. Express* **18**, 20164-20169, doi:10.1364/OE.18.020164 (2010).

57 Jackson, S. D., Bugge, F. & Erbert, G. Directly diode-pumped holmium fiber lasers. *Opt. Lett.* **32**, 2496-2498, doi:10.1364/OL.32.002496 (2007).

58 Walsh, B. M. Review of Tm and Ho Materials; Spectroscopy and Lasers. **19**, 855-866 (2009).

59 Jackson, S. D. The spectroscopic and energy transfer characteristics of the rare earth ions used for silicate glass fibre lasers operating in the shortwave infrared. *Laser Photonics Rev* **3**, 466-482, doi:10.1002/lpor.200810058 (2009).

60 Olshansky, R. Propagation in glass optical waveguides. *Reviews of Modern Physics* **51**, 341-367, doi:10.1103/RevModPhys.51.341 (1979).

61 Okamoto, K. *Fundamentals of Optical Waveguides*. Second edn, (2006).

62 Ghatak, A. & Thyagarajan, K. *Introduction to Fiber Optics*. (1997).

63 Multi-Wavelength Optical Fiber Refractive Index Profiling by Spatially Resolved Fourier Transform Spectroscopy. *Journal of Lightwave Technology* **28**, 360-364 (2010).

64 Yablon, A. New transverse techniques for characterizing high-power optical fibers. *Optical Engineering* **50**, 111603 (2011).

65 Chu, P. L. & Whitbread, T. Measurement of refractive-index profile of optical-fibre preform. *Electronics Letters* **15**, 295-296, doi:10.1049/el:19790210 (1979).

66 Novozámský, A., Slánička, J. & Peterka, P. *Tomography reconstruction of geometry and refractive index profile of highly asymmetric optical fiber preforms*. Vol. 7746 CPS (SPIE, 2010).

67 Javadimanesh, M., Ghavami Sabouri, S. & Khorsandi, A. The effect of cladding geometry on the absorption efficiency of double clad fiber lasers. *Optica Applicata* **XLVI**, doi:10.5277/oa160212 (2016).

68 Kouznetsov, D., Moloney, J. V. & Wright, E. M. Efficiency of pump absorption in double-clad fiber amplifiers. I. Fiber with circular symmetry. *J. Opt. Soc. Am. B* **18**, 743-749, doi:10.1364/JOSAB.18.000743 (2001).

69 Koška, P. *et al.* Enhanced pump absorption efficiency in coiled and twisted double-clad thulium-doped fibers. *Opt Express* **24**, doi:10.1364/OE.24.000102| (2016).

70 Kouznetsov, D. & Moloney, J. V. Efficiency of pump absorption in double-clad fiber amplifiers. II. Broken circular symmetry. *J. Opt. Soc. Am. B* **19**, 1259-1263, doi:10.1364/JOSAB.19.001259 (2002).

71 Wang, B. S. & Mies, E. W. *Advanced topics on fusion splicing of specialty fibers and devices*. Vol. 6781 ACP (SPIE, 2007).

72 Zachariasen, W. H. THE ATOMIC ARRANGEMENT IN GLASS. *Journal of the American Chemical Society* **54**, 3841-3851, doi:10.1021/ja01349a006 (1932).

73 Yamane, A. & Asahara, Y. *Glasses for photonics*. (Cambridge Univerisity Press, 2000).

74 Ten, S. Ultra Low-loss Optical Fiber Technology. *OFC OSA* (2016).

75 Auzel, F. Existance of Intrinsic Background Loss in Rare Earth Doped Fibres. *Electronics Letters* **29** (1993).

76 Humbach, O., Fabian, H., Grzesik, U., Haken, U. & Heitmann, W. Analysis of OH absorption bands in synthetic silica. *Journal of Non-Crystalline Solids* **203**, 19-26, doi:https://doi.org/10.1016/0022-3093(96)00329-8 (1996).

77 Plotnichenko, V. G., Sokolov, V. O. & Dianov, E. M. Hydroxyl groups in high-purity silica glass. *Inorganic Materials* **36**, 404-410, doi:10.1007/BF02758091 (2000).

78 Thorlabs. *0.22 NA Silica Core, Glass Clad Multimode Optical Fiber, Step Index*, <https://www.thorlabs.com/newgrouppage9.cfm?objectgroup_id=6838> (1990-2020).

79 Ainslie, B. J., Craig, S. P. & Davey, S. T. The absorption and fluorescence spectra of rare earth ions in silica-based monomode fiber. *Journal of Lightwave Technology* **6**, 287-293, doi:10.1109/50.4001 (1988).

80 Khopin, V. F. *et al.* Effect of core glass composition on the optical properties of active fibers. *Inorganic Materials* **41**, 434-437, doi:10.1007/s10789-005-0148-3 (2005).

81 Doremus, R. H. Viscosity of silica. *Journal of Applied Physics* **92**, 7619-7629, doi:10.1063/1.1515132 (2002).

82 Poole, S. B. Fabrication of Al2O3 co-doped optical fibres by a solution-doping technique. *Fourteenth European Conference on Optical Communication* (1988).

83 Dhar, A., Shymal, D., Himadri, S. & Ranjan, S. Fabrication of high aluminium containing rare-earth doped fiber without core–clad interface defects. *Optics Communications* **283**, 2344-2349 (2010).

84 Tang, F. Z., McNamara, P. & Barton, G. W. Enhanced Al Incorporation in Solution-Doped Optical Fibre Fabrication. (2006).

85 Saha, M., Pal, A., Pal, M. & Sen, R. Influence of aluminum on doping of ytterbium in optical fiber synthesized by vapor phase technique. *Optics Communications* **334**, 90-93, doi:10.1016/j.optcom.2014.07.070 (2015).

86 Arai, K. *et al.* Aluminum or phosphorus co - doping effects on the fluorescence and structural properties of neodymium - doped silica glass. *Journal of Applied Physics* **59**, 3430-3436, doi:10.1063/1.336810 (1986).

87 Kim, K.-S. & Pratsinis, S. E. Manufacture of optical waveguide preforms by modified chemical vapor deposition. *AIChE Journal* **34**, 912-921, doi:10.1002/aic.690340603 (1988).

88 Cognolato, L. Chemical Vapour Deposition for Optical Fibre Technology. *Le Journal de Physique IV* **05**, C5-975-C975-987, doi:10.1051/jphyscol:19955115 (1995).

89 Wanguang, L. & Davis, E. J. The effects of gas and particle properties on thermophoresis. *Journal of Aerosol Science* **27**, 1085-1099 (1995).

90 Moriarty, J. L. Vapor Pressures of Yttrium and Rare Earth Chlorides Above Their Melting Points. *Journal of Chemical & Engineering Data* **8**, 422-424, doi:10.1021/je60018a041 (1963).

91 Saha, M. & Sen, R. Vapor phase doping process for fabrication of rare earth doped optical fibers: Current status and future opportunities. *physica status solidi (a)* **213**, 1377-1391, doi:10.1002/pssa.201532668 (2016).

92 Poole, S. B., Payne, D. N. & Fermann, M. E. Fabrication of Low Loss Optical Fibres Containing Rare Earth Ions. (1985).

93 Boyland, A. J. *et al.* Optical Fiber Fabrication Using Novel Gas-Phase Deposition Technique. *Journal of Lightwave Technology* **29**, 912-915, doi:10.1109/jlt.2011.2109371 (2011).

94 Eisentraut, K. J. & Sievers, R. E. Volatile Rare Earth Chelates. *Journal of the American Chemical Society* **87**, 5254-5256, doi:10.1021/ja00950a051 (1965).

95 Springer, C. S., Meek, D. W. & Sievers, R. E. Rare earth chelates of 1,1,1,2,2,3,3-heptafluoro-7,7-dimethyl-4,6-octanedione. *Inorganic Chemistry* **6**, 1105-1110, doi:10.1021/ic50052a009 (1967).

96 Sicre, J. E., Dubois, J. T., Eisentraut, K. J. & Sievers, R. E. Volatile Lanthanide Chelates II. Vapor Pressures, Heats of Vaporization and Heats of Sublimation. *Journal of the American Chemical Society* **91**, 3476-3481 (1968).

97 Thomson, G. W. The Antoine Equation for Vapor-pressure Data. *Chemical Reviews* **38**, 1-39, doi:10.1021/cr60119a001 (1946).

98 Tumminelli, R. P., Mccollum, B. C. & Snitzer, E. Fabrication of High-Concentration Rare-Earth Doped Optical Fibers Using Chelates. *Journal of Lightwave Technology* **8**, 1680-1683, doi:Doi 10.1109/50.60565 (1990).

99 Muhd-Yassin, S. Z. *et al.* On the Initial Development of Rare Earth Doped Fiber using Chelate Delivery System. *IEEE* (2011).

100 Digonnet, M. J. F. *et al.* Optical properties of Yb-doped fibers prepared by gas phase doping. **8982**, 89820R, doi:10.1117/12.2036928 (2014).

101 Boyland, A. J. *et al.* in *CLEO/QELS: 2010 Laser Science to Photonic Applications.* 1-2.

102 Maitreyee, S., Atasi, P. & Ranjan, S. Vapor Phase Chelate Delivery Technique for Fabrication of Rare Earth Doped Optical Fiber. *International Conference on Fiber Optics and Photonics* (2012).

103 Tengfei, S., Zhou, Z., Xiao, X., Zhang, A. & Lin, A. Yb-doped LMA Fiber Fabricated by Chelate Deposition System for High Power Laser Applications. *CLEO: Applications and Technology* (2014).

104 Pal, M. *et al.* Investigation of the deposition of porous layers by the MCVD method for the preparation of rare-earth doped cores of optical fibres. *Optics Communications* **254**, 88-95, doi:https://doi.org/10.1016/j.optcom.2005.05.022 (2005).

105 Lupi, J. *et al.* Gradual-Time Solution Doping for the Fabrication of Longitudinally Varying Optical Fibres. *Journal of Lightwave Technology* **36**, 1786-1791, doi:10.1109/JLT.2017.2785862 (2018).

106 Smithgall, D. H. Application of Optimization Theory to the Control of the Optical Fiber Drawing Process. *Bell System Technical Journal* **58**, 1425-1435, doi:10.1002/j.1538-7305.1979.tb02262.x (1979).

107 Jaluria, Y. in *Advanced Materials Processing and Manufacturing* (ed Yogesh Jaluria) 239-286 (Springer International Publishing, 2018).

108 Khudyakov, I. V. Fast photopolymerization of acrylate coatings: Achievements and problems. *Progress in Organic Coatings* **121**, 151-159, doi:https://doi.org/10.1016/j.porgcoat.2018.04.030 (2018).

109 Dhar, A., Das, S., Maiti, H. S. & Sen, R. Fabrication of high aluminium containing rare-earth doped fiber without core–clad interface defects. *Optics Communications* **283**, 2344-2349, doi:https://doi.org/10.1016/j.optcom.2010.02.001 (2010).

110 Tang, F. Z., McNamara, P., W. Barton, G. & P. Ringer, S. Microscale Inhomogeneities in Aluminum Solution-Doping of Silica-Based Optical Fibers. *Journal of the American Ceramic Society*, doi:10.1111/j.1551-2916.2006.01330.x (2007).

111 Tang, F. Z., McNamara, P., Barton, G. W. & Ringer, S. P. Multiple solution-doping in optical fibre fabrication I – Aluminium doping. *Journal of Non-Crystalline Solids* **354**, 927-937, doi:10.1016/j.jnoncrysol.2007.08.020 (2008).

112 Tang, F. Z., McNamara, P., Barton, G. W. & Ringer, S. P. Multiple solution-doping in optical fibre fabrication II – Rare-earth and aluminium co-doping.

Journal of Non-Crystalline Solids **354**, 1582-1590, doi:10.1016/j.jnoncrysol.2007.10.006 (2008).

113 Strelov, K. K. & Kashcheev, I. D. Phase diagram of the system Al2O3-SiO2. *Refractories* **36**, 244-246, doi:10.1007/bf02227394 (1995).

114 A. Le Sauze *et al.* in *Optical Amplifiers and Their Applications.* WC5.

115 Tammela, S., Söderlund, M., Koponen, J., Philippov, V. & Stenius, P. *The potential of direct nanoparticle deposition for the next generation of optical fibers*. Vol. 6116 PWO (SPIE, 2006).

116 Kasik, I., Peterka, P., Mrázek, J. & Honzatko, P. Silica optical fibers doped with nanoparticles for fiber lasers and broadband sources. **12**, 277-290 (2016).

117 Kamrádek, M. *et al.* Nanoparticle and Solution Doping for Efficient Holmium Fiber Lasers. *IEEE Photonics Journal* **11**, 1-10, doi:10.1109/JPHOT.2019.2940747 (2019).

118 Simakov, N. *et al.* High gain holmium-doped fibre amplifiers. *Opt Express* **24**, 13946-13956, doi:10.1364/OE.24.013946 (2016).

119 Aubrecht, J. *et al. Characterization of holmium fibers with various concentrations for fiber laser applications around 2.1 um*. Vol. 9886 EPE (SPIE, 2016).

120 Hemming, A. *et al.* High power operation of cladding pumped holmium-doped silica fibre lasers. *Opt Express* **21**, 4560-4566, doi:10.1364/OE.21.004560 (2013).

121 Honzatko, P., Baravets, Y., Kasik, I. & Podrazky, O. Wideband thulium holmium doped fiber source with combined forward and backward spontaneous emission at 1600_2300nm spectral band. *Opt. Lett.* **39**, 3650-3653, doi:10.1364/OL.39.003650 (2014).

122 Kalisky, Y. Y., Rotman, S. R., Boulon, G., Pedrini, C. & Brenier, A. *Spectroscopic properties, energy transfer dynamics, and laser performance of thulium-holmium laser systems*. Vol. 2138 PWL (SPIE, 1994).

123 Cao, R. *et al.* Spectroscopy of thulium and holmium co-doped silicate glasses. *Opt. Mater. Express* **6**, 2252-2263, doi:10.1364/OME.6.002252 (2016).

124 4.62 kW excellent beam quality laser output with a low-loss Yb/Ce co-doped fiber fabricated by chelate gas phase deposition technique. *Opt. Mater. Express* **7**, 1259-1266, doi:10.1364/OME.7.001259 (2017).

125 in *Advanced Solid-State Lasers Congress.* ATh4A.2.

126 Yoo, S. *et al.* Ytterbium-doped Y2O3 nanoparticle silica optical fibers for high power fiber lasers with suppressed photodarkening. *Optics Communications* **283**, 3423-3427, doi:https://doi.org/10.1016/j.optcom.2010.04.093 (2010).

127 Analysis and optimization of acoustic speed profiles with large transverse variations for mitigation of stimulated Brillouin scattering in optical fibers. *Appl. Opt.* **49**, 1388-1399, doi:10.1364/AO.49.001388 (2010).

128 Highly efficient ytterbium-doped phosphosilicate fiber lasers operating below 1020nm. *Opt. Express* **23**, 17693-17700, doi:10.1364/OE.23.017693 (2015).

129 Unger, S. *et al. Influence of aluminum-phosphorus codoping on optical properties of ytterbium-doped laser fibers*. Vol. 7212 PWO (SPIE, 2009).

130 Saha, M., Pal, A., Pal, M., Guha, C. & Sen, R. An Optimized Vapor Phase Doping Process to Fabricate Large Core Yb-Doped Fibers. *Journal of Lightwave Technology* **33**, 3533-3541, doi:10.1109/JLT.2015.2442226 (2015).

131 Kirchhof, J., Unger, S. & Dellith, J. Diffusion of Phosphorus Doped Silica for Active Optical Fibers. *Journal of Non-Crystalline Solids* **s 345–346**, 234–238, doi:10.1016/j.jnoncrysol.2004.08.028 (2004).

132 Unger, S. *et al. Optical properties of Yb-doped laser fibers in dependence on codopants and preparation conditions*. Vol. 6890 PWO (SPIE, 2008).

133 Laperle, P., Paré, C., Zheng, H. & Croteau, A. *Yb-doped LMA triple-clad fiber for power amplifiers*. Vol. 6453 PWL (SPIE, 2007).

134 M. E. Likhachev *et al.* in *CLEO/Europe and EQEC 2011 Conference Digest.* CJ_P24.